

# Photocouplings at the pole from pion photoproduction

D. Rönchen<sup>1,a</sup>, M. Döring<sup>2,3,b</sup>, F. Huang<sup>4,5</sup>, H. Haberzettl<sup>3</sup>, J. Haidenbauer<sup>1,6</sup>, C. Hanhart<sup>1,6</sup>, S. Krewald<sup>1,6</sup>, U.-G. Meißner<sup>1,2,6</sup>, and K. Nakayama<sup>1,5</sup>

<sup>1</sup> Institut für Kernphysik and Jülich Center for Hadron Physics, Forschungszentrum Jülich, 52425 Jülich, Germany

<sup>2</sup> Helmholtz-Institut für Strahlen- und Kernphysik (Theorie) and Bethe Center for Theoretical Physics, Universität Bonn, Nußallee 14-16, 53115 Bonn, Germany

<sup>3</sup> Institute for Nuclear Studies and Department of Physics, The George Washington University, Washington, DC 20052, USA

<sup>4</sup> School of Physics, University of Chinese Academy of Sciences, Huairou District, Beijing 101408, China

<sup>5</sup> Department of Physics and Astronomy, University of Georgia, Athens, Georgia 30602, USA

<sup>6</sup> Institute for Advanced Simulation, Forschungszentrum Jülich, 52425 Jülich, Germany

Received: 29 January 2014 / Revised: 9 May 2014

Published online: 24 June 2014 – © Società Italiana di Fisica / Springer-Verlag 2014

Communicated by B. Ananthanarayan

**Abstract.** The reactions  $\gamma p \rightarrow \pi^0 p$  and  $\gamma p \rightarrow \pi^+ n$  are analyzed in a semi-phenomenological approach up to  $E \sim 2.3$  GeV. Fits to differential cross section and single- and double-polarization observables are performed. A good overall reproduction of the available photoproduction data is achieved. The Jülich2012 dynamical coupled-channel model—which describes elastic  $\pi N$  scattering and the world data base of the reactions  $\pi N \rightarrow \eta N$ ,  $K\Lambda$ , and  $K\Sigma$  at the same time—is employed as the hadronic interaction in the final state. The framework guarantees analyticity and, thus, allows for a reliable extraction of resonance parameters in terms of poles and residues. In particular, the photocouplings at the pole can be extracted and are presented.

## 1 Introduction

Quantum Chromodynamics (QCD) manifests itself in a rich spectrum of excited baryons in the region between the perturbative regime and the ground-state hadrons. Most of the available information on the resonance spectrum was obtained by partial-wave analyses of elastic  $\pi N$  scattering [1–3]. However, it is important to include other channels like  $\eta N$ ,  $K\Lambda$  or  $K\Sigma$  that couple to the  $\pi N$  system into such analyses. It is expected that data obtained for those other meson-baryon channels could help to shed light on the so-called “missing resonances” predicted in quark models and related approaches [4–12] or lattice calculations [13] and assumed to couple only weakly to  $\pi N$ .

Since the amount of data on transition reactions like  $\pi N \rightarrow \eta N$ ,  $K\Lambda$ ,  $K\Sigma$ , etc., is somewhat limited, one should take advantage of the wealth and precision of the corresponding photoproduction data supplied over the past few years by experimental facilities like ELSA, GRAAL, JLab, MAMI, and SPring-8. Clearly, also in the case of photoproduction so far, certain assumptions have to be made in partial-wave analyses because the data are not yet accurate enough to allow for a model-independent extraction

of the amplitude. However, the latter will become possible once more precise and more complete experiments become available [14–17]. It should be said that for pion photoproduction, in principle, a complete set of observables  $\{\sigma, \Sigma, T, P, E, G, C_x, C_z\}$ —which would allow a full determination of the reaction amplitude [18]—has become available quite recently. However, the observables in question have not yet been measured at the same energies—which would be required, at least formally, for a complete experiment. Actually, due to the self-analyzing nature of hyperons, the aim of providing a complete set of experiments is easier to realize in kaon photoproduction than in pion photoproduction. Finally, we want to mention that a smaller number of polarization observables is sufficient for an analysis within a truncated multipole expansion, see the arguments in refs. [19, 20].

To analyze pion- as well as photon-induced data theoretically, different approaches have been applied. The  $\pi N$  threshold region is well understood in terms of chiral perturbation theory (ChPT) [21–35], while extensions in form of unitarized chiral approaches [36–53] allow one to study the resonance region but also to consider the coupling to other channels like  $\eta N$ ,  $K\Lambda$  or  $K\Sigma$ .

$K$ -matrix [54–65] or unitary isobar models [66, 67] provide practical and flexible tools to analyze large amounts of data. By omitting the real parts of the self-energies the

<sup>a</sup> e-mail: d.roenchen@fz-juelich.de

<sup>b</sup> e-mail: doering@hiskp.uni-bonn.de

complexity of the calculation is strongly reduced and only on-shell intermediate states are included. While unitarity is preserved, dispersive parts are often neglected; this introduces systematic uncertainties into the extraction of resonance positions and residues.

For the task of a simultaneous analysis of different reactions, dynamical coupled-channel (DCC) models [68–78] are particularly well suited as they obey theoretical constraints of the  $S$ -matrix such as analyticity and unitarity. This allows for a reliable extraction of resonance parameters in terms of poles and residues in the complex energy plane. A simultaneous description of the reactions  $\pi N \rightarrow \pi N$ ,  $\eta N$  and  $KY$  ( $K\Lambda$ ,  $K\Sigma$ ) has been accomplished within the DCC framework of the Jülich2012 model [79]. See also the supplementary material and tables of hadronic transitions among the channels  $\pi N$ ,  $\eta N$ ,  $K\Lambda$ , and  $K\Sigma$  which are available online [80]. In this approach [79, 81–85], the inclusion of the dispersive contributions of intermediate states and the correct structure of branch points [86] guarantee analyticity. The scattering amplitude is obtained as solution of a Lippmann-Schwinger-type equation, formulated in time-ordered perturbation theory (TOPT), which automatically ensures two-body unitarity. The three-body channel  $\pi\pi N$  is important because it is the source of large inelasticities. Its effect is included in the model via effective  $\pi\Delta$ ,  $\sigma N$  and  $\rho N$  channels. In the Jülich2012 model, the  $t$ -channel exchanges are complemented by  $u$ -channel baryon exchanges to approximate the left-hand cut. Together, they constitute the non-resonant part of the interaction, referred to as “background”. Bare resonances are introduced as  $s$ -channel processes. The explicit treatment of the background in terms of  $t$ - and  $u$ -channel diagrams imposes strong correlations amongst the different partial waves and generates a non-trivial energy and angular dependence of the observables. Interestingly, the  $\pi N \rightarrow KY$  amplitudes found in ref. [79] are quite similar to those of a later analysis performed by the Bonn-Gatchina group [87].

The adaptation of DCC models to finite volumes, to allow for the prediction of lattice levels and the calculation of finite volume corrections, was pioneered in ref. [88]. In principle, such extensions of hadronic approaches allow for the analysis of experimental and “data” from lattice QCD simulations [13, 89–91] on the same footing [92–95]. Chiral extrapolations are non-trivial due to the intricate coupled-channel structure in meson-baryon scattering [96].

Recently, it was shown how the Jülich coupled-channels approach can be extended to pion photoproduction [97] within a gauge-invariant framework that respects the generalized off-shell Ward-Takahashi identity [98–100]. Such a field-theoretical description of the photoproduction process is, however, technically rather involved. Therefore, in the present work we follow a more phenomenological approach in which we use a flexible and easy-to-implement parametrization of the photo-excitation vertices at the multipole-amplitude level. This approach is inspired by the GWU/DAC CM12 parameterization of ref. [3], that complements earlier parameterizations [16, 101–104]. In this way, we will be able to consider a far larger and more comprehensive set of pion photoproduction data than before [97], although at the expense of giving up any direct

connection with the microscopic reaction dynamics of the photo-interaction. For the hadronic interaction part, all microscopic features from our full DCC approach [79] are preserved (*i.e.* the elastic  $\pi N$  and  $\pi N \rightarrow \eta N$ ,  $KY$  data are described). We view this semi-phenomenological approach as an intermediate step towards building a more microscopic DCC description not only of photoproduction, but also of electroproduction processes along the lines of ref. [97].

The paper is organized as follows: in sect. 2, we give an overview of the formalism of the hadronic coupled-channel model and the phenomenological parameterization of the photo-excitation vertices. The data base and the fitting strategy are described in sect. 3.1. In sect. 3.2, the fit results are compared to data and discussed in detail. The extracted photocouplings at the pole can be found in sect. 3.4. In the appendices, details of the multipole decomposition of the photoproduction amplitude and the definition of the observables and the photocouplings are given.

## 2 Formalism

### 2.1 Two-potential formalism for the hadronic interaction

Both the hadronic scattering matrix and the photoproduction amplitude can be decomposed into a pole and a non-pole part as outlined in this and the following section. This decomposition is not required by the photoproduction formalism because the photoproduction amplitude can be formulated in terms of the full half-offshell  $T$ -matrix as shown in the next section. However, the decomposition in pole and non-pole parts simplifies numerics significantly as outlined in sect. 3.1.

The partial-wave  $T$ -matrix in the Jülich2012 formulation [79] is given by the integral equation,

$$T_{\mu\nu}(q, p', E) = V_{\mu\nu}(q, p', E) + \sum_{\kappa} \int_0^{\infty} dp p^2 V_{\mu\kappa}(q, p, E) G_{\kappa}(p, E) T_{\kappa\nu}(p, p', E), \quad (1)$$

where  $q \equiv |\vec{q}|$  ( $p' \equiv |\vec{p}'|$ ) is the modulus of the outgoing (incoming) three-momentum that may be on- or off-shell,  $E$  is the scattering energy, and  $\mu, \nu, \kappa$  are channel indices. In eq. (1), the propagator  $G_{\kappa}$  has the form

$$G_{\kappa}(p, E) = \frac{1}{E - E_a(p) - E_b(p) + i\epsilon}, \quad (2)$$

where  $E_a = \sqrt{m_a^2 + p^2}$  and  $E_b = \sqrt{m_b^2 + p^2}$  are the on-mass-shell energies of the intermediate particles  $a$  and  $b$  in channel  $\kappa$  with respective masses  $m_a$  and  $m_b$ . Equation (1) is formulated in the partial-wave basis, *i.e.* the amplitude only depends on the modulus of the incoming, outgoing, and intermediate particle momenta. This implies a partial-wave decomposition of the exchange potentials [84, 85]. The denominator in eq. (1) corresponds

to the channels with stable particles,  $\pi N$ ,  $\eta N$ ,  $KA$ , and  $K\Sigma$ ; for the effective  $\pi\pi N$  channels ( $\pi\Delta$ ,  $\sigma N$ ,  $\rho N$ ), the propagator is more involved [83, 85].

The sum of the  $u$ - and  $t$ -channel diagrams is labeled as  $V^{\text{NP}}$  in the following. The full set is shown in figs. 1 and 2 of ref. [79]. Together with the (bare)  $s$ -channel exchanges  $V^{\text{P}}$ , they constitute the interaction  $V$  in eq. (1),

$$V_{\mu\nu} = V_{\mu\nu}^{\text{NP}} + V_{\mu\nu}^{\text{P}} \equiv V_{\mu\nu}^{\text{NP}} + \sum_{i=0}^n \frac{\gamma_{\mu;i}^a \gamma_{\nu;i}^c}{E - m_i^b}, \quad (3)$$

with  $n$  being the number of bare  $s$ -channel states in a given partial wave. The  $\gamma_{\mu;i}^c$  ( $\gamma_{\nu;i}^a$ ) are the bare creation (annihilation) vertices of resonance  $i$  with bare mass  $m_i^b$ . The notation is chosen to be consistent with earlier work; confusions with the photon ( $\gamma$ ) should be excluded by the context. The explicit form of the resonance vertex functions can be found in appendix B of ref. [81] and in appendix A of ref. [79]. In the following we make use of the two-potential formalism and apply it to the decomposition defined in eq. (3). Inserting  $V^{\text{NP}}$  into a Lippmann-Schwinger-type equation,

$$T_{\mu\nu}^{\text{NP}} = V_{\mu\nu}^{\text{NP}} + \sum_{\kappa} V_{\mu\kappa}^{\text{NP}} G_{\kappa} T_{\kappa\nu}^{\text{NP}}, \quad (4)$$

leads to the so-called *non-pole* part of the full  $T$ -matrix (projected to a partial wave). For simplicity, in eq. (4) and the following, the integration over the momentum of the intermediate state  $p$ , cf. eq. (1), is not written explicitly. The  $s$ -channel exchanges that constitute  $V^{\text{P}}$  generate the pole part of the  $T$ -matrix,  $T^{\text{P}}$ . The latter involves the non-pole part  $T^{\text{NP}}$  given in eq. (4) and can be expressed in terms of the quantities

$$\begin{aligned} \Gamma_{\mu;i}^c &= \gamma_{\mu;i}^c + \sum_{\nu} \gamma_{\nu;i}^c G_{\nu} T_{\nu\mu}^{\text{NP}}, \\ \Gamma_{\mu;i}^a &= \gamma_{\mu;i}^a + \sum_{\nu} T_{\mu\nu}^{\text{NP}} G_{\nu} \gamma_{\nu;i}^a, \\ \Sigma_{ij} &= \sum_{\mu} \gamma_{\mu;i}^c G_{\mu} \Gamma_{j;\mu}^a, \end{aligned} \quad (5)$$

where  $\Gamma^c$  ( $\Gamma^a$ ) are the so-called dressed resonance creation (annihilation) vertices and  $\Sigma$  is the self-energy. The indices  $i, j$  label the  $s$ -channel state in the case of multiple resonances. The order of terms in eq. (5) and all following equations corresponds to the convention that time flows from the right to the left. For the case of two resonances in a partial wave, the pole part reads explicitly [105]

$$T_{\mu\nu}^{\text{P}} = \Gamma_{\mu}^a D^{-1} \Gamma_{\nu}^c,$$

where

$$\begin{aligned} \Gamma_{\mu}^a &= (\Gamma_{\mu;1}^a, \Gamma_{\mu;2}^a), & \Gamma_{\mu}^c &= \begin{pmatrix} \Gamma_{\mu;1}^c \\ \Gamma_{\mu;2}^c \end{pmatrix}, \\ D &= \begin{pmatrix} E - m_1^b - \Sigma_{11} & -\Sigma_{12} \\ -\Sigma_{21} & E - m_2^b - \Sigma_{22} \end{pmatrix}, \end{aligned} \quad (6)$$

from which the single-resonance case follows immediately. It is easy to show that the full scattering  $T$ -matrix of eq. (1) is given by the sum of pole and non-pole parts,

$$T_{\mu\nu} = T_{\mu\nu}^{\text{P}} + T_{\mu\nu}^{\text{NP}}. \quad (7)$$

## 2.2 Two-potential formalism for photoproduction

The photoproduction multipole amplitude in terms of a photoproduction kernel  $V_{\mu\gamma}$  is given by

$$\begin{aligned} M_{\mu\gamma}(q, E) &= V_{\mu\gamma}(q, E) + \sum_{\kappa} \int_0^{\infty} dp p^2 T_{\mu\kappa}(q, p, E) \\ &\quad \times G_{\kappa}(p, E) V_{\kappa\gamma}(p, E). \end{aligned} \quad (8)$$

Here and in the following the index  $\gamma$  is used exclusively for the  $\gamma N$  channel. Note that in the second term the photoproduction kernel produces a meson-baryon pair in channel  $\kappa$  with off-shell momentum  $p$  that rescatters via the hadronic half-offshell  $T$ -matrix, producing the final  $\pi N$  state (more generally, channel  $\mu$ ) with momentum  $q$ . The formalism allows for off-shell external  $q$  but we will consider only the production of real pions in the following. Similarly,  $V_{\mu\gamma}$  can also depend on the virtuality of the photon, but we will consider only real photons with  $Q^2 = 0$ . With the choice of  $V_{\mu\gamma}$  as specified below, the photoproduction amplitude of eq. (8) satisfies Watson's theorem by construction.

The photoproduction kernel can be written as

$$V_{\mu\gamma}(p, E) = \alpha_{\mu\gamma}^{\text{NP}}(p, E) + \sum_i \frac{\gamma_{\mu;i}^a(p) \gamma_{\gamma;i}^c(E)}{E - m_i^b}. \quad (9)$$

Here,  $\alpha_{\mu\gamma}^{\text{NP}}$  represents the photon coupling to  $t$ - and  $u$ -channel diagrams and to contact diagrams. These diagrams together form the non-pole part of the full photoproduction kernel as can be seen from field-theoretical considerations [100]. The summation in eq. (9) is over the resonances  $i$  in a multipole, and the  $\gamma_{\gamma;i}^c$  are the real tree-level  $\gamma NN_i^*$  and  $\gamma N \Delta_i^*$  photon couplings that only depend on the energy  $E$  but not on the momentum  $p$ . It is crucial that the resonance annihilation vertex  $\gamma^a$  in eq. (9) is precisely the same as in the hadronic part of eq. (3) so that the explicit singularity at  $E = m_i^b$  cancels.

The two-potential formalism allows one to rewrite the photoproduction amplitude  $M$  as

$$\begin{aligned} M_{\mu\gamma} &= \alpha_{\mu\gamma}^{\text{NP}} + \sum_{\kappa} T_{\mu\kappa}^{\text{NP}} G_{\kappa} \alpha_{\kappa\gamma}^{\text{NP}} + \Gamma_{\mu;i}^a (D^{-1})_{ij} \Gamma_{\gamma;j}^c, \\ \Gamma_{\gamma;j}^c &= \gamma_{\gamma;j}^c + \sum_{\kappa} \Gamma_{\kappa;j}^c G_{\kappa} \alpha_{\kappa\gamma}^{\text{NP}}, \end{aligned} \quad (10)$$

with the dressed resonance-creation photon-vertex  $\Gamma_{\gamma;j}^c$  which is a vector in resonance space, like the strong dressed vertex  $\Gamma_{\mu;i}^c$  in eq. (6). This standard result has been derived, *e.g.*, in ref. [105]. In the form of eq. (10) it becomes apparent that in  $M_{\mu\gamma}$  all singularities due to the bare resonances of eq. (9) have canceled.

Alternatively, one can write the amplitude simply in terms of the full hadronic  $T$ -matrix as

$$M_{\mu\gamma} = \sum_{\kappa} (1 - VG)_{\mu\kappa}^{-1} V_{\kappa\gamma}. \quad (11)$$

In principle, any of the forms (8), (10), or (11) can be used in practical calculations. In the form of eq. (11), which resembles the one of ref. [106], the similarity with the CM12 Chew-Mandelstam parameterization of the CNS/DAC group [3] becomes apparent, in which the hadronic kernel  $\bar{K}_{\kappa\nu}$  of the hadronic  $T$ -matrix,

$$T_{\mu\nu} = \sum_{\kappa} (1 - \bar{K}C)_{\mu\kappa}^{-1} \bar{K}_{\kappa\nu}, \quad (12)$$

is replaced by a photoproduction kernel,  $\bar{K}_{\kappa\gamma}$ ,

$$M_{\mu\gamma} = \sum_{\kappa} (1 - \bar{K}C)_{\mu\kappa}^{-1} \bar{K}_{\kappa\gamma}. \quad (13)$$

Here,  $C$  is the complex Chew-Mandelstam function that guarantees unitarity. While eq. (13) is formally identical to eq. (11), there is a practical difference: Equation (11) implies an integration over intermediate off-shell momenta, while the quantities  $\bar{K}$  and  $C$  in eq. (13) factorize. In both approaches the dispersive parts of the intermediate loops  $G$  and  $C$  are maintained.

In the present approach, the terms  $\alpha_{\mu\gamma}^{\text{NP}}$  and  $\gamma_{\gamma;i}^c$  in eq. (9) are approximated by polynomials  $P$ ,

$$\begin{aligned} \alpha_{\mu\gamma}^{\text{NP}}(p, E) &= \frac{\tilde{\gamma}_{\mu}^a(p)}{\sqrt{m_N}} P_{\mu}^{\text{NP}}(E) \\ \gamma_{\gamma;i}^c(E) &= \sqrt{m_N} P_i^{\text{P}}(E), \end{aligned} \quad (14)$$

where  $\tilde{\gamma}_{\mu}^a$  is a vertex function equal to  $\gamma_{\mu;i}^a$  but stripped of any dependence on the resonance number  $i$ . Equation (14) means that we have  $n+m$  polynomials per multipole with  $n$  resonances  $i$  and  $m$  hadronic channels  $\mu$ . With this parameterization, non-analyticities from left-hand cuts, like the one from the pion-pole term, are approximated by polynomials. As the distance to the physical region is quite large, such an approximation can be justified. Note in this context that even for the  $\gamma\gamma \rightarrow \pi\pi$  reaction that has a very close-by left-hand cut, the Born contributions can be effectively parameterized by a linear polynomial [107].

The photoproduction kernel  $V_{\mu\gamma}$  should have the correct threshold structure,  $V_{\mu\gamma} \sim q^L$  where  $q$  is the center-of-mass momentum in channel  $\mu$  and  $L$  is the orbital angular momentum. The  $L$  dependence of the different channels with a given  $J^P$  can be found, *e.g.*, in table XI of ref. [79]. The correct  $L$  dependence is automatically provided by the bare resonance vertices  $\gamma_{\mu;i}^a$  and, thus, already fulfilled for the pole part of eq. (14). The same applies to the vertex function  $\tilde{\gamma}_{\mu}^a$  in the non-pole part of eq. (14).

The final choice for the polynomials  $P$ , for a given multipole, is then

$$\begin{aligned} P_i^{\text{P}}(E) &= \sum_{j=1}^{\ell_i} g_{i,j}^{\text{P}} \left( \frac{E - E_s}{m_N} \right)^j e^{-\lambda_i^{\text{P}}(E - E_s)} \\ P_{\mu}^{\text{NP}}(E) &= \sum_{j=0}^{\ell_{\mu}} g_{\mu,j}^{\text{NP}} \left( \frac{E - E_s}{m_N} \right)^j e^{-\lambda_{\mu}^{\text{NP}}(E - E_s)}, \end{aligned} \quad (15)$$

with  $E_s$  being a suitable expansion point close to the  $\pi N$  threshold,  $E_s = 1077$  MeV. The appearance of the nucleon mass  $m_N$  in eqs. (14) and (15) ensures that the  $g$ 's are dimensionless quantities. The  $g$  and the  $\lambda > 0$  are multipole-dependent free parameters that are fitted to data. Furthermore, to fulfill the decoupling theorem, that resonance contributions are parametrically suppressed at threshold, the sum for  $P^{\text{P}}$  starts with  $j = 1$  and not with  $j = 0$  (hence, the expansion is chosen at threshold). In the fitting procedure,  $\ell_i$  and  $\ell_{\mu}$  are chosen as demanded by data but always  $\ell_i, \ell_{\mu} \leq 3$ . The factor  $e^{-\lambda(E - E_s)}$  ensures that the multipole amplitudes are well behaved in the high-energy limit, and, at the same time, absorbs the potentially strong energy dependence induced by the  $\gamma N$  threshold that is close to the  $\pi N$  threshold. In any case, it is clear that this effective parameterization cannot be used for sub-threshold extrapolations.

In a covariant microscopic formulation of the reaction dynamics of photoprocesses, as for example in ref. [97], local gauge invariance in the form of generalized Ward-Takahashi identities [98–100] provides an important and indispensable off-shell constraint that governs the correct microscopic interplay of longitudinal and transverse contributions of the electromagnetic currents. The present study, by contrast, concerns only a phenomenological three-dimensional parametrization of the underlying reaction dynamics where the real (and thus transverse) photons never “see” the longitudinal parts of the electromagnetic currents important for local gauge invariance. The physical (on-shell) amplitudes obtained here thus trivially correspond to globally conserved currents because the parametrization is chosen from the very beginning to only model the transverse contributions of the current. Global gauge invariance (which is the only measurable constraint), therefore, is never an issue for the present study. The situation is more complicated if one considers virtual photons, however, we will not enter this discussion here.

In the present approach, the photon is allowed to couple to the  $\pi N$ ,  $\eta N$  and  $\pi\Delta$  channels. The latter accounts for the inelasticity into the  $\pi\pi N$  channels. As long as the analysis is restricted to one-pion photoproduction, as in this study, there is no need to include additional couplings of the photon to  $\sigma N$  and  $\rho N$ . As for the  $\pi\Delta$  channels, there are usually two independent couplings for a given multipole; we only couple the photon to the  $\pi\Delta$  channel with the lower  $L$  (*c.f.* also table XI of ref. [79]). The extension to  $\eta N$ ,  $K\Lambda$  and  $K\Sigma$  photoproduction is planned for the future and will require direct photon couplings to these states. As for photoproduction on the neutron, the JLab

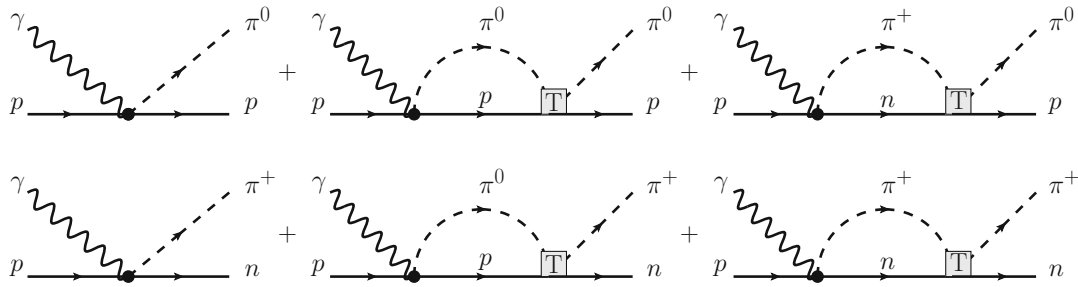


**Fig. 1.** Schematic representation of the reactions  $\gamma p \rightarrow \pi^0 p$  (upper row) and  $\gamma p \rightarrow \pi^+ n$  (lower row), cf. eqs. (16) and (17). The small black dots represent the potentials  $V_{\frac{1}{2}(\pi N \gamma p)}$  and  $V_{\frac{3}{2}(\pi N \gamma p)}$ , while  $T$  is the hadronic  $T$ -matrix. Not shown are the excitations of intermediate  $\pi\Delta$  and  $\eta N$  channels that are treated isospin-symmetrically.

FROST and HD-ICE experiments are currently being analyzed [108,109] and theoretical methods are being developed to disentangle the neutron amplitudes [101,110,111]

For completeness, a multipole decomposition of the pseudoscalar meson photoproduction amplitude is given in appendix A.

### 2.3 Isospin breaking

In the Jülich model, in general, isospin-averaged masses are used, which has little effect at energies that are not very close to the threshold, as it is the case for the hadronic data used in the analysis of ref. [79]. For pion photoproduction, however, there are data at very low energies and we have to take into account the different threshold energies for the  $\pi^0 p$  and the  $\pi^+ n$  channels.

In the particle basis, the amplitudes for the processes  $\gamma p \rightarrow \pi^0 p$  and  $\gamma p \rightarrow \pi^+ n$  are shown in fig. 1 and read

$$\begin{aligned}
 M_{\pi^0 p \gamma p} &= V_{\pi^0 p \gamma p} + T_{\pi^0 p \pi^0 p} G_{\pi^0 p} V_{\pi^0 p \gamma p} \\
 &\quad + T_{\pi^0 p \pi^+ n} G_{\pi^+ n} V_{\pi^+ n \gamma p} \\
 &\quad + \sum_{\kappa \neq \pi N} \left( T_{\frac{1}{2}(\pi N \kappa)} G_{\kappa} V_{\frac{1}{2} \kappa \gamma p} \right. \\
 &\quad \left. + \frac{2}{3} T_{\frac{3}{2}(\pi N \kappa)} G_{\kappa} V_{\frac{3}{2} \kappa \gamma p} \right), \quad (16)
 \end{aligned}$$

$$\begin{aligned}
 M_{\pi^+ n \gamma p} &= V_{\pi^+ n \gamma p} + T_{\pi^+ n \pi^0 p} G_{\pi^0 p} V_{\pi^0 p \gamma p} \\
 &\quad + T_{\pi^+ n \pi^+ n} G_{\pi^+ n} V_{\pi^+ n \gamma p} \\
 &\quad + \sum_{\kappa \neq \pi N} \left( \sqrt{2} T_{\frac{1}{2}(\pi N \kappa)} G_{\kappa} V_{\frac{1}{2} \kappa \gamma p} \right. \\
 &\quad \left. - \frac{\sqrt{2}}{3} T_{\frac{3}{2}(\pi N \kappa)} G_{\kappa} V_{\frac{3}{2} \kappa \gamma p} \right), \quad (17)
 \end{aligned}$$

where  $\kappa \neq \pi N$  stands for the sum over the intermediate states  $\pi\Delta$  and  $\eta N$  that are assumed to fulfill isospin symmetry as indicated with isospin indices  $I = \frac{1}{2}, \frac{3}{2}$ . Furthermore, note that  $T_{\pi^0 p \pi^0 p}$  is a pure isoscalar transition and, thus, very small near threshold [28–30,112–115]. As a consequence,  $E_0^+(\pi^0 p)$  develops only a very small imaginary part below the  $\pi^+ n$  threshold.

For the hadronic final-state interaction  $T_{\mu\nu}$ , and for  $V_{\mu\gamma}$  in eqs. (16) and (17) we neglect the small mass differ-

ences within the isospin multiplets, *i.e.*

$$\begin{aligned}
 V_{\pi^0 p \gamma p} &= V_{\frac{1}{2}(\pi N \gamma p)} + \frac{2}{3} V_{\frac{3}{2}(\pi N \gamma p)}, \\
 V_{\pi^+ n \gamma p} &= \sqrt{2} V_{\frac{1}{2}(\pi N \gamma p)} - \frac{\sqrt{2}}{3} V_{\frac{3}{2}(\pi N \gamma p)}, \\
 T_{\pi^0 p \pi^0 p} &= \frac{1}{3} T_{\frac{1}{2}(\pi N \pi N)} + \frac{2}{3} T_{\frac{3}{2}(\pi N \pi N)}, \\
 T_{\pi^0 p \pi^+ n} &= \frac{\sqrt{2}}{3} T_{\frac{1}{2}(\pi N \pi N)} - \frac{\sqrt{2}}{3} T_{\frac{3}{2}(\pi N \pi N)}, \\
 T_{\pi^+ n \pi^+ n} &= \frac{2}{3} T_{\frac{1}{2}(\pi N \pi N)} + \frac{1}{3} T_{\frac{3}{2}(\pi N \pi N)}. \quad (18)
 \end{aligned}$$

The  $\pi^0 p$  and  $\pi^+ n$  propagators  $G_{\pi^0 p}$ ,  $G_{\pi^+ n}$  have the same form as the isospin-symmetric  $\pi N$  propagator but incorporate the exact proton (neutron) and  $\pi^0$  ( $\pi^+$ ) masses,

$$G_{\pi^0 p} = \frac{1}{E - \sqrt{m_p^2 + p^2} - \sqrt{M_{\pi^0}^2 + p^2} + i\epsilon}, \quad (19)$$

$$G_{\pi^+ n} = \frac{1}{E - \sqrt{m_n^2 + p^2} - \sqrt{M_{\pi^+}^2 + p^2} + i\epsilon}. \quad (20)$$

Accordingly, to calculate the differential cross section close to threshold in eq. (B.13) instead of the averaged  $m_N$  we use  $m_p$  and  $m_n$  for calculating  $|\vec{q}|$ . The same applies to  $m_N$  appearing in eq. (A.6).

## 3 Results

Before we start discussing the present results, a remark on the observables discussed in this work is in order. There are many different conventions used in the literature to define the spin polarization observables. Our convention is given explicitly in appendix B and agrees with that used by the SAID group [104].

### 3.1 Data base and fit parameters

The free parameters  $g$  and  $\lambda$  of eq. (15) are determined by MINUIT fits on the JUROPA supercomputer at the Forschungszentrum Jülich. In a first step, the parameters

**Table 1.** Characteristics of fits 1 and 2. The difference between the fits shows the impact of recent high-precision measurements of  $\Sigma$ ,  $\Delta\sigma_{31}$ ,  $G$  and  $H$  from ELSA, JLab and MAMI.

	Fit 1	Fit 2
Line style	— — — —	—————
# of data	21,627	23,518
Excluded data	$\pi^0 p$ : $E > 2.33$ GeV and $\theta < 40^\circ$ for $E > 2.05$ GeV $\pi^+ n$ : $E > 2.26$ GeV and $\theta < 9^\circ$ for $E > 1.60$ GeV	
$ds/d\Omega$ , P, T	included	included
$\Sigma$	included (CLAS [118] predicted)	included
$\Delta\sigma_{31}$ , $G$ , $H$	predicted	included
$E$ , $F$ , $C_{x'L}$ , $C_{z'L}$	predicted	predicted
Sys. Error	5%	5%
$\chi^2$	20,095	22,880
$\chi^2/\text{d.o.f.}$	0.95	0.99

are fitted to the multipole amplitudes of the GWU/SAID CM12 solution [3] which guarantees a good starting point for the second step that involves fitting only to the data. The two reactions  $\gamma p \rightarrow \pi^0 p$  and  $\gamma p \rightarrow \pi^+ n$  are studied simultaneously. For the connection of the present formalism to observables see appendix B. The hadronic  $T$ -matrix in eq. (8) is taken from the Jülich2012 fit A [79]. This interaction describes elastic  $\pi N$  scattering and the world data base of  $\pi N \rightarrow \eta N$  and  $KY$ . Simultaneous fits to pion- and photon-induced reactions in the spirit of refs. [116,117] are planned for the future.

In the fitting procedure we consider two scenarios. In fit 1, only differential cross sections, beam and target asymmetries, and recoil polarizations are taken into account. In a second fit (fit 2), also recent CLAS data on the beam asymmetry [118] and data on the double-polarization observables  $G$ ,  $H$  and  $\Delta\sigma_{31}$  are included. We expect that a comparison of the two fits allows one to see the impact of the recent high-precision data from ELSA, JLab, MAMI, and Spring-8 on the extracted resonance parameters. An overview of the two fits performed in this study can be found in table 1. The observables  $E$ ,  $F$ ,  $C_{x'L}$ , and  $C_{z'L}$  are predicted.

The photoproduction data are taken from the GWU/SAID data base [2, 3] where we consider data up to  $E = 2330$  MeV for  $\gamma p \rightarrow \pi^0 p$  and up to  $E = 2260$  MeV for  $\gamma p \rightarrow \pi^+ n$ . (The CNS/DAC group at GWU includes data up to higher energies.) For the reaction with final state  $\pi^0 p$  ( $\pi^+ n$ ) and for energies  $E > 2050$  MeV ( $E > 1600$ ), we exclude data with forward angles  $\theta < 40^\circ$  ( $\theta < 9^\circ$ ) because in the present approach we do not include partial waves with total angular momentum  $J \geq 11/2$ . A detailed look at the two data sets in question is provided in fig. 2, where results of our fit 2 are shown together with those of

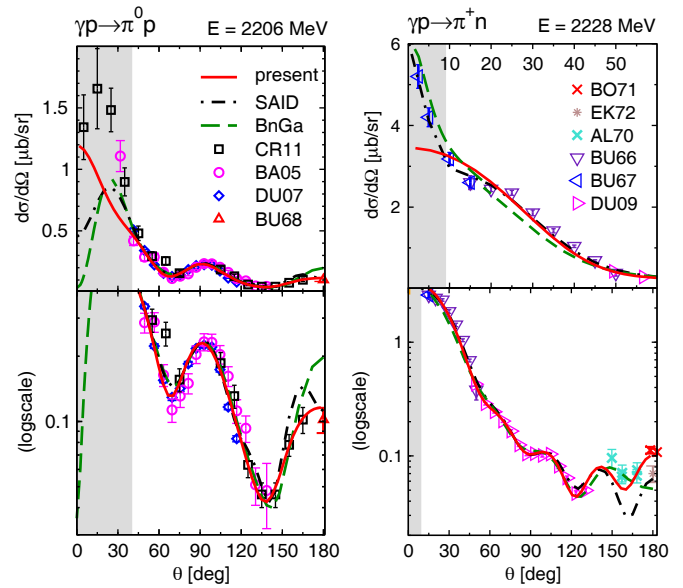


**Fig. 2.** High-energy behavior in the reaction  $\gamma p \rightarrow \pi^0 p$  (left) and  $\gamma p \rightarrow \pi^+ n$  (right). Solid (red) line: fit 2; dash-dotted (black) line: GWU/SAID CM12 [3]; dashed (green) line: Bonn-Gatchina [119]. Data  $\pi^0 p$ : CR11 [120], BA05 [126], DU07 [127], BU68 [128]. Data  $\pi^+ n$ : BO71 [129], EK72 [130], AL70 [131], BU66 [132], BU67 [133], DU09 [134]. The regions excluded in our fit are shown as shaded areas.

the GWU/SAID analysis [3] and the Bonn-Gatchina analysis [119]. As can be seen, for  $\pi^0 p$  none of the approaches is able to describe the forward peak (an experimental confirmation of the data CR11 [120] is needed). In case of  $\pi^+ n$ , on the other hand, the forward peak is well described by the GWU/SAID analysis. Note that the GWU/SAID and the Bonn-Gatchina analyses use prescriptions for partial waves with  $J \geq 11/2$  in terms of Born amplitudes and reggeized exchanges, respectively. We plan to improve the matching to the high energy/low  $t$  region where Regge trajectories provide an economic parameterization of the amplitude [121–125].

No special weights are assigned to any data in both fit 1 and 2. However, some data sets are contradictory to each other as can be seen, *e.g.*, in fig. 3 at the energies 1170 MeV and 1268 MeV. The deviations go beyond an overall normalization, *i.e.* they concern also the angular dependence. To account for such discrepancies we apply an additional systematic error of 5% to all data. Of course, this effectively gives more weight to data with larger errors, such as polarization observables.

In any case, as next step, one would allow for a certain freedom in the normalization of individual data sets as practiced by the CNS/DAC group [2, 3]. We plan to improve our analysis along these lines in the future.

In total, we use 417 free parameters for fit 1 and 388 for fit 2. The parameters are the photon couplings  $g^P$  and  $\lambda^P$  to 11 isospin  $I = 1/2$  resonance states and 10 isospin  $I = 3/2$  resonance states in addition to the non-pole photon couplings  $g_\mu^{\text{NP}}$  and  $\lambda_\mu^{\text{NP}}$  with  $\mu = \pi N, \eta N, \pi \Delta$  for  $I = 1/2$  and  $\mu = \pi N, \pi \Delta$  for  $I = 3/2$ , cf. eq. (15).

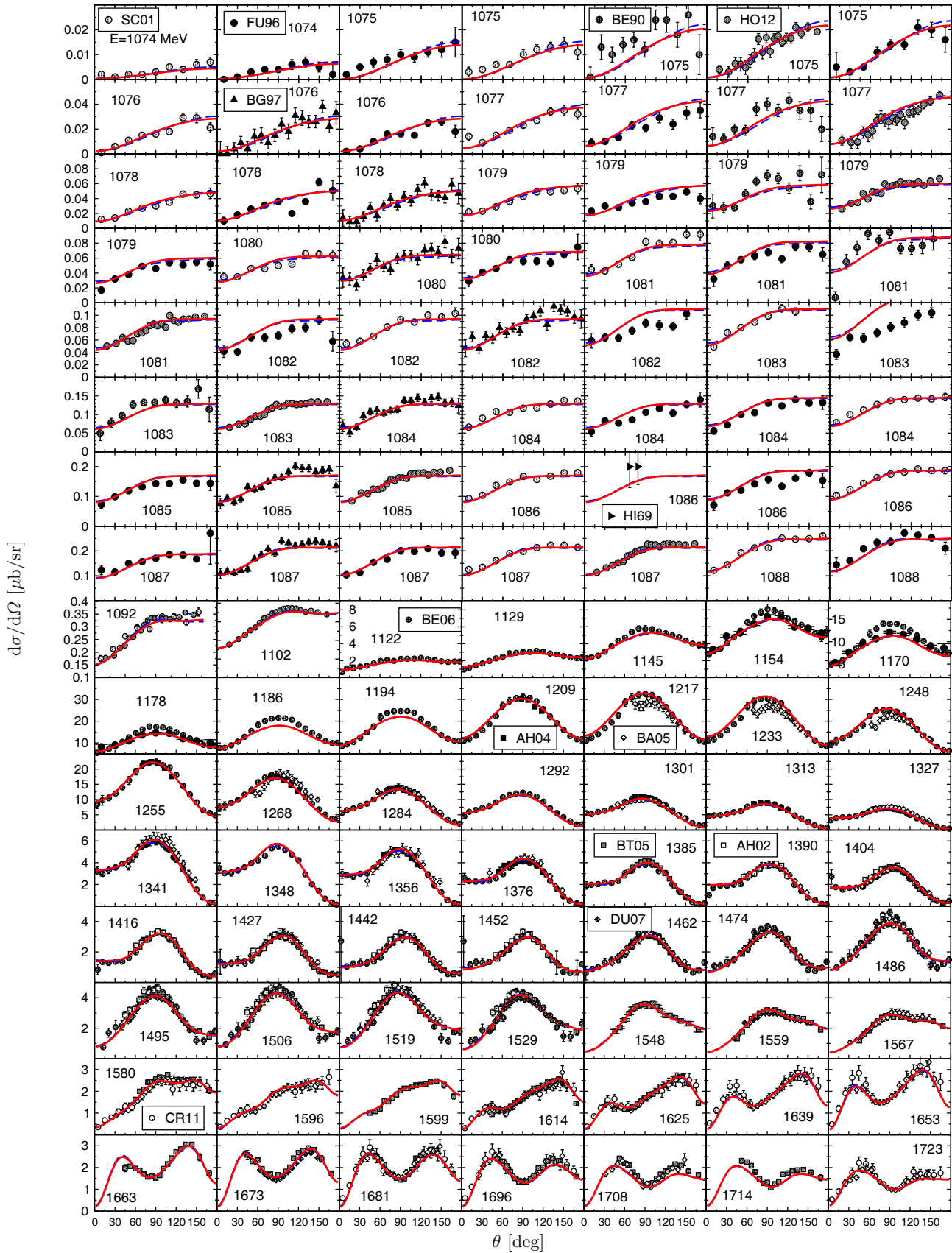


**Fig. 3.** Differential cross section of the reaction  $\gamma p \rightarrow \pi^0 p$ . Dashed (blue) line: fit 1; solid (red) line: fit 2; data: SC01 [135] (MAMI), FU96 [136], BE90 [137], HO12 [138] (MAMI), BG97 [139], HI69 [140], BE06 [141], AH04 [142] (MAMI), BA05 [126] (ELSA), BT05 [143] (GRAAL), AH02 [144] (MAMI), DU07 [127] (JLab), CR11 [120] (ELSA).

It is obvious from eq. (6) that the pole-part can be evaluated from the non-pole part, meaning that for every fit step of parameters tied to the non-pole part, it is most economic to perform a full fit of the parameters tied to the pole part. This was the strategy followed in ref. [79]. Similarly, the photoproduction amplitude  $M$  in eq. (8) is evaluated from the hadronic  $T$ -matrix, that is not altered in the study, and the calculation can be optimized. This is the motivation to perform the decompositions outlined in sect. 2. The photo-excitation of both bare resonances and background is possible as can be seen in eq. (9). We find that for some less prominent resonances it is possible to set the bare resonance excitation  $\gamma_\gamma^c = 0$ . However, for the more prominent ones, we need  $\gamma_\gamma^c \neq 0$  for a good description of the data. In any case, we do not attribute any physical meaning to the individual components of the decompositions into pole and non-pole part.

After convergence of fit 2, we have searched for local minima of  $\chi^2$  in the vicinity of the best parameter set but have not found any. This search was performed by introducing special weights for subsets of data, such that parameters are forced to change. Introducing the original universal weight of one for all data, the fit converged back to the original solution. This procedure also allowed to estimate errors in the photocouplings, as discussed at the end of sect. 3.4.

### 3.2 Fit results

In figs. 3 to 21, we show selected results of the fits to observables. The results compared to the full data base will be made available online [80]. Data sets that differ by less than 10 MeV in scattering energy are depicted in one graph if necessary. If more than one data set from the same experiment lies in the same energy bin, we show only the one closest to the quoted energy. Older data with larger error bars are not displayed in many cases but enter the fitting procedure.

The differential cross section for  $\gamma p \rightarrow \pi^0 p$  is shown in figs. 3 and 4 from threshold up to 2350 MeV. Due to the inclusion of isospin breaking as explained in sect. (2.3), we achieve a satisfactory description of the data even at energies close to threshold. At very high energies ( $E > 2$  GeV) and backward angles, the agreement between data and fit is good, while the fit does not reproduce the forward peak at extreme angles (cf. fig. 2). As explained in the previous section, those data points were excluded from the fits (shaded areas in the figures) because the current approach is limited to partial waves with a total angular momentum of  $J \leq 9/2$ . Higher partial waves would be needed to describe this aspect of the data distribution. The region of forward angles at high energies is then also the only place where differences between fit 1 and fit 2 show up.

By contrast, in case of the differential cross section for  $\gamma p \rightarrow \pi^+ n$ , shown in figs. 5 and 6, small differences between fit 1 and fit 2 are visible at very low energies  $E \leq 1130$  MeV. Small deviations from data, as can be seen, *e.g.*, at  $E = 1131$  or 1240 MeV, are due to inconsistencies among the different data sets.

The beam asymmetry  $\Sigma$  is presented in fig. 7 for the reaction  $\gamma p \rightarrow \pi^0 p$  and in fig. 9 for the  $\pi^+ n$  final state. In figs. 8 and 10 results for the new CLAS data [118] on  $\Sigma$  can be found. These data were not included in fit 1 but only in fit 2. At higher energies  $E \geq 1970$  MeV (fig. 8), fit 2 is clearly better than the prediction of fit 1. The medium-energy regime is predicted/described equally well in both fits. For  $\gamma p \rightarrow \pi^+ n$  (fig. 10), on the other hand, the influence of the new CLAS data is visible at medium energies  $E \sim 1700$  MeV. Here, the description of the forward and backward angles in fit 2 is improved compared to the prediction of fit 1. The same applies to higher energies. Overall, the new CLAS data have a major impact.

The results of the fits to the target asymmetry  $T$  can be found in figs. 11 and 12. Compared to differential cross sections and beam asymmetries, much less data is available for this observable. Although this reduces the influence in the  $\chi^2$  minimization, the agreement of fit and data distribution is good, especially at high energies. Differences between fits 1 and 2 show up predominantly at high energies and in  $\gamma p \rightarrow \pi^+ n$ .

For the recoil polarization  $P$  (see figs. 13 and 14), the data situation is similar to the one of the target asymmetry. For the reaction  $\gamma p \rightarrow \pi^0 p$ , contradicting data sets complicate the task of describing this observable as visible, *e.g.*, at  $E = 1602$  MeV in fig. 13. In regions, where the data is without ambiguity, we achieve a nice description in both fits. At backward angles and higher energies, fit 1 and 2 differ from each other, in  $\pi^+ n$  more than in  $\pi^0 p$ . Additional data could resolve the ambiguity.

In figs. 15 to 17, we display the results for the double-polarization observable  $G$ . This observable was excluded from fit 1. As figs. 15 and 17 show, differences between fit 1 and 2 become larger at higher energies and backward angles, where no data are available. The recent high-precision measurement from CB/ELSA-TAPS [222] is presented in fig. 16. At medium energies, the new CB-ELSA/TAPS data cover almost the whole angular range and the inclusion of  $G$  data in fit 2 has a noticeable impact. In case of  $\gamma p \rightarrow \pi^+ n$ , distinguishable differences between the predictions of fit 1 and the results of fit 2 are confined to angles  $60^\circ < \theta < 90^\circ$ . Note that, compared to  $d\sigma/d\Omega$  or  $\Sigma$ , the number of data points available for this observable is very small for both reactions. It is, thus, not possible to improve the fit if one wants to maintain the same weight for all data points (see, *e.g.* the set at  $E = 1910$  MeV in fig. 17).

Similar considerations apply to the data on the double polarization  $H$  in figs. 18 and 19, that is only included in fit 2. In any case, the agreement between fit and data is acceptable. Again, fit 1 and 2 differ most evidently at backward angles and high energies in  $\pi^0 p$ .

The inclusion of the data for the helicity cross-section difference  $\Delta\sigma_{31}$  which is related to the helicity asymmetry  $E$  (cf. eq. (B.23)) for  $\gamma p \rightarrow \pi^0 p$  (fig. 20) in fit 2, results in a major improvement at energies  $E > 1415$  MeV compared to the prediction of fit 1. This is not the case for  $\gamma p \rightarrow \pi^+ n$  as can be seen in fig. 21. Here, the prediction of fit 1 is good and fit 2 shows only minor improvements.

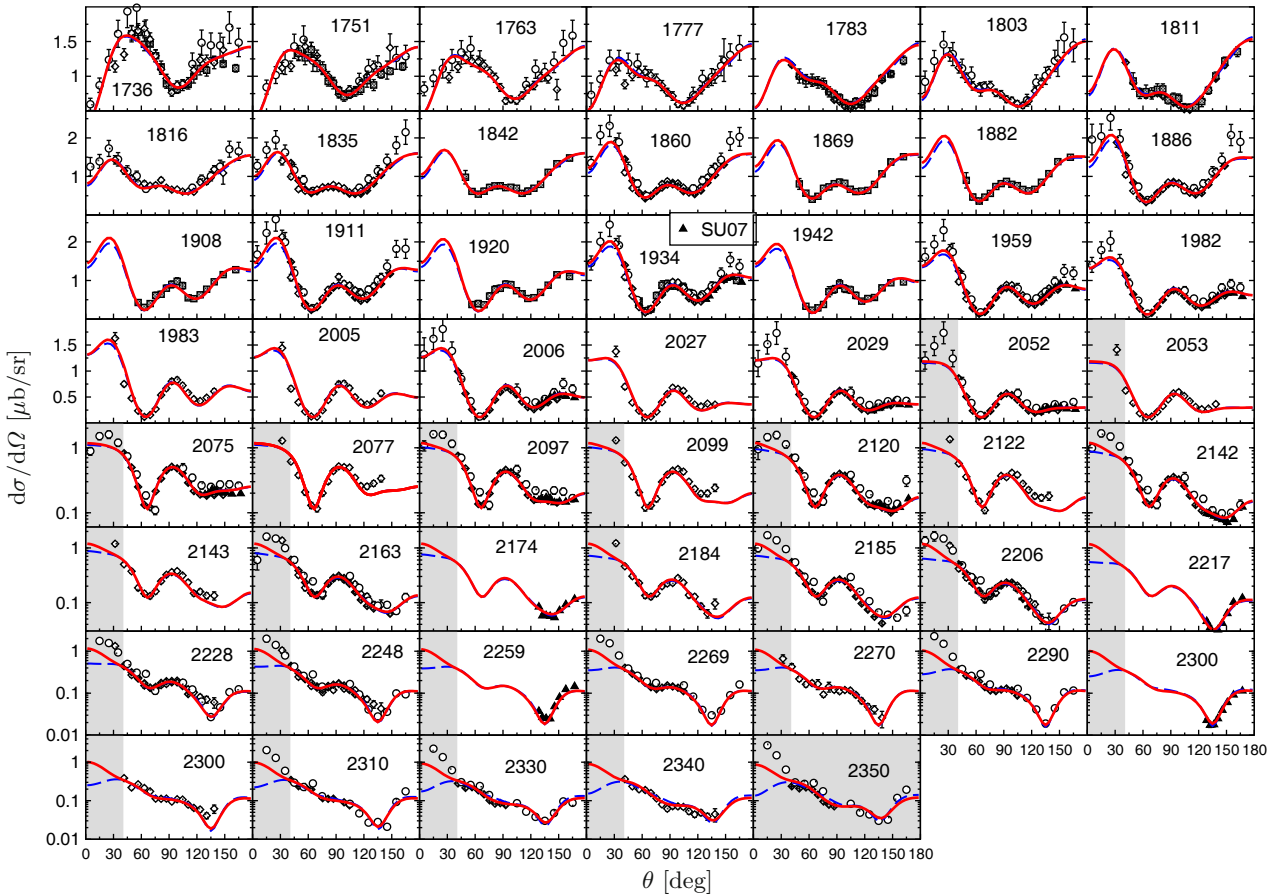


**Fig. 4.** Differential cross section of the reaction  $\gamma p \rightarrow \pi^0 p$ . Dashed (blue) line: fit 1; solid (red) line: fit 2; grey background: data points excluded from the fit; data: cf. fig. 3 and SU07 [145] (SPring-8/LEPS).

In figs. 22 and 23, we present predictions for the double-polarization observables  $E$  and  $F$ . At low energies, the results from fit 1 and 2 are quite similar. With increasing energy, the deviation between the two fits becomes larger, which is an indication for the sensitivity of these observables to small variations of the amplitude. Very recently, data on the double-polarization observable  $E$  for  $\gamma p \rightarrow \pi^0 p$  became available from the CBELSA/TAPS Collaboration [230]. Those data, which were neither included in fit 1 nor in fit 2, are shown in fig. 24 together with our predictions. As said above  $E$  is related to  $\Delta\sigma_{31}$ , and low-energy data on the latter observable are included in fit 2. This explains why the results for that fit are somewhat better than those for fit 1, at least at lower energies. The evident discrepancies at high energies suggest that the inclusion of the CBELSA/TAPS data [230] in a future fit will certainly yield a modification of the amplitudes and, therefore, have an impact on the resulting resonance parameters. Results for this observable from measurements at JLab are expected soon, as well. In fig. 25 the total cross section from ref. [231] and the angle-integrated helicity cross-section difference,  $\Delta\sigma = \sigma_{3/2} - \sigma_{1/2}$ , from ref. [230] are shown. As expected from the good description of the unpolarized differential cross section by both fits 1 and 2, the total cross section  $\sigma$  and our results are in excellent agreement. In contrast, the predictions for  $\Delta\sigma$  deviate at lower energies and reflect the differences in the predic-

tions for  $E$ . Here, fit 2 gives a much better result, while at higher energies, fit 1 is slightly better. The peak at  $E \sim 1700$  MeV is well described by both fits. The broad structure at  $E \sim 1900$  MeV, however, is underestimated by both fits.

Predictions of the beam-recoil polarizations  $C_{x'_L}$  and  $C_{z'_L}$  can be found in figs. 26 and 27 along with recent data from MAMI [232] and JLab [218], and an earlier measurement, also from JLab [217]. Calculations of these observables have been made, *e.g.*, within a quark model [233] or perturbative QCD [234]. Fit 1 and 2 give similar results for  $C_{x'_L}$ , which are also, overall, in fair agreement with the data. For certain details in the data distribution improvements could be achieved by including the data in the fit. The predictions are averaged over the indicated angular bin for the MAMI measurement. For the JLab measurement, however, the observable has been evaluated at the exact angle without averaging, displayed in the plots with thin (red) lines. We observe a strong angular dependence for angles  $\theta > 110^\circ$  and at high energies. With regard to  $C_{z'_L}$ , fit 1 and 2 show larger deviations than for  $C_{x'_L}$ , especially at higher energies. In this case fit 1 seems to be slightly better. Here, the results were not angle-averaged. The rather large difference in the results of fit 2 at  $\theta = 135^\circ$  and at  $\theta = 143^\circ$  (cf. the solid and the dash-dotted lines in fig. 27) illustrates that  $C_{z'_L}$  exhibits a strong angular dependence, as well.

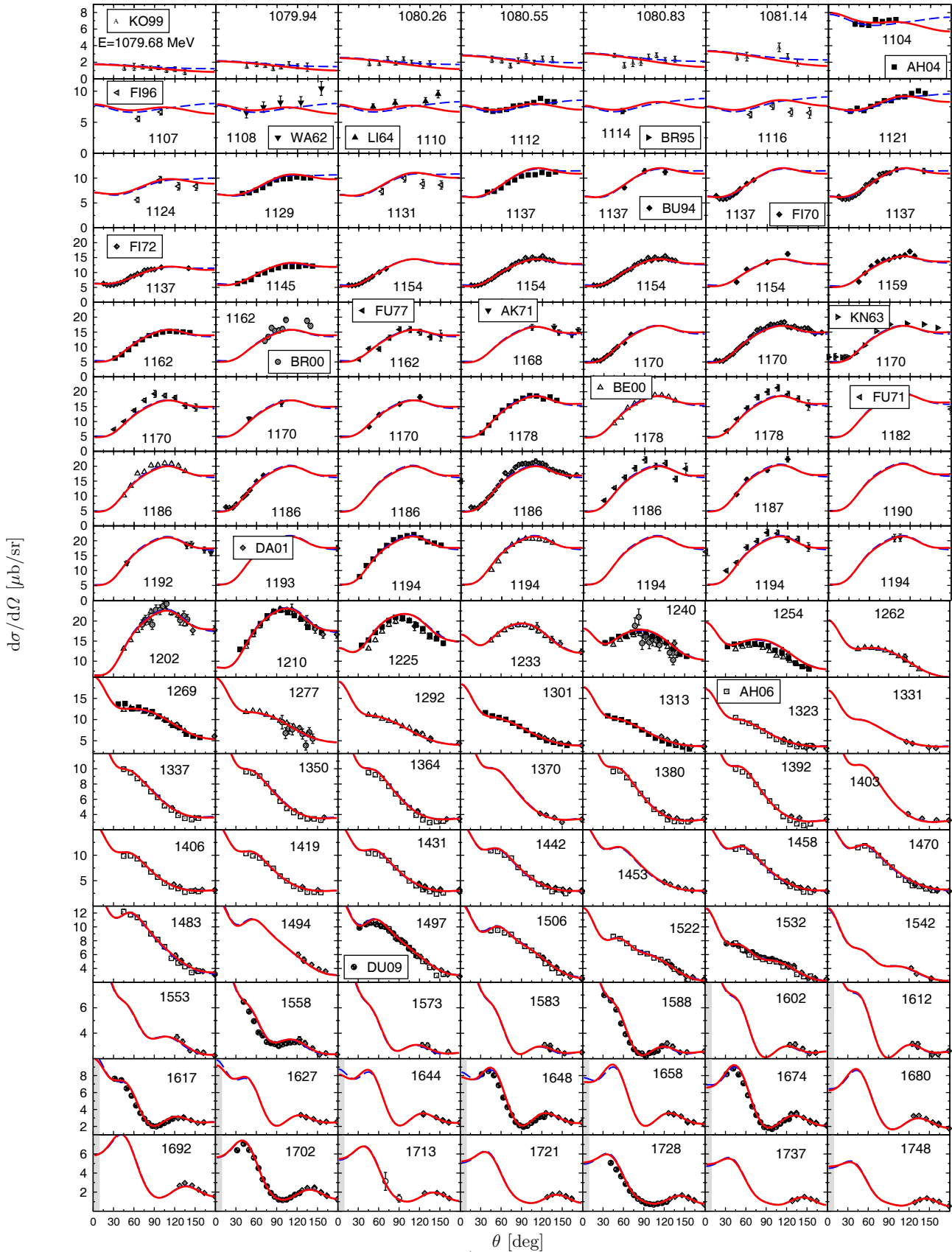


**Fig. 5.** Differential cross section of the reaction  $\gamma p \rightarrow \pi^+ n$ . Dashed (blue) line: fit 1; solid (red) line: fit 2; grey background: data points excluded from the fit; data: KO99 [146], AH04 [142] (MAMI), FI96 [147], WA62 [148], LI64 [149], BR95 [150], BU94 [151], FI70 [152], FI72 [153], BR00 [154] (MAMI), FU77 [155], KN63 [156], BE00 [157] (MAMI), FU71 [158], DA01 [159], AH06 [160] (MAMI), DU09 [134] (JLab).

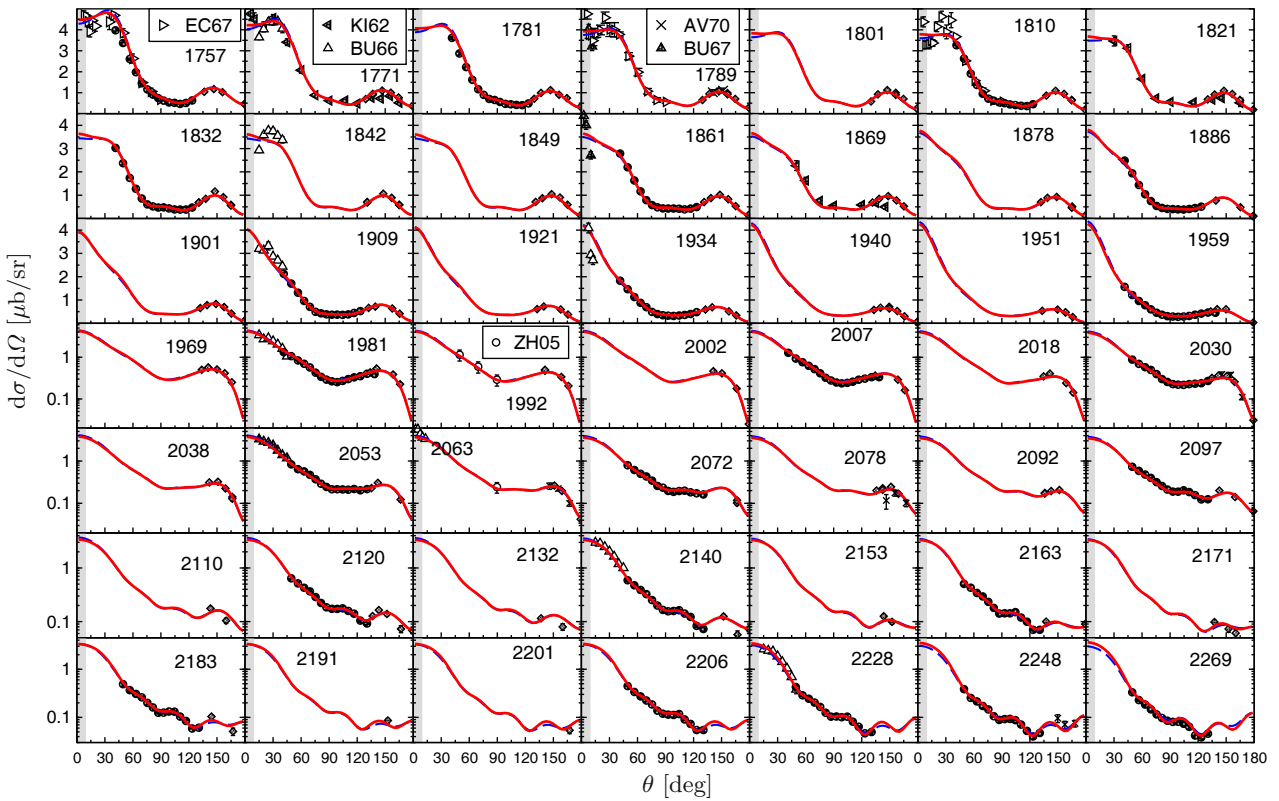


**Fig. 6.** Differential cross section of the reaction  $\gamma p \rightarrow \pi^+ n$ . Dashed (blue) line: fit 1; solid (red) line: fit 2; grey background: data points excluded from the fit; data: cf. fig. 5 and EC67 [161], BU66 [132], KI62 [162], AV70 [163], BU66 [132], ZH05 [164] (JLab).

In general, we observe that fit 1 quite well predicts the data, in particular the new CLAS data on  $\Sigma$  and the double-polarization observables  $G$ ,  $H$ , and  $\Delta\sigma_{31}$ . Still, at the quantitative level, those data have an impact on the resonance properties, once they are included in our fit, as discussed in sect. 3.4. Similar effects can be expected from the inclusion of double polarizations, like  $E$ , or the polarization transfer  $C_{x'_L}$  and  $C_{z'_L}$  in future analyses. Although our predictions of those observables do not deviate strongly from data in most cases, a fit to those data will lead to a more precise determination of the resonance parameters.

### 3.3 Multipoles

In figs. 28 and 29, we show our results for the isospin  $I = 1/2$  and  $3/2$  multipoles together with those of the GWU/SAID CM12 analysis [3]. Single-energy solutions of the latter are available for the lower partial waves. For lower multipoles our solution is similar to the CM12 solution. The most striking example is the dominant  $M_{1+}(3/2)$  multipole. In the electric  $P_{33}$  multipole  $E_{1+}(3/2)$ , however, we observe a structure around 1.65 GeV in both fits that does not show up in the SAID analysis. This structure has its origin in the  $\Delta(1600) 3/2^+$ , a resonance which is dynamically generated in the Jülich2012 coupled-channels model [79]. Since this resonance couples predominantly to

the  $\pi\Delta$  channel, no effect of it was seen in the elastic  $\pi N P_{33}$  partial wave, as discussed in the analysis of ref. [79] where only hadronic channels were considered. However, the  $\gamma N \rightarrow \pi\Delta$  transition is large, making the resonance structure visible in photoproduction. Preliminary results of a new parameterization of the MAID approach suggest a similar structure [235]. In case of the electric and magnetic  $D_{15}$  multipoles  $E_{2+}(1/2)$  and  $M_{2+}(1/2)$  the solutions of fit 1 and 2 deviate at  $E \sim 1.3$  GeV in the real part of the amplitude. At such —comparably low— energies a full dynamical coupled-channels analysis would probably give a result, that is more constrained due to the explicit inclusion of Born terms that can account for a large part of the low-energy dynamics [97]. Further deviations from the SAID solution can be found, *e.g.*, in  $M_{1+}(1/2)$  or in  $E_{2+}(3/2)$  and  $M_{2+}(3/2)$ . Here, fit 1 and 2 also give different results. Note that the relatively sharp spike in the real part of the  $M_{1+}(1/2)$  multipole is an artifact of the isospin-symmetric representation of the multipoles in the plot. The physical  $P$ -waves are all smooth and well behaved close to the thresholds, as fig. 31 demonstrates.

The higher multipoles starting with  $E_{3+}$  are less well determined. With the exception of  $M_{3+}(3/2)$ , larger deviations between our fits on the one hand and between our fits and the SAID solution on the other hand can be observed, as well as a strong energy dependence. The scale, especially for the imaginary parts, is much smaller than the scale of the lower multipoles, though.

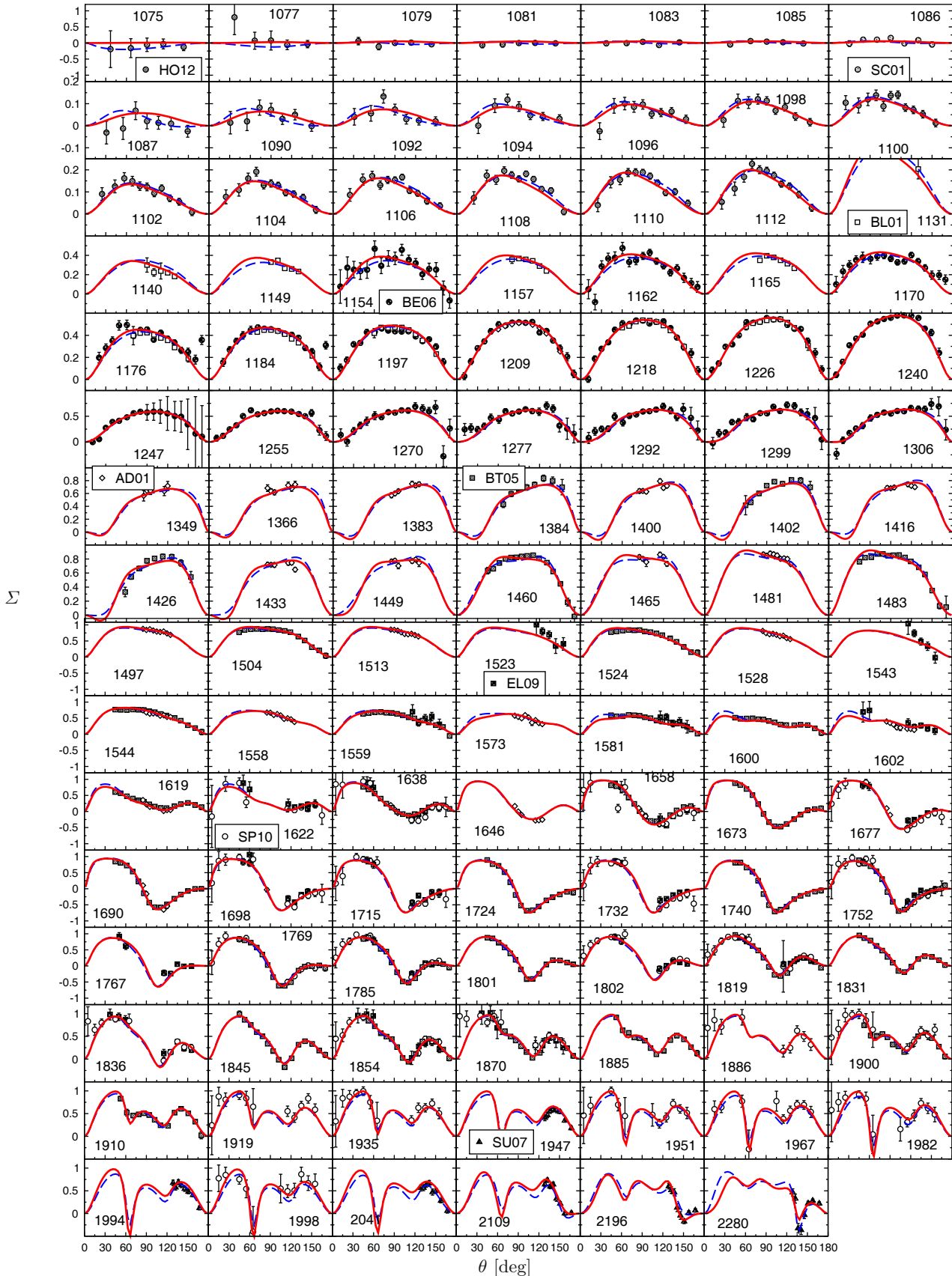


**Fig. 7.** Beam asymmetry of the reaction  $\gamma p \rightarrow \pi^0 p$ . Dashed (blue) line: fit 1; solid (red) line: fit 2; data: HO12 [138] (MAMI), SC01 [135], BL01 [165] (LEGS), BE06 [141] (MAMI), AD01 [166], BT05 [143] (GRAAL), EL09 [167] (ELSA), SP10 [168] (ELSA), SU07 [145] (SPring-8/LEPS).

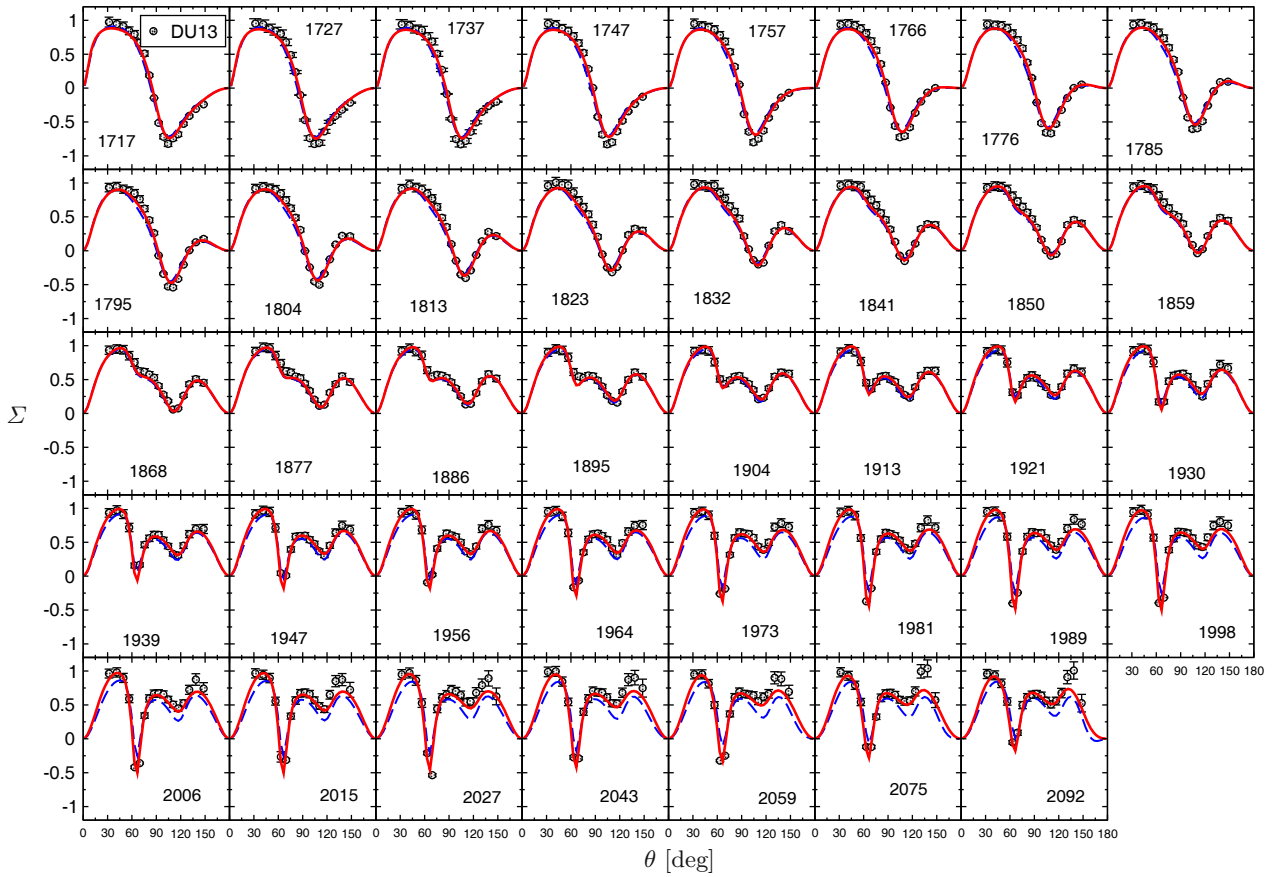


**Fig. 8.** Beam asymmetry of the reaction  $\gamma p \rightarrow \pi^0 p$ . Dashed (blue) line: fit 1 (prediction); solid (red) line: fit 2; data: DU13 [118] (CLAS).

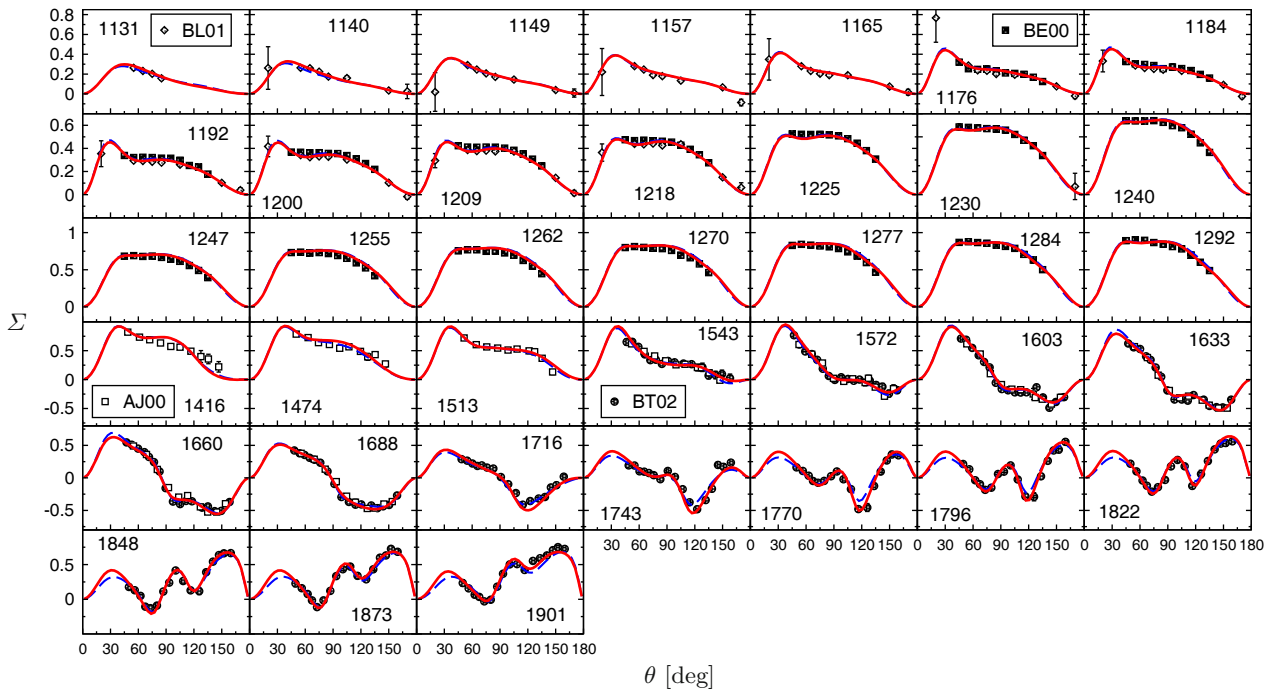


**Fig. 9.** Beam asymmetry of the reaction  $\gamma p \rightarrow \pi^+ n$ . Dashed (blue) line: fit 1; solid (red) line: fit 2; data: BL01 [165] (LEGS), BE00 [157] (MAMI), AJ00 [169] (GRAAL), BT02 [170] (GRAAL).

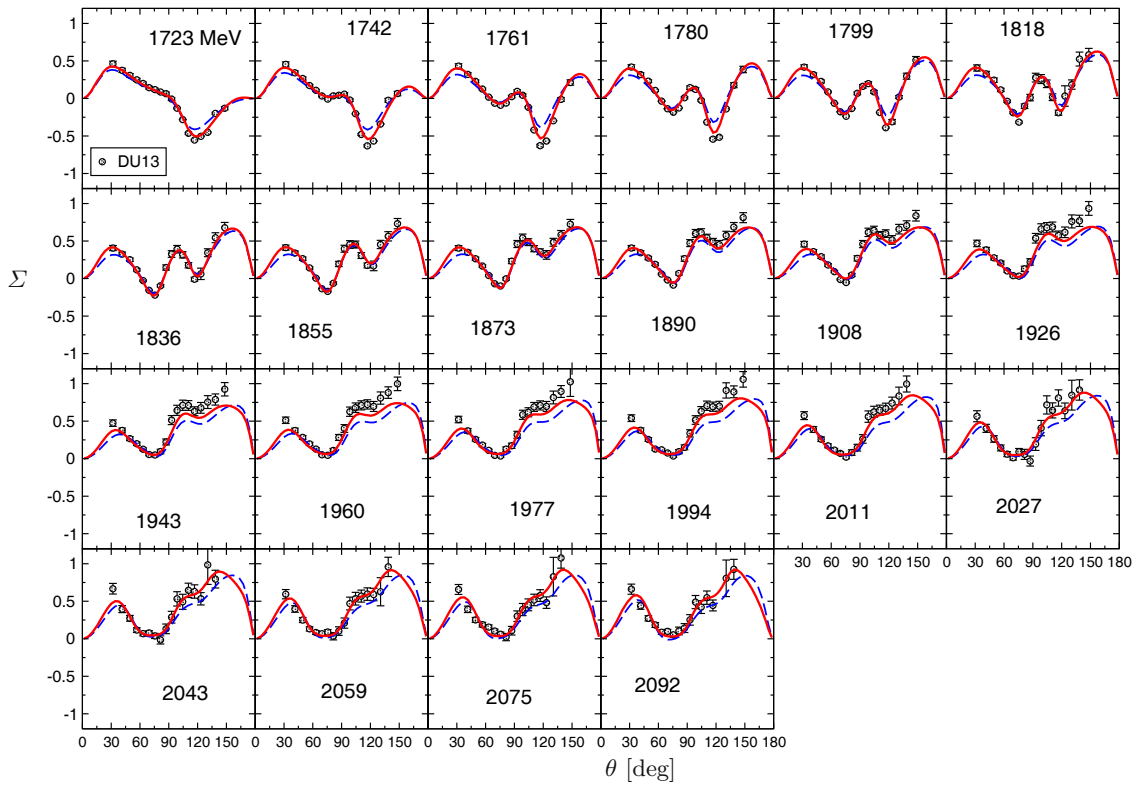


**Fig. 10.** Beam asymmetry of the reaction  $\gamma p \rightarrow \pi^+ n$ . Dashed (blue) line: fit 1 (prediction); solid (red) line: fit 2; data: DU13 [118] (CLAS).

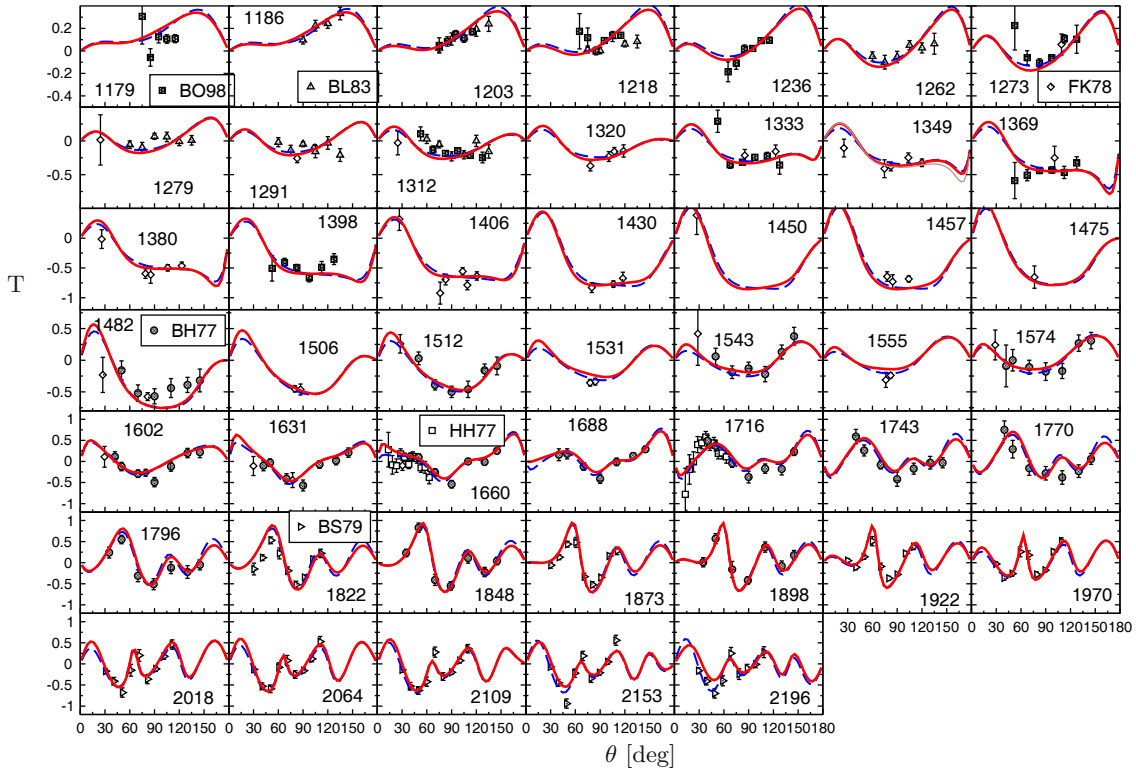


**Fig. 11.** Target asymmetry of the reaction  $\gamma p \rightarrow \pi^0 p$ . Dashed (blue) line: fit 1; solid (red) line: fit 2; data: BO98 [171], BL83 [172], FK78 [173], BH77 [174], HH77 [175], BS79 [176].

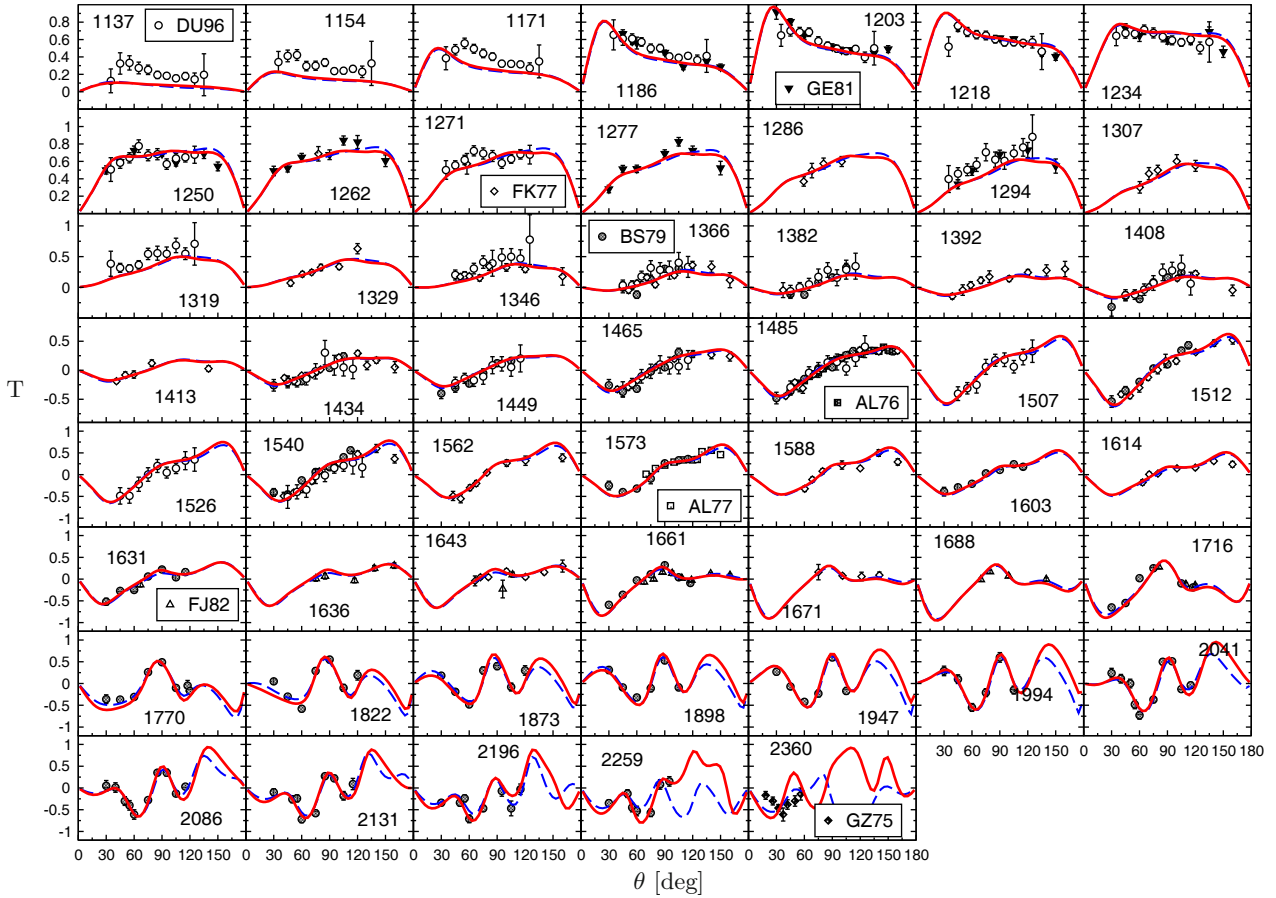


**Fig. 12.** Target asymmetry of the reaction  $\gamma p \rightarrow \pi^+ n$ . Dashed (blue) line: fit 1; solid (red) line: fit 2; data: DU96 [177], GE81 [178], FK77 [179], BS79 [180], AL76 [181], AL77 [182], FJ82 [183].

The threshold region of the  $E_{0+}(\pi^0 p)$  multipole in the particle basis is presented in fig. 30. Note that we only adjust to experimental observables and not to any of the extracted points from analyses shown in the figure (the same applies to fig. 31). Due to its smallness, the  $E_{0+}(\pi^0 p)$  multipole enables very sensitive tests of the photoproduction amplitude and has been addressed in several experimental and theoretical analyses. Precise experimental data are available from MAMI [138], for earlier measurements see refs. [135, 139]. Within the framework of chiral perturbation theory,  $E_{0+}(\pi^0 p)$  close to threshold has been calculated in the fundamental works of refs. [21–27, 236]. More recent ChPT calculations can be found in refs. [32–34]. The role of  $D$ -waves has been discussed in refs. [35, 53]. ChPT calculations including isospin breaking have been performed in refs. [28–30] and relativistic chiral perturbation theory has been applied in ref. [32]. The new ChiralMAID approach [33] includes also electroproduction of charged pions. ChPT in two-pion photoproduction has been pioneered in refs. [24, 26] and nowadays ChPT calculations for photoproduction even on the tri-nucleon system have become possible [237].

Predictions of  $E_{0+}$  from a dispersion-relation calculation can be found in ref. [238] and in ref. [239] the threshold region has been described within a dynamical model for  $\pi^0$  photo- and electroproduction.

As visible in fig. 30, the opening of the  $\pi^+ n$  channel produces a kink in the  $\pi^0 p$  multipole amplitude. For the real part of  $E_{0+}$ , we note strong correlations between the value at the  $\pi^+ n$  threshold and the slope: A small value in combination with a small slope (fit 1) leads to a very similar  $\chi^2$  as a rather large negative value and slope (fit 2), adjusting the higher multipoles at the same time, of course.

The imaginary part of  $E_{0+}$  in fit 2 is in good agreement with the high-precision determination of refs. [28, 30] although it has to be stressed that in the latter works isospin breaking effects beyond those considered here are included. The small imaginary part below the  $\pi^+ n$  threshold originates from a non-vanishing  $\pi^0 p \rightarrow \pi^0 p$  transition, cf. fig. 1. In this context let us mention that the isoscalar scattering length of the Jülich2012 model [79] which enters into this calculation is with  $a_{0+}^+ = -16.6 \cdot 10^{-3} M_{\pi^+}^{-1}$  very small, but it is still twice as large as the recent high-precision ChPT result [29] of  $a_{0+}^+ = (7.6 \pm 3.1) \cdot 10^{-3} M_{\pi^+}^{-1}$ .

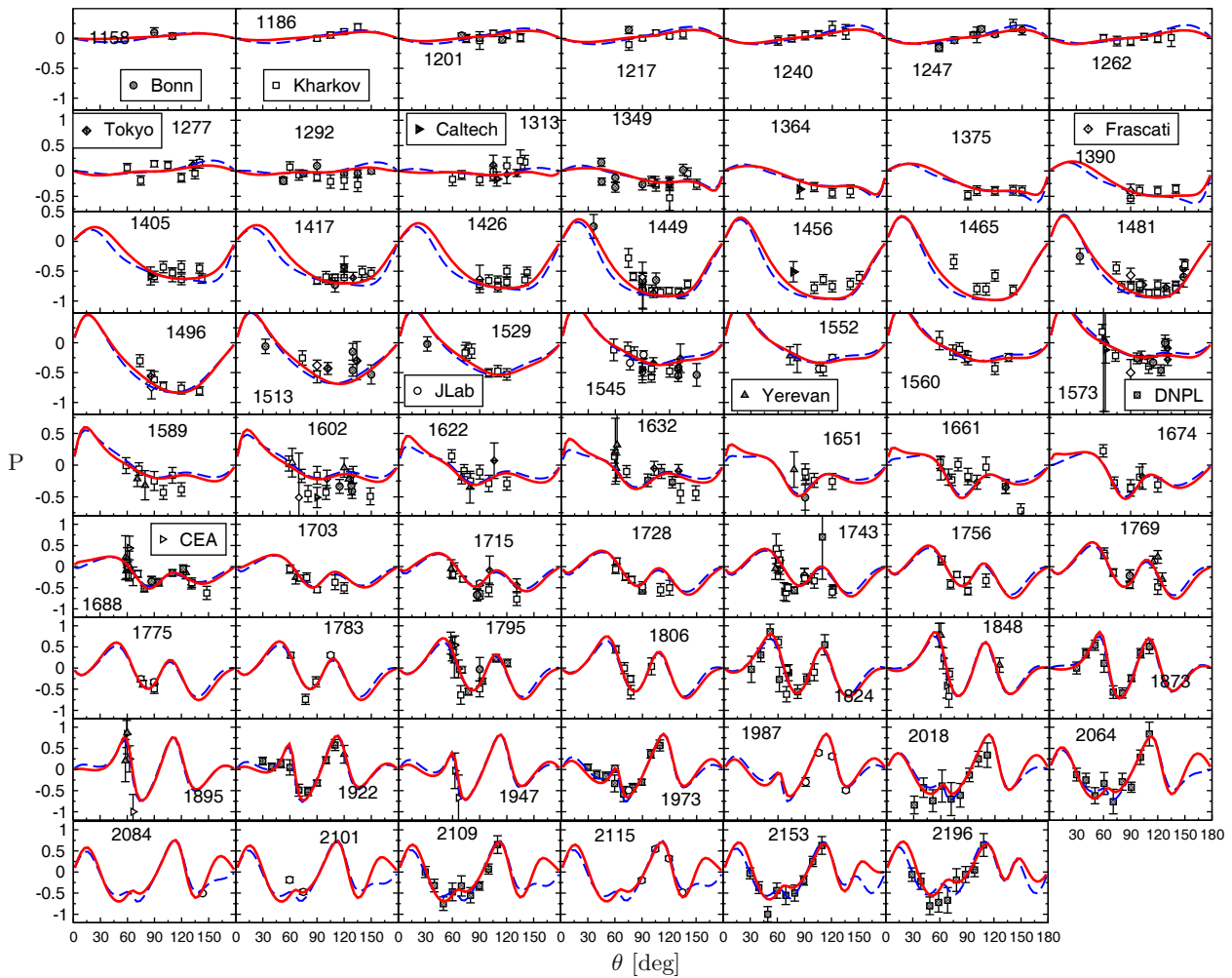


**Fig. 13.** Recoil polarization of the reaction  $\gamma p \rightarrow \pi^0 p$ . Dashed (blue) line: fit 1; solid (red) line: fit 2; data from Bonn [184–188], Kharkov [172, 189–203], Tokyo [204–206], Caltech [207, 208], Frascati [209, 210], Yerevan [211–216], JLab [217, 218], DNPL [176, 219], and CEA [220].

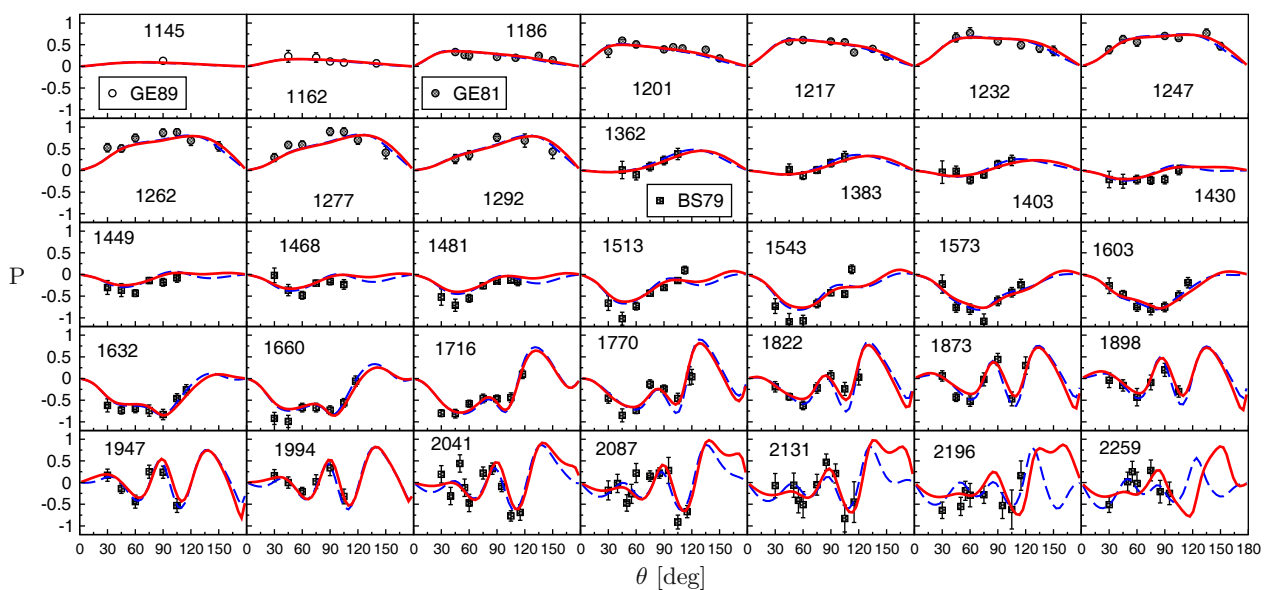


**Fig. 14.** Recoil polarization of the reaction  $\gamma p \rightarrow \pi^+ n$ . Dashed (blue) line: fit 1; solid (red) line: fit 2; data: GE81 [178], GE89 [221], BS79 [180].

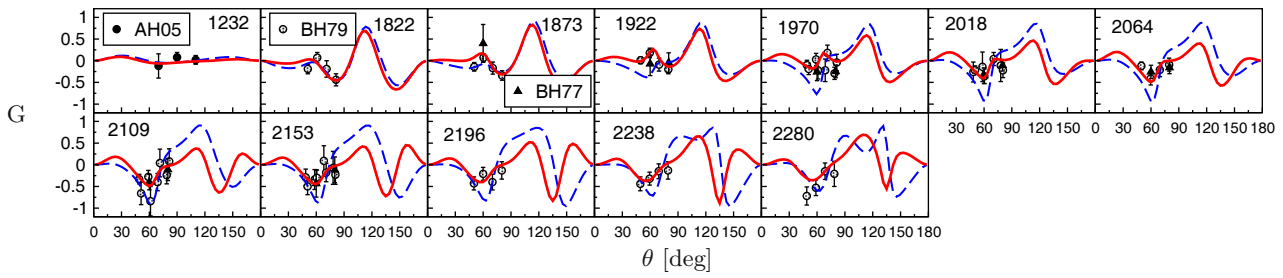


**Fig. 15.** Double polarization  $G$  of the reaction  $\gamma p \rightarrow \pi^0 p$ . Dashed (blue) line: prediction based on fit 1; solid (red) line: fit 2; data: AH05 [223] (MAMI), BH79 [224], BH77 [225].

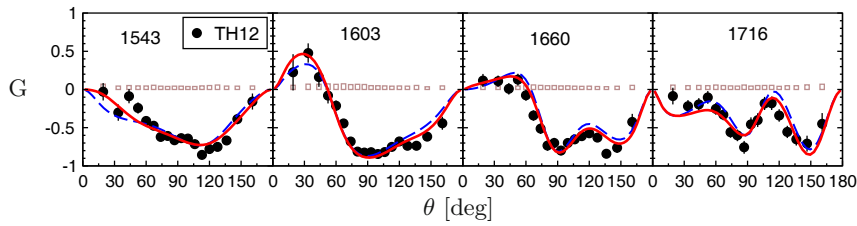


**Fig. 16.** Double polarization  $G$  of the reaction  $\gamma p \rightarrow \pi^0 p$ . Dashed (blue) line: prediction based on fit 1; solid (red) line: fit 2; data: TH12 [222] (ELSA). Systematic errors are separately shown as brown bars.

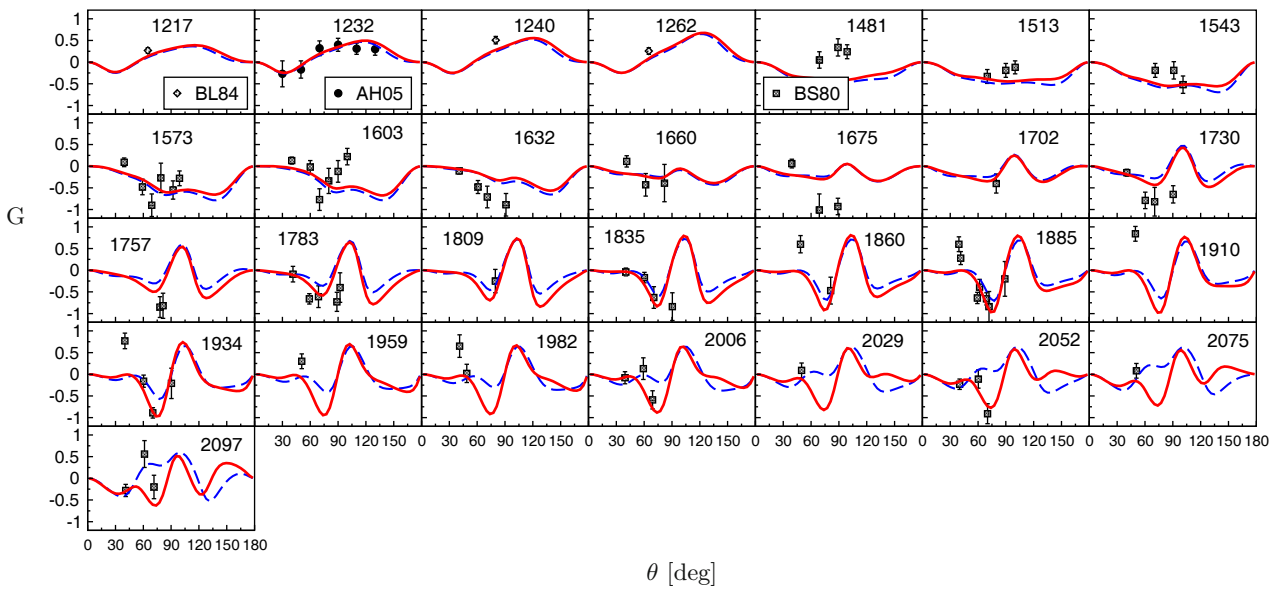


**Fig. 17.** Double polarization  $G$  of the reaction  $\gamma p \rightarrow \pi^+ n$ . Dashed (blue) line: prediction based on fit 1; solid (red) line: fit 2; data: BL84 [226], AH05 [223] (MAMI), BS80 [227].

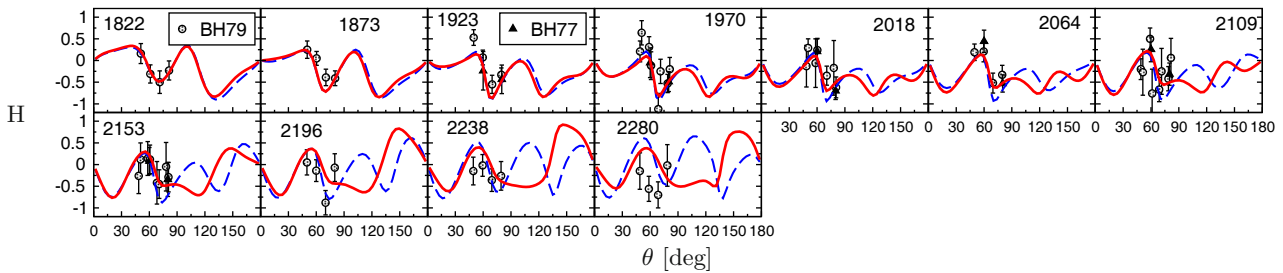


**Fig. 18.** Double polarization  $H$  of the reaction  $\gamma p \rightarrow \pi^0 p$ . Dashed (blue) line: prediction based on fit 1; solid (red) line: fit 2; data: BH77 [225], BH79 [224].

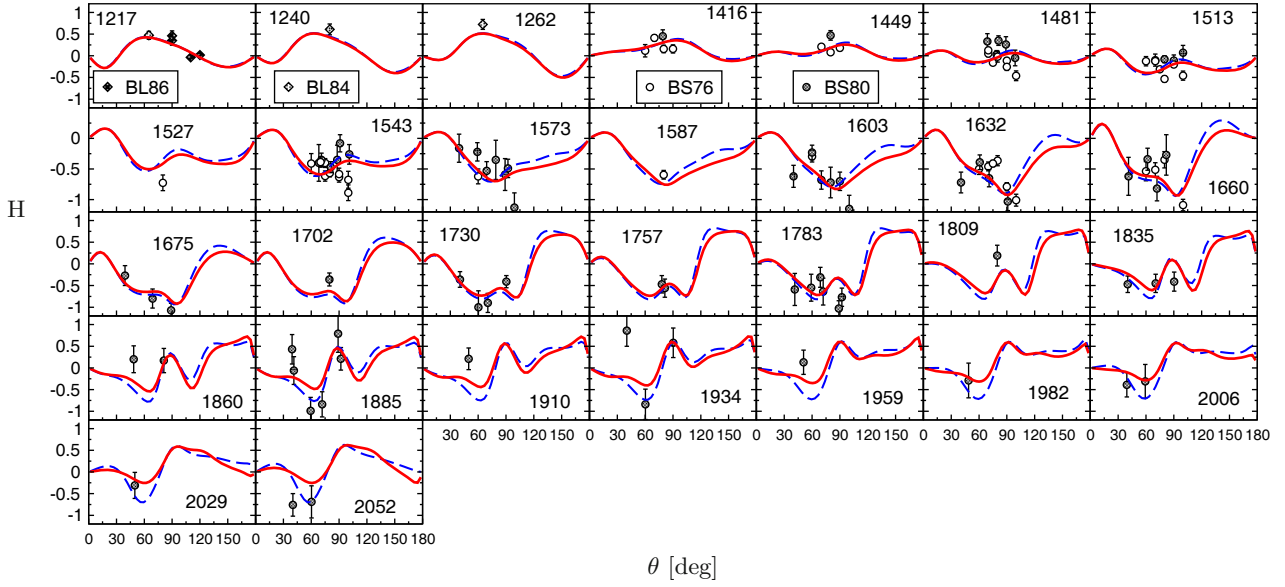


**Fig. 19.** Double polarization  $H$  of the reaction  $\gamma p \rightarrow \pi^+ n$ . Dashed (blue) line: prediction based on fit 1; solid (red) line: fit 2; data: BL86 [228], BL84 [226], BS76 [229], BS80 [227].

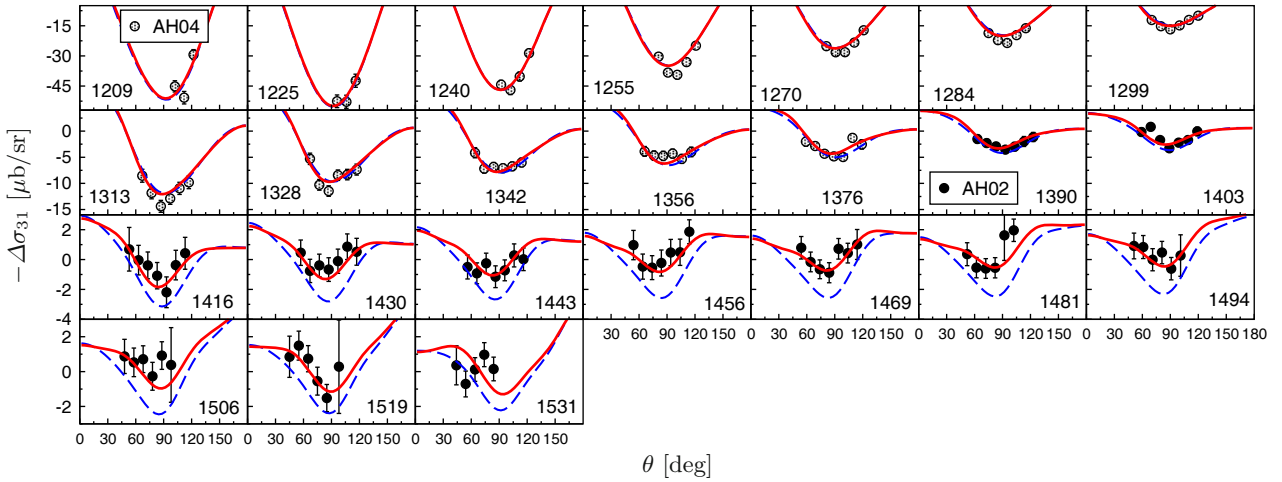


**Fig. 20.**  $\Delta\sigma_{31}$  of the reaction  $\gamma p \rightarrow \pi^0 p$ . Dashed (blue) line: prediction based on fit 1; solid (red) line: fit 2; data: AH04 [142], AH02 [144] (MAMI) (MAMI).

In fig. 31, the  $P$ -wave combinations  $P_1$  to  $P_3$  are shown, divided by the  $\pi^0$  c.m. momentum  $q$ . The  $P_i$  are defined as

$$\begin{aligned} P_1 &= 3E_{1+} + M_{1+} - M_{1-} \\ P_2 &= 3E_{1+} - M_{1+} + M_{1-} \\ P_3 &= 2M_{1+} + M_{1-}. \end{aligned} \quad (21)$$

The data points represent a single-energy analysis of the recent MAMI measurement performed in ref. [138]. Part of the discrepancy between that analysis and our fits certainly comes from employing a different data base. For our analysis, in addition to the data of ref. [138], we also use all data shown in figs. 3 and 7.

Predictions of the  $P$ -wave slopes from low-energy theorems have been pioneered in ref. [25] up to  $\mathcal{O}(q^3)$  and in ref. [240] up to  $\mathcal{O}(q^4)$ . The  $\mathcal{O}(q^3)$  threshold prediction of ref. [240] is shown in fig. 31. For  $P_1$ , the prediction is in agreement with our fits. The deviation in  $P_2$  is presumably due to too small errors of the experimental analysis. In principle one could fit the differences as LECs appear in  $P_1$  and  $P_2$  in the fourth order. For the reason just mentioned we refrain from fitting these LECs here.

One can use the value of  $P_3$  from our fit 2, extrapolated to threshold ( $P_3/q = 11.8 \cdot 10^{-3}/M_\pi^2$ ), to determine the counterterm  $b_P$  [240]. We obtain  $b_P = 14.5 \text{ GeV}^{-3}$  to order  $\mathcal{O}(q^3)$  and  $b_P = 18.0 \text{ GeV}^{-3}$  to order  $\mathcal{O}(q^4)$ . The latter value should be compared to the ones of the  $\mathcal{O}(q^4)$  fits of ref. [240] to older data:  $b_P = 14.9 \text{ GeV}^{-3}$  (Schmidt *et al.* [135]) and  $b_P = 13.0 \text{ GeV}^{-3}$  (Fuchs *et al.* [136]).

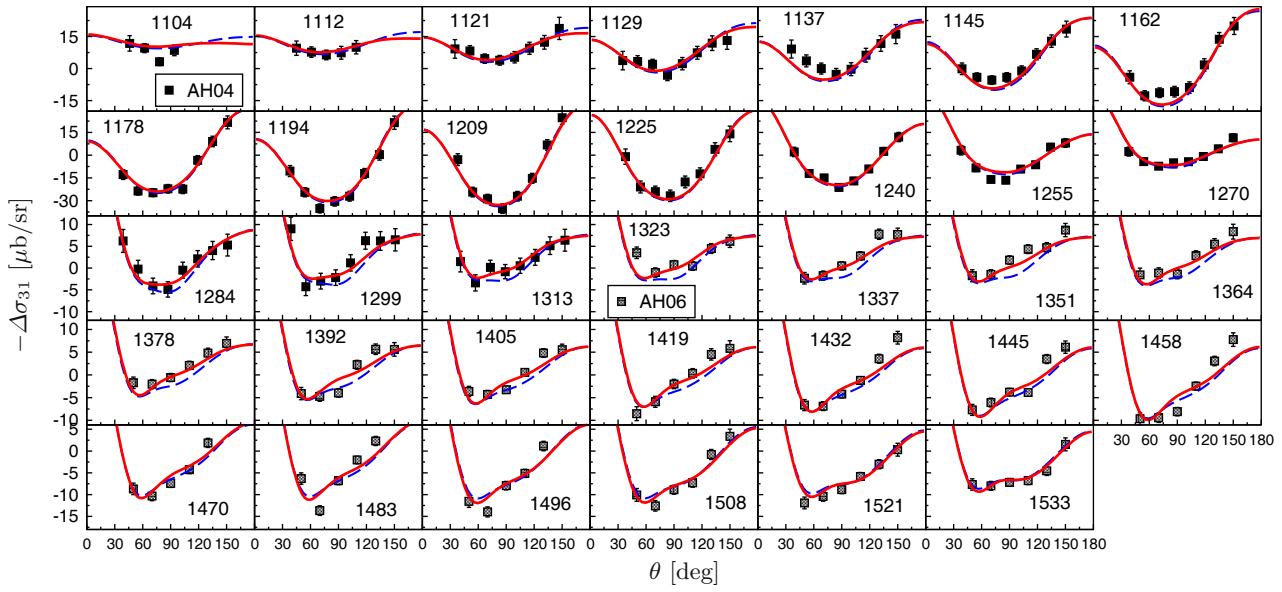


**Fig. 21.**  $\Delta\sigma_{31}$  of the reaction  $\gamma p \rightarrow \pi^+ n$ . Dashed (blue) line: prediction based on fit 1; solid (red) line: fit 2; data: AH04 [142] (MAMI), AH06 [160] (MAMI).

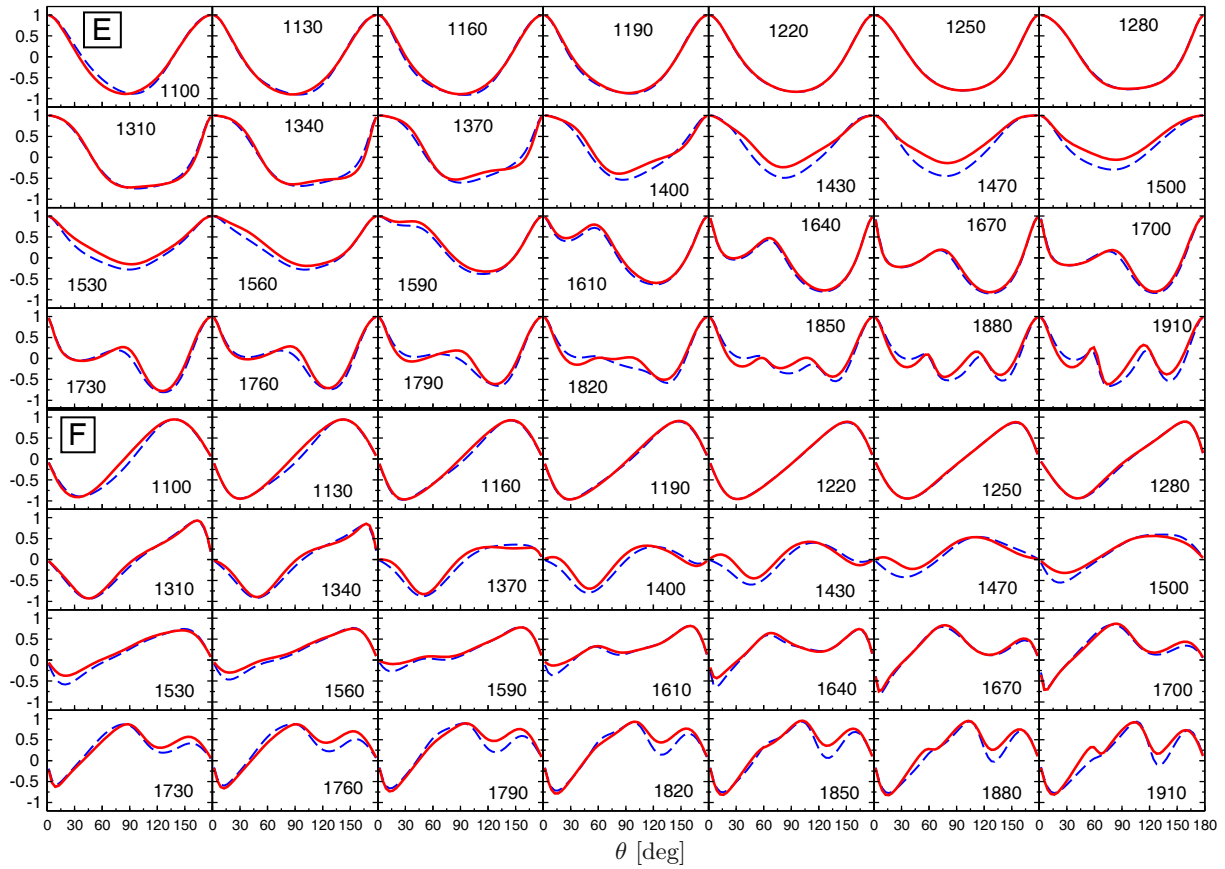


**Fig. 22.** Double polarizations  $E$  (upper 4 rows) and  $F$  (lower 4 rows) of the reaction  $\gamma p \rightarrow \pi^0 p$ . Dashed (blue) line: prediction based on fit 1; solid (red) line: prediction based on fit 2.

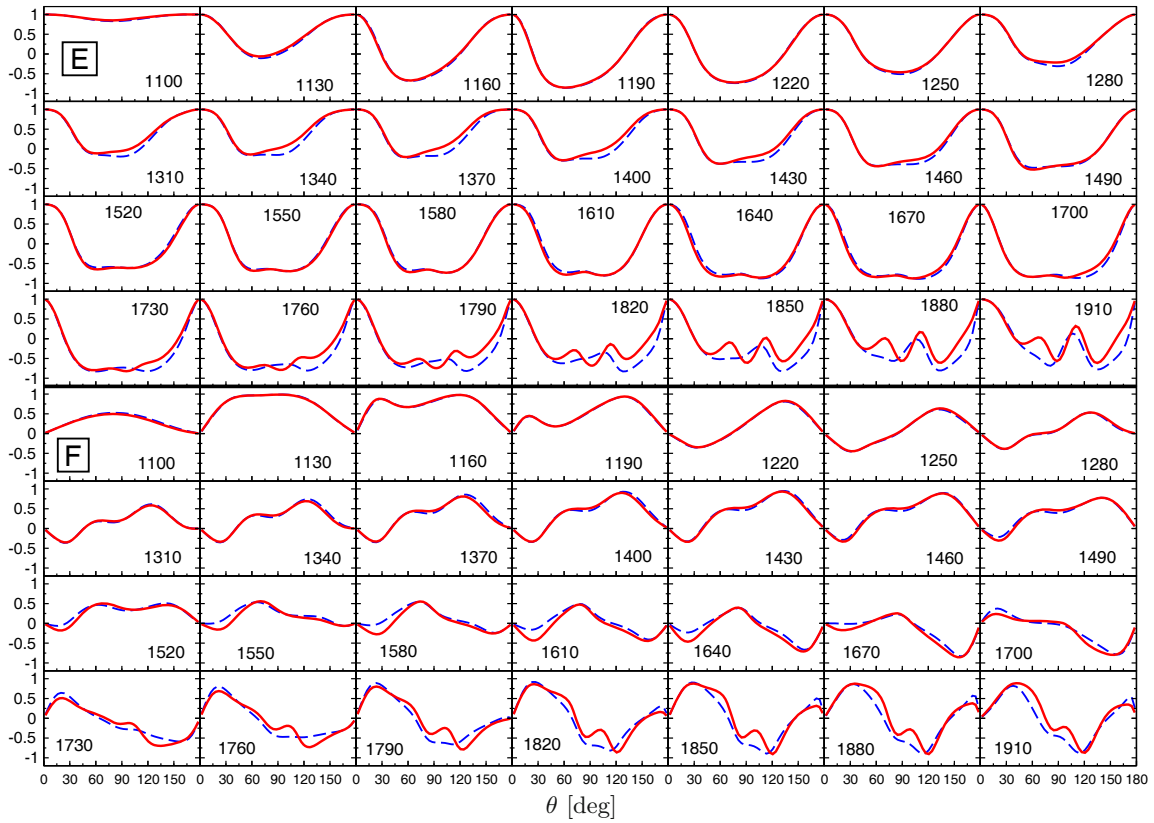


**Fig. 23.** Double polarizations  $E$  (upper 4 rows) and  $F$  (lower 4 rows) of the reaction  $\gamma p \rightarrow \pi^+ n$ . Dashed (blue) line: prediction based on fit 1; solid (red) line: prediction based on fit 2.

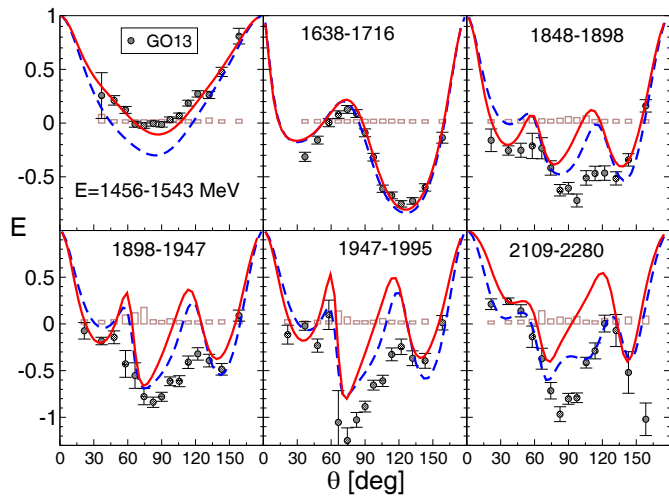


**Fig. 24.** Double polarization  $E$  of the reaction  $\gamma p \rightarrow \pi^0 p$ . Dashed (blue) line: prediction based on fit 1; solid (red) line: prediction based on fit 2; data: GO13 [230] (ELSA). Systematic errors are separately shown as brown bars.

### 3.4 Photocouplings

The photocouplings  $\tilde{A}_{\text{pole}}^h$  (cf. the definition in appendix C) are complex quantities that specify the  $\gamma N$  coupling to a resonance. They are well defined because they

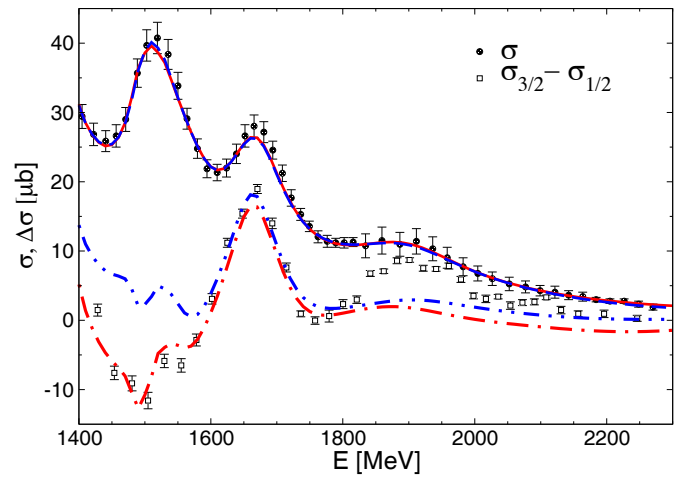


**Fig. 25.** Total cross section  $\sigma$  and the cross-section difference  $\Delta\sigma = \sigma_{3/2} - \sigma_{1/2}$  of the reaction  $\gamma p \rightarrow \pi^0 p$ . Dashed and dash-dot-dotted (blue) line: prediction based on fit 1; solid and dash-dotted (red) line: prediction based on fit 2; data:  $\sigma$  [231],  $\Delta\sigma$  [230] (ELSA).

can be expressed in terms of pole positions and residues of pion photoproduction multipoles and elastic  $\pi N$  scattering amplitudes. The  $\tilde{A}_{\text{pole}}^h$  play the same role as the complex hadronic couplings  $g$  at the pole discussed in ref. [79].

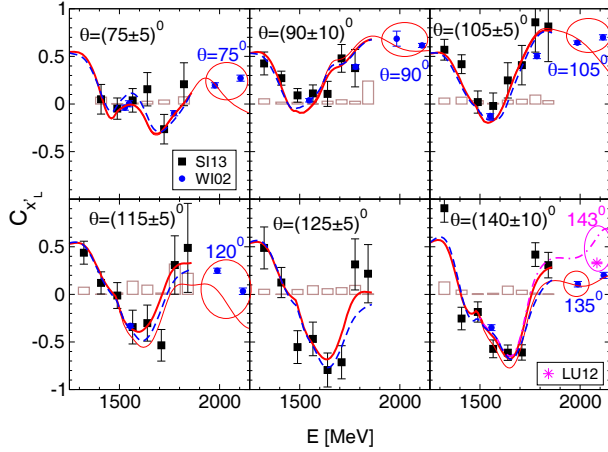


**Fig. 26.** Polarization transfer  $C_{x_L}$  of the reaction  $\gamma p \rightarrow \pi^0 p$ . Note that this observable is defined with respect to the lab frame but shown for different values of the c.m. scattering angle  $\theta$ . Dashed (blue) lines: prediction based on fit 1; solid thick (red) lines: prediction based on fit 2. For both fits, the predictions are angle-averaged as indicated, corresponding to the MAMI angular bins (black squares, SI13 [232]). The thin red lines show the predictions of fit 2 for the JLab 2002 measurements (blue circles, WI02 [217]). The magenta line shows the prediction of fit 2 at  $\theta = 143^\circ$  of the JLab 2012 data point (magenta star, LU12 [218]). Note that the JLab data WI02 [217] are shown here with a reversed sign due to different conventions (cf. appendix B). Systematic errors of the MAMI data SI13 [232] are separately shown as brown bars.

In particular, residues of multipole amplitude  $M_{\mu\gamma}$  have the same factorizing property as the residues of a multi-channel scattering amplitude and can be expressed as the product of the photocoupling  $g_{\gamma N}$  and the resonance coupling to the final state  $\pi N$ , *i.e.*  $\text{Res } M_{\pi N \gamma N} = g_{\pi N} g_{\gamma N}$ . This means that the photocoupling at the pole is entirely independent of the final state of the studied photoproduction reaction.

Photocouplings at the pole are also the quantities to which, *e.g.*, chiral unitary approaches to radiative baryon decays can compare [43, 241–244].

In contrast, the real-valued helicity amplitudes  $A^h$  traditionally quoted [245] depend on the parameterization of the amplitude used in a particular approach. As shown in ref. [246],  $\tilde{A}_{\text{pole}}^h$  becomes real only in case of a pure Breit-Wigner amplitude in the absence of background. In that case,  $\tilde{A}_{\text{pole}}^h = A^h$  [246]. As a side remark, sometimes helicity amplitudes calculated in quark models, real by construction, are compared to the  $A^h$  quoted by the PDG [245]; in view of the unclear physical meaning of the  $A^h$  one should be very cautious when doing that kind of comparison.

In this context, note also that the bare, real couplings  $\gamma_\gamma^c$  in our parameterization of eq. (9) do not have any physical meaning; in particular, they cannot have the meaning of helicity amplitudes of bare resonance states as sometimes claimed in quark model calculations. The bare parameters  $\gamma_\gamma^c$  suffer from the same dependencies on the renormalization scheme and channel space as the bare

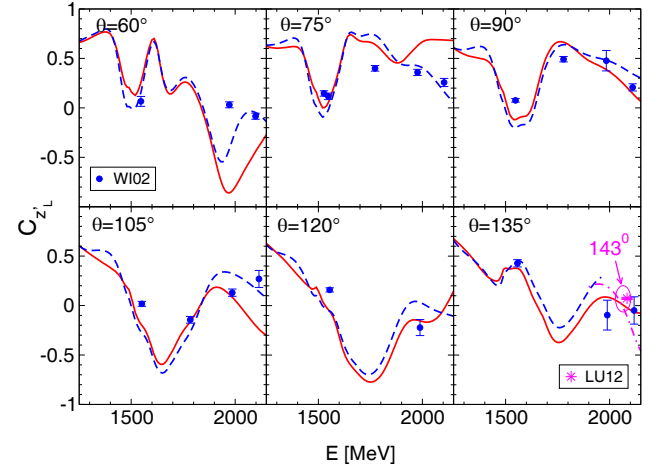


**Fig. 27.** Polarization transfer  $C_{z_L}$  of the reaction  $\gamma p \rightarrow \pi^0 p$ . Note that this observable is defined with respect to the lab frame but shown for different values of the c.m. scattering angle  $\theta$ . Dashed (blue) lines: prediction based on fit 1; solid (red) lines: prediction based on fit 2. Both curves show the prediction for the JLab 2002 data (blue circles, WI02 [217]). The magenta line shows the prediction of fit 2 at  $\theta = 143^\circ$  of the JLab 2012 data point (magenta star, LU12 [218]).

hadronic couplings  $\gamma_{\mu;i}$ . See sects. 4.5 and 4.6 of ref. [79] for a comprehensive discussion of this issue.

In tables 2 and 3, we list the results for the photocouplings at the pole ( $A_{\text{pole}}^h \in \mathbb{R}$ ),

$$\tilde{A}_{\text{pole}}^h = A_{\text{pole}}^h e^{i\vartheta^h}, \quad (22)$$

of the isospin 1/2 and 3/2 resonances calculated in this study together with the pole positions extracted in the Jülich2012 analysis [79]. The analytic continuation is performed with the methods derived in ref. [83]. Additionally, we compare our results to the ones of the Bonn-Gatchina group [55], the recent ANL-Osaka analysis [68] and parameters extracted [246] from an older version of the GWU/SAID multipole analysis [247, 248]. Our conventions for the photocouplings are identical to those of ref. [246] and can be found in appendix C.

In tables 2 and 3, the photocouplings are quoted for both fit 1 and fit 2. For prominent resonances such as the  $N(1535)1/2^-$ , the moduli of the photocoupling are similar in both fits, in contrast to some of the angles, that can differ by more than  $20^\circ$ . Angles are in general less well determined than the magnitude of photocouplings. For less prominent resonances, like the  $N(1710)1/2^+$  or  $\Delta(1930)5/2^+$ , the modulus can change by up to a factor of two. This demonstrates that the recent data from ELSA, JLab, MAMI, Spring-8, and GRAAL, included in fit 2 but not in fit 1, have a major impact on the quantitative determination of resonance properties.

We find small to moderate angles  $\vartheta^h$  for several resonances, among them the  $\Delta(1232)3/2^-$ ,  $N(1650)1/2^-$ ,  $N(1440)1/2^+$ ,  $N(1520)3/2^-$ , in fair agreement with ref. [246]. This has led to speculations [246] that the difference between the (real)  $A^h$  quoted in the Particle Data

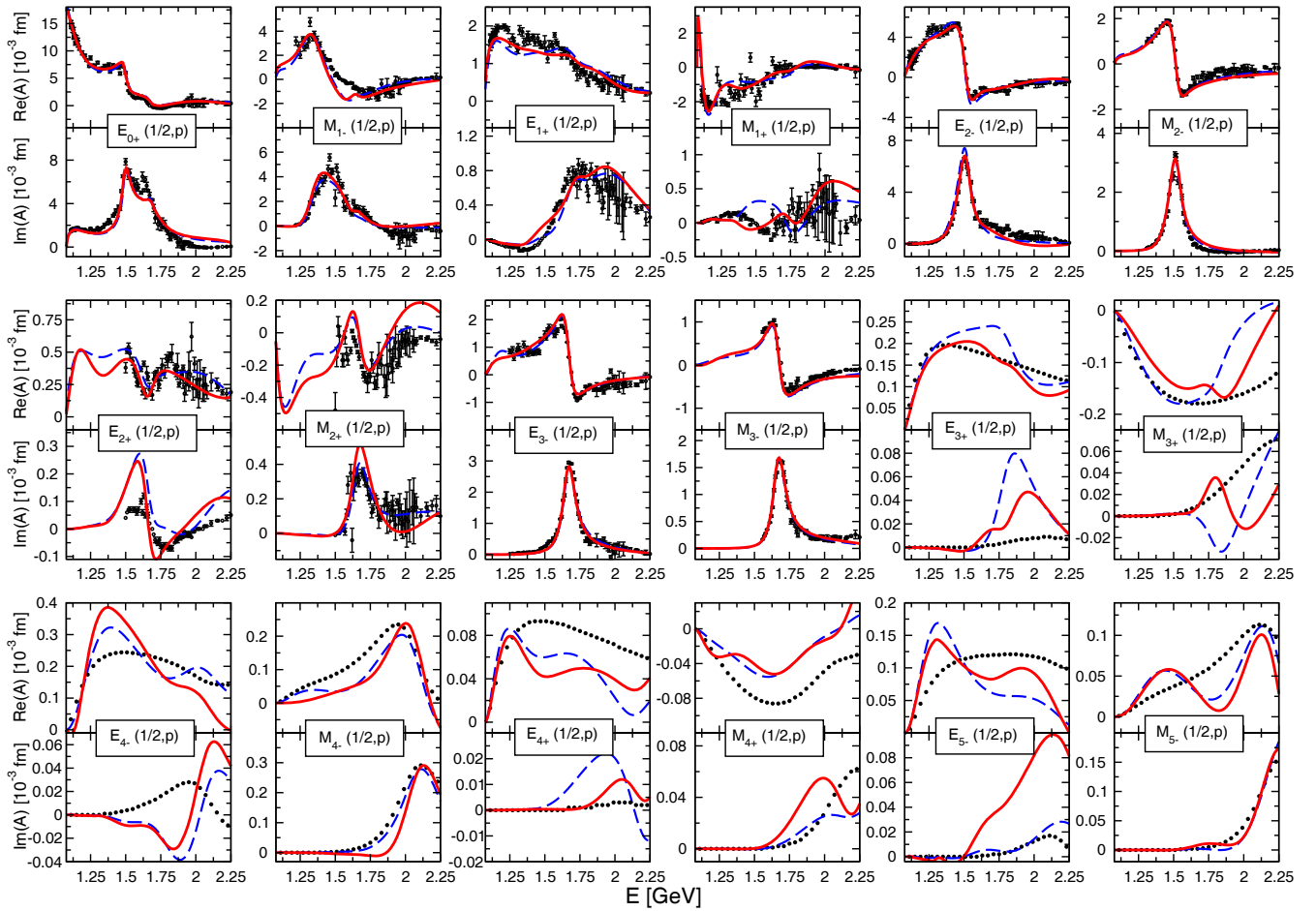


**Fig. 28.** Isospin  $I = 1/2$  multipoles. Points: GWU/SAID CM12 solution [3] (single-energy solution for  $E_{0+}$  to  $M_{3-}$ , energy-dependent solution for  $E_{3+}$  to  $M_{5-}$ ). Dashed (blue) line: fit 1; solid (red) line: fit 2.

Book [245] and the photocouplings at the pole is possibly not large. However, an inspection of tables 2 and 3 reveals that the complex phases are, in general, not really small.

As can be seen in table 2, the real part of the pole position of the  $N(1535)1/2^-$  resonance is similar in all quoted analyses, while the imaginary part in the present approach is rather small. Our  $N(1650)1/2^-$ , on the other hand, is wider compared to other analyses. This illustrates the difficulties to extract pole positions in the  $S_{11}$  partial wave [83]. As a result of the small width of the  $N(1535)1/2^-$  we also obtain a smaller photocoupling  $A_{\text{pole}}^{1/2}$ . The same correlation can be observed for the  $\Delta(1620)1/2^-$  in table 3. Likewise, for the  $\Delta(1232)3/2^+$ , the slightly different pole position in our analysis leads to photocouplings  $A_{\text{pole}}^{1/2}$  and  $A_{\text{pole}}^{3/2}$  slightly different from the ones in the other analyses. In case of the Roper resonance  $N(1440)1/2^+$  our result is in good agreement with the SAID analysis.

The photocoupling of the  $N(1535)1/2^-$  and its  $Q^2$  dependence has been evaluated in the chiral unitary approach of ref. [242]. The resonance appears as a quasi-bound  $KY$  state generated from coupled-channel scattering in the  $\pi N$ ,  $\eta N$ , and  $KY$  channels. The pho-

tocoupling at  $Q^2 = 0$  was predicted to be around  $50 - 75 \cdot 10^{-3} \text{ GeV}^{-1/2}$  with an angle of around  $-35^\circ$  (the values do not change much if evaluated at the pole position, as we have checked). This prediction compares well to the present data analysis, see table 2.

Our value of the photocoupling  $A_{\text{pole}}^{1/2}$  for the  $N(1710)1/2^+$  is rather small. Including kaon photoproduction data into the approach might lead to a different value because in the Jülich2012 analysis [79] a considerable impact of the  $N(1710)1/2^+$  on those channels was observed. A fairly good agreement with the SAID and the Bonn-Gatchina results is found in case of the  $N(1520)3/2^-$ ; the corresponding multipoles  $E_{2-}(1/2)$  and  $M_{2-}(1/2)$  are indeed quite large and seem to be well determined, cf. fig. 28. An agreement with the Bonn-Gatchina group is also observed for the  $N(1675)5/2^-$  and the  $N(1680)5/2^+$ . In contrast, the large  $\gamma N$  coupling of the  $\Delta(1600)3/2^+$  results in photocouplings  $A_{\text{pole}}^{1/2}$  and  $A_{\text{pole}}^{3/2}$  much larger than the ones of the other analyses and is reflected in a resonance-like structure around 1600 MeV in the  $E_{1+}(3/2)$  multipole, see fig. 29. A similar structure has been observed in preliminary results of a new parameterization of the MAID approach [235]. In case of the

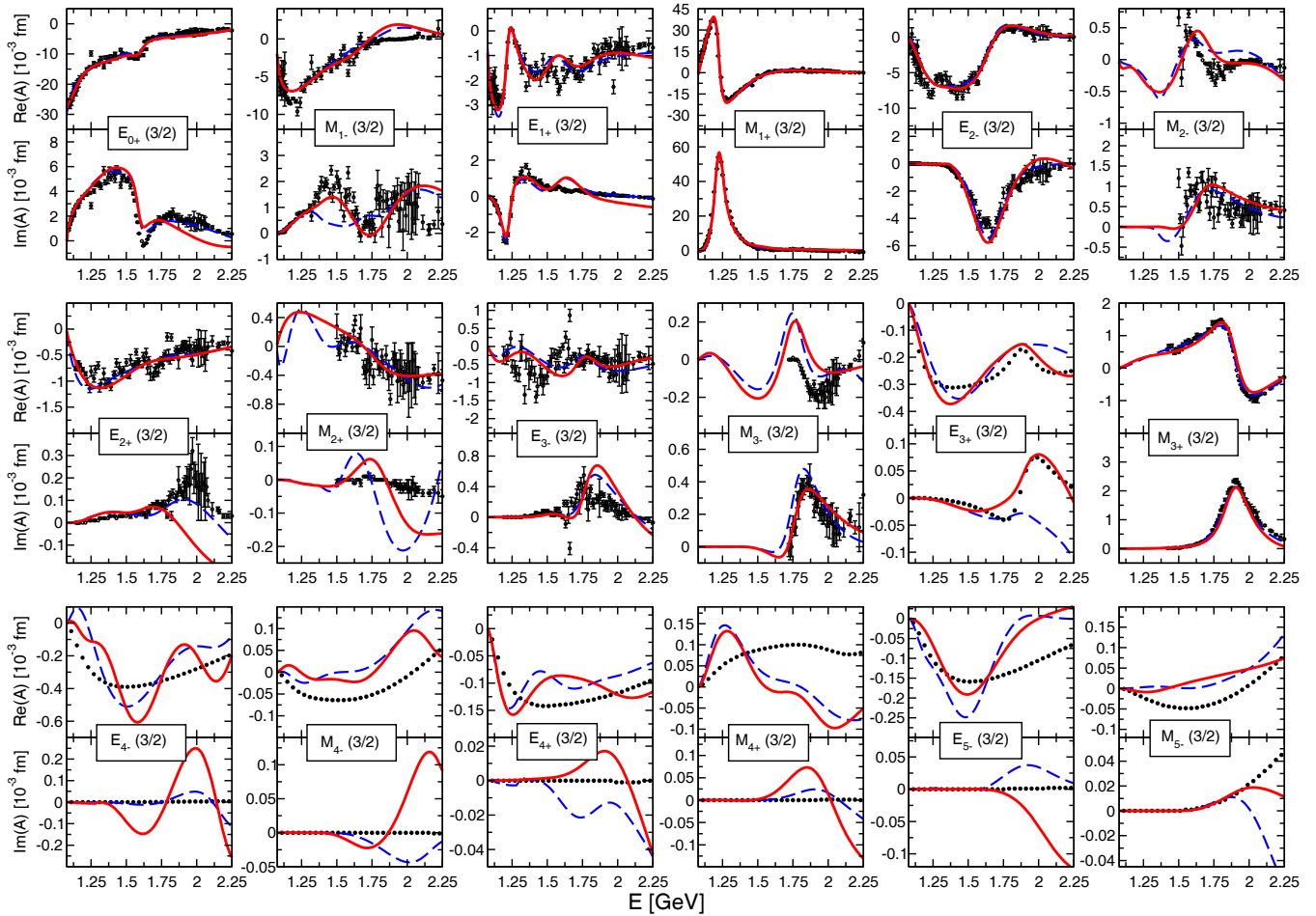


**Fig. 29.** Isospin  $I = 3/2$  multipoles. Points: GWU/SAID CM12 solution [3] (single-energy solution for  $E_{0+}$  to  $M_{3-}$  and for  $M_{3+}$ , energy-dependent solution for  $E_{3+}$  and for  $E_{4-}$  to  $M_{5-}$ ). Dashed (blue) line: fit 1; solid (red) line: fit 2.

prominent  $\Delta(1950)7/2^+$  all analyses obtain similar results.

For some very wide resonances ( $N(2220)9/2^+$ ,  $\Delta(1910)1/2^+$ ,  $\Delta(1920)3/2^+$ ,  $\Delta(1930)5/2^-$ ,  $\Delta(2200)7/2^-$ ,  $\Delta(2400)9/2^-$ ), the photocouplings are sometimes sizable and very different for fit 1 and fit 2. There are very large uncertainties attached to these values, because the higher multipoles themselves are not uniquely determined as seen in the previous section. Second, some of these resonances are not well determined by hadronic data, see the discussion in ref. [79]. Extreme examples are the  $N(1750)1/2^+$  and the  $\Delta(1920)3/2^+$ . Third, as these resonances are so wide, their contribution to the multipole is difficult to disentangle from background terms; partial cancellations of different contributions to a multipole may occur rendering  $A_{\text{pole}}$  unnaturally large. We do not assign much significance to the existence or properties of these resonances [79]. The  $N(2250)9/2^-$  is also very wide, but the resonance shape is clearly visible in the  $\pi N$  partial wave [2] and its properties can be determined more reliably.

In the absence of a reliable tool to bring systematic data uncertainties under control, a rigorous error estimate is not possible. However, one can obtain a qualitative estimate from re-fits based on a re-weighted data set, imposing that the  $\chi^2$  of the re-fit should not deviate from

the best  $\chi^2$  by more than 5%. Altogether, we have performed seven re-fits assigning weights different from one to certain subgroups of observables, such that the 5% criterion is fulfilled. The seven subgroups are the observables  $d\sigma/d\Omega$ ,  $\Sigma$ ,  $T$ ,  $P$ , and  $(\Delta\sigma_{31}, G, H)$ , for both final states, and  $d\sigma/d\Omega$  and  $\Sigma$  only for  $\pi^+n$  in the final state. The errors quoted in tables 2 and 3 reflect the maximal deviations from the values of the best fit, found in any of the re-fits.

As discussed, the absolute size of these errors is not well determined, but the relative size among different resonances indeed helps to assess how reliably the photocouplings at the pole are determined by data. The errors for the lower-lying, well-established resonances are often considerably smaller than for the higher-spin resonances. Also, resonances with a very large width often exhibit larger errors, as, *e.g.*, in case of the  $\Delta(1930)5/2^-$  whose photocoupling is basically undetermined. It should be noted that through the parameterization of eq. (9) resonances and background can be excited independently by the photon, without making assumptions on the underlying dynamics. For wide resonances, this translates generally in larger uncertainty of the photocoupling at the pole, reflecting the inherent difficulty to separate background from resonance contributions in these cases.

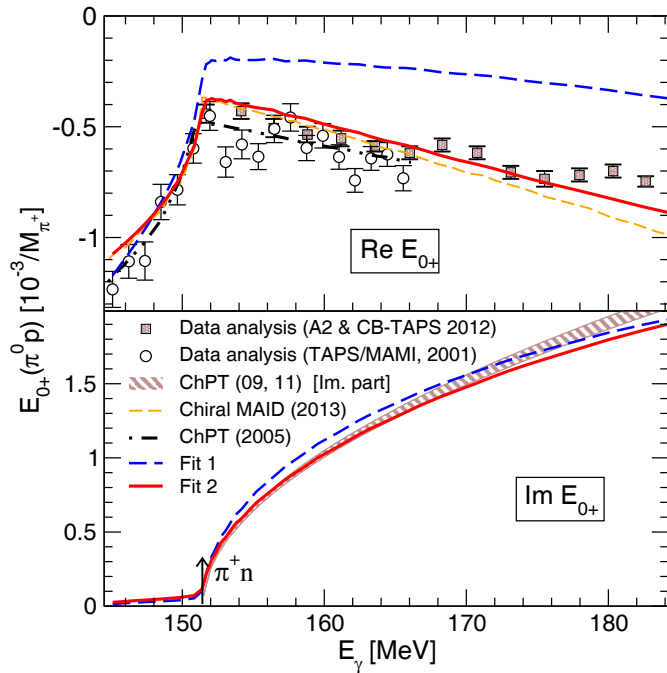


**Fig. 30.** The  $E_{0+}(\pi^0 p)$  multipole close to threshold. The  $\pi^+ n$  threshold is indicated with an arrow. Dashed (blue) line: fit 1; solid (red) line: fit 2. Experimental analyses: A2 and CB-TAPS (2012) [138] and TAPS/MAMI (2001) [135]. Theoretical analyses: Chiral MAID (2013) [33] and ChPT (2005) [27]. The imaginary part (dashed area) is provided in ref. [138] based on the ChPT calculation including isospin breaking of refs. [28,30].

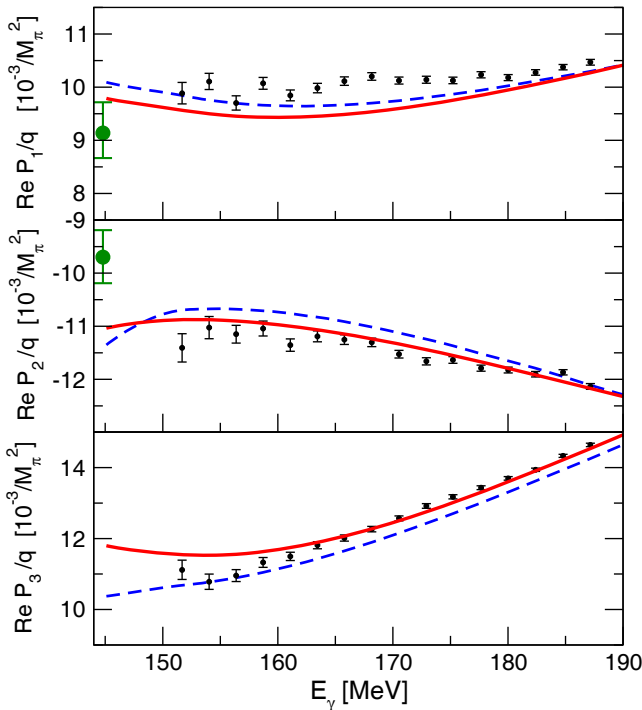


**Fig. 31.**  $P$ -waves for the reaction  $\gamma p \rightarrow \pi^0 p$  close to threshold. Dashed (blue) lines: fit 1; solid (red) lines: fit 2. The data points at threshold (green circles) show the results of the  $\mathcal{O}(q^3)$  calculation of ref. [240]. Data points beyond threshold (black): Phenomenological analysis of the recent MAMI measurement in ref. [138].

## 4 Summary

Photocouplings at the resonance pole are well-defined quantities and, therefore, appropriate to specify the electromagnetic excitations of resonances. They are given as ratios of residues that, together with pole positions, characterize resonances. The corresponding values are necessarily complex. To determine the photocouplings, a reliable analytic continuation to the resonance poles is needed. Here, we rely on the Jülich2012 dynamical coupled-channel model which guarantees unitarity and analyticity, and incorporates general  $S$ -matrix principles such as the correct branch points on the real axis and in the complex plane.

In the present study of pion photoproduction, we have chosen a highly flexible, model-independent form of the photo excitation inspired by the GWU/DAC CM12 parameterization. This enables an accurate fit of over 20000 photoproduction data of the reactions  $\gamma p \rightarrow \pi^0 p$  and  $\gamma p \rightarrow \pi^+ n$ , for altogether seven observables:  $d\sigma/d\Omega$ ,  $\Sigma$ ,  $T$ ,  $P$ ,  $\Delta\sigma_{31}$ ,  $G$ , and  $H$ . The polarization observables  $E$ ,  $F$ ,  $C_{x'_L}$ , and  $C_{z'_L}$  are predicted. Minimal chiral constraints and the incorporation of some isospin breaking effects allow for a precise description of the data even very close to threshold.

In order to shed light on the impact of recent high-precision measurements by ELSA, JLab, MAMI, Spring-8 and GRAAL, we have performed another fit where we omitted those recent data and included only data on  $d\sigma/d\Omega$ ,  $\Sigma$ ,  $T$ , and  $P$ . The predictions of  $\Delta\sigma_{31}$ ,  $G$ , and  $H$  based on such a fit turned out to be surprisingly good. However, the explicit inclusion of actual data on those observables definitely has a significant quantitative influence on the values of the resulting resonance photocouplings.

The resonance positions and residues were determined in the hadronic Jülich2012 analysis. The photocouplings extracted in the present study are found to be in qualitative agreement with other determinations in most cases. Since, in general, the phase angle is not small, the traditionally quoted, real helicity couplings cannot be identified with the photocouplings at the pole.

To complete the analysis, a comprehensive error estimate of extracted multipoles and photocouplings is planned. The extension of the present approach to other photoproduction channels is straightforward.

We would like to thank Reinhard Beck, Michael Dugger, César Fernández Ramírez, Manuela Gottschall, Jan Hartmann, Eberhard Klempt, Vincent Mathieu, Paolo Pedroni, Andrei Sarantsev, Toru Sato, Mark Sikora, Igor Strakovsky, Steffen Strauch, Adam Szczepaniak, Annika Thiel, Ulrike Thoma, Lothar Tiaator, Daniel Watts, and Ron Workman for many discussions and providing data. The numerical calculations were made possible through the grant jikp07 at the JUROPA supercomputer of the Forschungszentrum Jülich. This work is also supported by the EU Integrated Infrastructure Initiative HadronPhysics3 (contract number 283286) and by the DFG (Deutsche Forschungsgemeinschaft, GZ: DO 1302/1-2 and SFB/TR 16, “Subnuclear Structure of Matter”). The work of F.H. has been partially supported by the FFE Grant No. 41788390 (COSY-058) and by the One Hundred Person Project of the University of Chinese Academy of Sciences.

**Table 2.** Properties of the  $I = 1/2$  resonances: Pole positions  $E_p$  ( $\Gamma_{\text{tot}}$  defined as  $-2\text{Im} E_p$ ), photocouplings at the pole ( $A_{\text{pole}}^h, \vartheta^h$ ) according to eq. (22).

fit→	Re $E_p$	$-2\text{Im} E_p$	$A_{\text{pole}}^{1/2}$		$\vartheta^{1/2}$		$A_{\text{pole}}^{3/2}$		$\vartheta^{3/2}$	
	[MeV]	[MeV]	[ $10^{-3}\text{ GeV}^{-1/2}$ ]		[deg]		[ $10^{-3}\text{ GeV}^{-1/2}$ ]		[deg]	
			1	2	1	2	1	2	1	2
<b><math>N(1535) 1/2^-</math></b>	<b>1498</b>	<b>74</b>	57	<b><math>50_{-4}^{+4}</math></b>	-51	<b><math>-45_{-10}^{+12}</math></b>				
BnGa [55]	1501±4	134±11		116±10		7±6				
ANL-Osaka [68]	1482	196		161		9				
SAID [246]	1502	95		77±5		4				
<b><math>N(1650) 1/2^-</math></b>	<b>1677</b>	<b>146</b>	27	<b><math>23_{-8}^{+3}</math></b>	-14	<b><math>-29_{-15}^{+28}</math></b>				
BnGa [55]	1647±6	103±8		33±7		-9±15				
ANL-Osaka [68]	1656	170		40		-44				
SAID [246]	1648	80		35±3		-16				
<b><math>N(1440) 1/2^{+(b)}</math></b>	<b>1353</b>	<b>212</b>	-58	<b><math>-54_{-3}^{+4}</math></b>	-44	<b><math>-43_{-5}^{+2}</math></b>				
BnGa [55]	1370±4	190±7		-44±7		-38±5				
ANL-Osaka [68]	1374	152		49		-10				
SAID [246]	1359	162		-66±5		-38				
<b><math>N(1710) 1/2^+</math></b>	<b>1637</b>	<b>97</b>	15	<b><math>28_{-2}^{+9}</math></b>	13	<b><math>77_{-6}^{+20}</math></b>				
BnGa [55]	1687±17	200±25		55±18		-10±65				
ANL-Osaka [68]	1746	354		86		106				
<b><math>N(1750) 1/2^{+(a,b)}</math></b>	<b>1742</b>	<b>318</b>	-2	<b><math>-10_{-6}^{+3}</math></b>	8	<b><math>32_{+12}^{-13}</math></b>				
<b><math>N(1720) 3/2^+</math></b>	<b>1717</b>	<b>208</b>	39	<b><math>51_{-4}^{+5}</math></b>	31	<b><math>-8_{-4}^{+9}</math></b>	17	<b><math>14_{-3}^{+9}</math></b>	118	<b><math>37_{-59}^{+29}</math></b>
BnGa [55]	1660±30	450±100		110±45		0±40		150±35		65±35
ANL-Osaka [68]	1703	140		234		2		70		173
<b><math>N(1520) 3/2^-</math></b>	<b>1519</b>	<b>110</b>	-27	<b><math>-24_{-3}^{+8}</math></b>	-18	<b><math>-24_{-6}^{+16}</math></b>	114	<b><math>117_{-10}^{+6}</math></b>	19	<b><math>19_{-2}^{+2}</math></b>
BnGa [55]	1507±3	111±5		-21±4		0±5		132±9		2±4
ANL-Osaka [68]	1501	78		38		2		94		-173
SAID [246]	1515	113		-24±3		-7		157±6		10
<b><math>N(1675) 5/2^-</math></b>	<b>1650</b>	<b>126</b>	22	<b><math>22_{-7}^{+4}</math></b>	24	<b><math>38_{-2}^{+5}</math></b>	21	<b><math>36_{-5}^{+4}</math></b>	-71	<b><math>-41_{-4}^{+4}</math></b>
BnGa [55]	1654±4	151±5		24±3		-16±5		26±8		-19±6
ANL-Osaka [68]	1650	150		5		-22		33		-23
<b><math>N(1680) 5/2^+</math></b>	<b>1666</b>	<b>108</b>	-12	<b><math>-13_{-5}^{+2}</math></b>	-46	<b><math>-60_{-18}^{+9}</math></b>	124	<b><math>126_{-2}^{+1}</math></b>	-26	<b><math>-24_{-2}^{+3}</math></b>
BnGa [55]	1676±6	113±4		-13±4		-25±22		134±5		-2±4
ANL-Osaka [68]	1665	98		53		-5		38		-177
<b><math>N(1990) 7/2^+</math></b>	<b>1788</b>	<b>282</b>	19	<b><math>10_{-6}^{+11}</math></b>	-76	<b><math>-173_{-155}^{+108}</math></b>	37	<b><math>53_{-28}^{+23}</math></b>	97	<b><math>-34_{-4}^{+17}</math></b>
BnGa [55]	2030±65	240±60		42±14		-30±20		58±12		-35±25
<b><math>N(2190) 7/2^-</math></b>	<b>2092</b>	<b>363</b>	-48	<b><math>-83_{-3}^{+7}</math></b>	-16	<b><math>-28_{-2}^{+6}</math></b>	70	<b><math>95_{-10}^{+13}</math></b>	-19	<b><math>-21_{-5}^{+3}</math></b>
BnGa [55]	2150±25	330±30		-63±7		10±15		35±20		25±10
<b><math>N(2250) 9/2^-</math></b>	<b>2141</b>	<b>465</b>	-56	<b><math>-90_{-22}^{+25}</math></b>	-91	<b><math>-99_{+17}^{-11}</math></b>	14	<b><math>49_{-19}^{+31}</math></b>	-89	<b><math>121_{-43}^{+36}</math></b>
BnGa [55]	2195±45	470±50		< 10		-		< 10		-
<b><math>N(2220) 9/2^+</math></b>	<b>2196</b>	<b>662</b>	-108	<b><math>-233_{-44}^{+84}</math></b>	-93	<b><math>-91_{-6}^{+10}</math></b>	87	<b><math>162_{-38}^{+41}</math></b>	-76	<b><math>-71_{-13}^{+26}</math></b>
BnGa [55]	2150±35	440±40		< 10		-		< 10		-

(a) Not identified with PDG name.

(b) Dynamically generated.

**Table 3.** Properties of the  $I = 3/2$  resonances: Pole positions  $E_p$  ( $\Gamma_{\text{tot}}$  defined as  $-2\text{Im } E_p$ ), photocouplings at the pole ( $A_{\text{pole}}^h, \vartheta^h$ ) according to eq. (22).

fit→	Re $E_p$	$-2\text{Im } E_p$	$A_{\text{pole}}^{1/2}$		$\vartheta^{1/2}$		$A_{\text{pole}}^{3/2}$		$\vartheta^{3/2}$	
	[MeV]	[MeV]	[ $10^{-3} \text{ GeV}^{-1/2}$ ]		[deg]		[ $10^{-3} \text{ GeV}^{-1/2}$ ]		[deg]	
			1	2	1	2	1	2	1	2
<b><math>\Delta(1620) 1/2^-</math></b>	<b>1599</b>	<b>71</b>	-28	$-28_{-2}^{+6}$	85	$92_{-4}^{+1}$				
BnGa [55]	$1597 \pm 4$	$130 \pm 9$		$52 \pm 5$		$-9 \pm 9$				
ANL-Osaka [68]	1592	136		113		-1				
<b><math>\Delta(1910) 1/2^+</math></b>	<b>1788</b>	<b>575</b>	-200	$-246_{-47}^{+24}$	-87	$47_{-4}^{+9}$				
BnGa [55]	$1850 \pm 40$	$350 \pm 45$		$23 \pm 9$		$40 \pm 90$				
ANL-Osaka [68]	1854	368		52		170				
<b><math>\Delta(1232) 3/2^+</math></b>	<b>1220</b>	<b>86</b>	-116	$-114_{-3}^{+10}$	-27	$-27_{-2}^{+4}$	-231	$-229_{-4}^{+3}$	-15	$-15_{-0.4}^{+0.3}$
BnGa [55]	$1210 \pm 1$	$99 \pm 2$		$-131 \pm 3.5$		$-19 \pm 2$		$-254 \pm 4.5$		$-9 \pm 1$
ANL-Osaka [68]	1211	102		-133		-15		-257		-3
SAID [246]	1211	99		$-136 \pm 5$		-18		$-255 \pm 5$		-6
<b><math>\Delta(1600) 3/2^+ \text{ (a)}</math></b>	<b>1553</b>	<b>352</b>	260	$193_{-24}^{+23}$	27	$15_{-15}^{+9}$	-72	$-254_{-86}^{+85}$	-54	$-25_{-6}^{+10}$
BnGa [55]	$1498 \pm 25$	$230 \pm 50$		$53 \pm 10$		$130 \pm 25$		$41 \pm 11$		$165 \pm 17$
ANL-Osaka [68]	1734	352		72		-109		136		-98
<b><math>\Delta(1920) 3/2^+</math></b>	<b>1724</b>	<b>863</b>	46	$190_{-22}^{+50}$	8	$-137_{-11}^{+24}$	-352	$-398_{-67}^{+70}$	-85	$-87_{-5}^{+4}$
BnGa [55]	$1890 \pm 30$	$300 \pm 60$		$130_{-60}^{+30}$		$-65 \pm 20$		$115_{-50}^{+25}$		$-160 \pm 20$
<b><math>\Delta(1700) 3/2^-</math></b>	<b>1675</b>	<b>303</b>	106	$109_{-10}^{+10}$	10	$-12_{-6}^{+12}$	141	$111_{-6}^{+27}$	27	$21_{-11}^{+9}$
BnGa [55]	$1680 \pm 10$	$305 \pm 15$		$170 \pm 20$		$50 \pm 15$		$170 \pm 25$		$45 \pm 10$
ANL-Osaka [68]	1707	340		59		-70		125		-75
<b><math>\Delta(1930) 5/2^-</math></b>	<b>1775</b>	<b>646</b>	84	$130_{-96}^{+73}$	-55	$-177_{-26}^{+77}$	-231	$-56_{-151}^{+3}$	82	$42_{-76}^{+72}$
ANL-Osaka [68]	1936	210		53		-21		35		-15
<b><math>\Delta(1905) 5/2^+</math></b>	<b>1770</b>	<b>259</b>	61	$13_{-5}^{+13}$	-92	$19_{-36}^{+72}$	112	$72_{-16}^{+16}$	85	$67_{-7}^{+13}$
BnGa [55]	$1805 \pm 10$	$300 \pm 15$		$25 \pm 5$		$-23 \pm 15$		$-50 \pm 4$		$0 \pm 10$
ANL-Osaka [68]	1765	188		8		-97		18		-90
<b><math>\Delta(1950) 7/2^+</math></b>	<b>1884</b>	<b>234</b>	-68	$-71_{-4}^{+4}$	-18	$-29_{-4}^{+2}$	-85	$-89_{-7}^{+8}$	-16	$-25_{-1}^{+3}$
BnGa [55]	$1890 \pm 4$	$243 \pm 8$		$-72 \pm 4$		$-7 \pm 5$		$-96 \pm 5$		$-7 \pm 5$
ANL-Osaka [68]	1872	206		-62		-9		-76		2
<b><math>\Delta(2200) 7/2^-</math></b>	<b>2147</b>	<b>477</b>	41	$107_{-20}^{+11}$	-105	$-72_{-5}^{+5}$	-29	$-131_{-9}^{+24}$	71	$78_{-5}^{+9}$
<b><math>\Delta(2400) 9/2^-</math></b>	<b>1969</b>	<b>577</b>	-59	$-128_{-12}^{+46}$	39	$63_{-3}^{+24}$	-15	$-115_{-24}^{+42}$	27	$84_{-28}^{+17}$

(a) Dynamically generated.

## Appendix A. Multipole decomposition

We start by writing the reaction amplitude for the (pseudoscalar) meson photoproduction process,

$$\gamma(k) + N(p) \rightarrow M(q) + N(p'), \quad (\text{A.1})$$

where the arguments  $k$ ,  $p$ ,  $q$ , and  $p'$  stand for the four-momenta of the incident photon, target nucleon, emitted meson, and recoil nucleon, respectively. Following refs. [249, 250], the photoproduction amplitude of pseudoscalar mesons is written as

$$\begin{aligned} J = & iJ_1 \vec{\sigma} \cdot \vec{\epsilon} + J_2 \vec{\sigma} \cdot \hat{q} \vec{\sigma} \cdot (\hat{k} \times \vec{\epsilon}) \\ & + iJ_3 \vec{\sigma} \cdot \hat{k} \hat{q} \cdot \vec{\epsilon} + iJ_4 \vec{\sigma} \cdot \hat{q} \hat{q} \cdot \vec{\epsilon}, \end{aligned} \quad (\text{A.2})$$

where  $\vec{q}$  and  $\vec{k}$  denote the meson and photon momentum, respectively; the photon polarization vector is denoted by  $\vec{\epsilon}$ . For an arbitrary vector  $\vec{a}$ , the notation  $\hat{a}$  stands for the corresponding unit vector. The  $J_i$  ( $i = 1-4$ ) are functions of the total energy  $E$  and the scattering angle  $x \equiv \cos \theta = \hat{q} \cdot \hat{k}$ .

For further convenience, we rewrite eq. (A.2) as [251]

$$\begin{aligned} \hat{\mathcal{M}} = & -iJ = F_1 \vec{\sigma} \cdot \vec{\epsilon} + iF_2 (\hat{k} \times \hat{q}) \cdot \vec{\epsilon} \\ & + F_3 \vec{\sigma} \cdot \hat{k} \hat{q} \cdot \vec{\epsilon} + F_4 \vec{\sigma} \cdot \hat{q} \hat{q} \cdot \vec{\epsilon}, \end{aligned} \quad (\text{A.3})$$

where

$$F_1 \equiv J_1 - xJ_2, \quad F_2 \equiv J_2, \quad F_3 \equiv J_2 + J_3, \quad F_4 \equiv J_4. \quad (\text{A.4})$$

Note that the forms of the amplitudes given by eqs. (A.2), (A.3) are coordinate-independent.

The multipole decomposition of the photoproduction amplitude  $J$  in eq. (A.2) is given by [249, 250]

$$\begin{pmatrix} J_1 \\ J_2 \\ J_3 \\ J_4 \end{pmatrix} = \frac{4\pi E}{m_N} \sum_{L=0}^{\infty} \tilde{D}_L(x) \begin{pmatrix} E_{L+} \\ E_{L-} \\ M_{L+} \\ M_{L-} \end{pmatrix}, \quad (\text{A.5})$$

where  $L$  stands for the orbital angular momentum of the final nucleon-pion state. The electric and magnetic multipoles  $E_{L\pm}$  and  $M_{L\pm}$  correspond to our photoproduction amplitude  $M$  in eq. (8) for a given partial wave with  $J = L \pm \frac{1}{2}$ . The matrix  $\tilde{D}_L(x)$  is given by [249]

$$\tilde{D}_L \equiv \begin{pmatrix} P'_{L+1} & P'_{L-1} & LP'_{L+1} & (L+1)P'_{L-1} \\ 0 & 0 & (L+1)P'_L & LP'_L \\ P''_{L+1} & P''_{L-1} & -P''_{L+1} & P''_{L-1} \\ -P''_L & -P''_L & P''_L & -P''_L \end{pmatrix},$$

with  $P'_L \equiv P'_L(x)$  and  $P''_L \equiv P''_L(x)$  denoting, respectively, the derivative and the double-derivative of the Legendre Polynomial of the first kind,  $P_L \equiv P_L(x)$ , with respect to  $x$ .

Considering partial waves with  $J^P \leq 9/2$  corresponding to orbital angular momentum  $L \leq 5$  (remember that

this excludes  $E_{5+}$  and  $M_{5+}$ ), one obtains from eqs. (A.4) and (A.5)

$$\begin{aligned} F_1 = & -i \frac{4\pi E}{m_N} \frac{1}{128} \left[ 32(4E_{0+} + 9E_{2+} + 4M_{2-} + 9M_{4-}) \right. \\ & + 2 \cos(\theta)(192E_{1+} + 360E_{3+} + 525E_{5+} - 64M_{1-} \\ & + 64M_{1+} + 168M_{3-} + 24M_{3+} + 345M_{5-} + 15M_{5+}) \\ & + 8 \cos(2\theta)(60E_{2+} + 105E_{4+} - 48M_{2-} + 48M_{2+} \\ & + 40M_{4-} + 20M_{4+}) + 5 \cos(3\theta)(112E_{3+} + 189E_{5+} \\ & - 144M_{3-} + 144M_{3+} + 49M_{5-} + 63M_{5+}) \\ & + 70 \cos(4\theta)(9E_{4+} + 16(M_{4+} - M_{4-})) \\ & \left. + 450E_{4+} + 63 \cos(5\theta)(11E_{5+} + 25(M_{5+} - M_{5-})) \right], \\ F_2 = & -i \frac{4\pi E}{m_N} \frac{1}{64} \left[ 64M_{1-} + 128M_{1+} \right. \\ & + 24 \cos(\theta)(16M_{2-} + 24M_{2+} + 60M_{4-} + 75M_{4+}) \\ & + 60 \cos(2\theta)(12M_{3-} + 16M_{3+} + 35M_{5-} + 42M_{5+}) \\ & + 9(48M_{3-} + 64M_{3+} + 125M_{5-} + 150M_{5+}) \\ & + 280 \cos(3\theta)(4M_{4-} + 5M_{4+}) \\ & \left. + 315 \cos(4\theta)(5M_{5-} + 6M_{5+}) \right], \\ F_3 = & -i \frac{4\pi E}{m_N} \frac{1}{64} \left[ 192E_{1+} + 24 \cos(\theta)(40E_{2+} + 175E_{4+} \right. \\ & + 4(4M_{2-} - 4M_{2+} + 35M_{4-} - 25M_{4+})) \\ & + 60 \cos(2\theta)(28E_{3+} + 105E_{5+} + 12M_{3-} - 12M_{3+} \\ & + 91M_{5-} - 63M_{5+}) + 1200E_{3+} \\ & + 280 \cos(3\theta)(9E_{4+} + 4M_{4-} - 4M_{4+}) \\ & + 315 \cos(4\theta)(11E_{5+} + 5M_{5-} - 5M_{5+}) \\ & + 3675E_{5+} + 64M_{1-} - 64M_{1+} + 816M_{3-} \\ & \left. - 624M_{3+} + 3525M_{5-} - 2325M_{5+} \right], \\ F_4 = & -i \frac{4\pi E}{m_N} \frac{3}{8} \left[ -2(4E_{2+} + 25E_{4+} + 8M_{2-} - 4M_{2+} \right. \\ & + 50M_{4-} - 25M_{4+}) - 5 \cos(\theta)(8E_{3+} + 35E_{5+} \\ & + 16M_{3-} - 8M_{3+} + 70M_{5-} - 35M_{5+}) \\ & - 70 \cos(2\theta)(E_{4+} + 2M_{4-} - M_{4+}) \\ & \left. - 105 \cos(3\theta)(E_{5+} + 2M_{5-} - M_{5+}) \right]. \end{aligned} \quad (\text{A.6})$$

## Appendix B. Observables

In order to explain our conventions, we explicitly define the spin-polarization observables first in a coordinate-independent manner. We then provide expressions for the

specific coordinate systems relevant for their actual measurements. We will also give some details how these observables are calculated in the present work in terms of the multiple amplitudes introduced in sect. 2.2.

### Appendix B.1. Definitions of the observables

In the following, we introduce a set of coordinate-independent unit vectors

$$\hat{n}_3 = \hat{k}, \quad \hat{n}_2 = \frac{\hat{k} \times \hat{q}}{|\hat{k} \times \hat{q}|}, \quad \hat{n}_1 = \hat{n}_2 \times \hat{n}_3. \quad (\text{B.1})$$

Note that in terms of  $\{\hat{n}_1, \hat{n}_2, \hat{n}_3\}$ , the center-of-momentum (c.m.) Cartesian coordinate system  $\{\hat{x}, \hat{y}, \hat{z}\}$ , where  $\vec{k} + \vec{p} = \vec{q} + \vec{p}' = 0$ , and the laboratory (lab) Cartesian coordinate system  $\{\hat{x}_L, \hat{y}_L, \hat{z}_L\}$ , where  $\vec{p} = 0$ , are given by

$$\begin{aligned} \{\hat{x}, \hat{y}, \hat{z}\} &= \{\hat{n}_1, \hat{n}_2, \hat{n}_3\}_{(\text{cm})}, \\ \{\hat{x}_L, \hat{y}_L, \hat{z}_L\} &= \{\hat{n}_1, \hat{n}_2, \hat{n}_3\}_{(\text{lab})}, \end{aligned} \quad (\text{B.2})$$

where the subscript (cm) and (lab) indicate that  $\{\hat{n}_1, \hat{n}_2, \hat{n}_3\}$  is to be evaluated in the c.m. and lab frame, respectively.

The reaction plane is defined as the  $(\hat{n}_1 \hat{n}_3)$ -plane. Then,  $\hat{n}_2$  is perpendicular to the reaction plane.

A real photon has two independent polarization states. A linearly polarized photon is specified by  $\vec{\epsilon}_{\parallel}$  and  $\vec{\epsilon}_{\perp}$ , where  $\vec{\epsilon}_{\parallel}$  ( $\vec{\epsilon}_{\perp}$ ) stands for the photon polarization vector parallel (perpendicular) to the reaction plane. More generally, we define the linearly polarized photon states  $\vec{\epsilon}_{\parallel'}$  and  $\vec{\epsilon}_{\perp'}$  obtained by rotating  $\vec{\epsilon}_{\parallel}$  and  $\vec{\epsilon}_{\perp}$  (counterclockwise) by an angle  $\phi$  about the  $\hat{n}_3$ -axis, *i.e.*,

$$\begin{aligned} \vec{\epsilon}_{\parallel'} &= \cos \phi \vec{\epsilon}_{\parallel} + \sin \phi \vec{\epsilon}_{\perp}, \\ \vec{\epsilon}_{\perp'} &= -\sin \phi \vec{\epsilon}_{\parallel} + \cos \phi \vec{\epsilon}_{\perp}. \end{aligned} \quad (\text{B.3})$$

The circularly polarized photon is specified by

$$\vec{\epsilon}_{\pm} \equiv \mp \frac{1}{\sqrt{2}} (\vec{\epsilon}_{\parallel} \pm i \vec{\epsilon}_{\perp}). \quad (\text{B.4})$$

For further convenience, we also introduce the projection operator  $\hat{P}_{\lambda}$  which specifies the state of the photon polarization; namely,  $\hat{P}_{\lambda} \vec{\epsilon} \equiv \vec{\epsilon}_{\lambda}$ . Note that  $\hat{P}_{\lambda} \hat{P}_{\lambda} = \delta_{\lambda, \lambda}$  and  $\sum_{\lambda} \hat{P}_{\lambda} = 1$ . The projection operator  $\hat{P}_{\lambda}$  defined here is associated with the Stokes vector  $\vec{P}^S$  [252], which specifies the direction and degree of polarization of the photon. For example,  $\hat{P}_{\pm}$  corresponds to  $P_{z=n_3}^S = \pm 1$ , while  $\hat{P}_{\perp}$  ( $\hat{P}_{\parallel}$ ) corresponds to  $P_{x=n_1}^S = +1$  ( $P_{x=n_1}^S = -1$ ). Furthermore, the difference of the appropriate projection operators can be expressed in terms of the usual Pauli spin matrices in photon helicity space, *i.e.*,  $\hat{P}_{+} - \hat{P}_{-} = \sigma_{n_3}$  and  $\hat{P}_{\perp} - \hat{P}_{\parallel} = \sigma_{n_1}$ .

We now define the coordinate-independent observables. Provided the reaction amplitude  $\hat{\mathcal{M}}$  in eq. (A.3)

is Lorentz invariant, these observables are also Lorentz invariants. The cross section is defined as

$$\frac{d\sigma}{d\Omega} \equiv \frac{1}{4} \text{Tr}[\hat{\mathcal{M}} \hat{\mathcal{M}}^{\dagger}], \quad (\text{B.5})$$

where the trace is over both the nucleon spin and photon polarization. The appearance of the factor  $\frac{1}{4}$  is due to the averaging over the target-nucleon spin and the photon-beam polarization.

The single polarization observables, namely, the beam, target, and recoil polarization asymmetries,  $\Sigma$ ,  $T$ , and  $P$ , respectively, are defined as

$$\begin{aligned} \frac{d\sigma}{d\Omega} \Sigma &\equiv \frac{1}{4} \text{Tr}[\hat{\mathcal{M}}(\hat{P}_{\perp} - \hat{P}_{\parallel}) \hat{\mathcal{M}}^{\dagger}], \\ \frac{d\sigma}{d\Omega} T &\equiv \frac{1}{4} \text{Tr}[\hat{\mathcal{M}} \sigma_{n_2} \hat{\mathcal{M}}^{\dagger}], \\ \frac{d\sigma}{d\Omega} P &\equiv \frac{1}{4} \text{Tr}[\hat{\mathcal{M}} \hat{\mathcal{M}}^{\dagger} \sigma_{n_2}]. \end{aligned} \quad (\text{B.6})$$

The beam-target asymmetries,  $E$ ,  $F$ ,  $G$ , and  $H$ , are defined as

$$\begin{aligned} \frac{d\sigma}{d\Omega} E &\equiv -\frac{1}{4} \text{Tr}[\hat{\mathcal{M}}(\hat{P}_{+} - \hat{P}_{-}) \sigma_{n_3} \hat{\mathcal{M}}^{\dagger}] \\ &= -2 \frac{1}{4} \text{Tr}[\hat{\mathcal{M}} \hat{P}_{+} \sigma_{n_3} \hat{\mathcal{M}}^{\dagger}] = 2 \frac{1}{4} \text{Tr}[\hat{\mathcal{M}} \hat{P}_{-} \sigma_{n_3} \hat{\mathcal{M}}^{\dagger}], \\ \frac{d\sigma}{d\Omega} F &\equiv \frac{1}{4} \text{Tr}[\hat{\mathcal{M}}(\hat{P}_{+} - \hat{P}_{-}) \sigma_{n_1} \hat{\mathcal{M}}^{\dagger}] \\ &= 2 \frac{1}{4} \text{Tr}[\hat{\mathcal{M}} \hat{P}_{+} \sigma_{n_1} \hat{\mathcal{M}}^{\dagger}] = -2 \frac{1}{4} \text{Tr}[\hat{\mathcal{M}} \hat{P}_{-} \sigma_{n_1} \hat{\mathcal{M}}^{\dagger}], \\ \frac{d\sigma}{d\Omega} G &\equiv -\frac{1}{4} \text{Tr}[\hat{\mathcal{M}}(\hat{P}_{\perp'} - \hat{P}_{\parallel'}) \sigma_{n_3} \hat{\mathcal{M}}^{\dagger}] \\ &= -2 \frac{1}{4} \text{Tr}[\hat{\mathcal{M}} \hat{P}_{\perp'} \sigma_{n_3} \hat{\mathcal{M}}^{\dagger}] = 2 \frac{1}{4} \text{Tr}[\hat{\mathcal{M}} \hat{P}_{\parallel'} \sigma_{n_3} \hat{\mathcal{M}}^{\dagger}], \\ \frac{d\sigma}{d\Omega} H &\equiv \frac{1}{4} \text{Tr}[\hat{\mathcal{M}}(\hat{P}_{\perp'} - \hat{P}_{\parallel'}) \sigma_{n_1} \hat{\mathcal{M}}^{\dagger}] \\ &= 2 \frac{1}{4} \text{Tr}[\hat{\mathcal{M}} \hat{P}_{\perp'} \sigma_{n_1} \hat{\mathcal{M}}^{\dagger}] = -2 \frac{1}{4} \text{Tr}[\hat{\mathcal{M}} \hat{P}_{\parallel'} \sigma_{n_1} \hat{\mathcal{M}}^{\dagger}]. \end{aligned} \quad (\text{B.7})$$

Here, in the definitions of  $G$  and  $H$ , the projection operators  $\hat{P}_{\parallel'}$  and  $\hat{P}_{\perp'}$  correspond to the photon polarizations given by eq. (B.3) with  $\phi = \pi/4$ . We note that in the above definition of  $E$  and  $G$ , we have introduced a minus sign so that our convention matches that of the SAID group [104] in the c.m. frame.

The beam-recoil asymmetries,  $C_{n'_i}$  and  $O_{n'_i}$  ( $i = 1, 3$ ), are defined as

$$\begin{aligned} \frac{d\sigma}{d\Omega} C_{n'_i} &\equiv -\frac{1}{4} \text{Tr}[\hat{\mathcal{M}}(\hat{P}_{+} - \hat{P}_{-}) \hat{\mathcal{M}}^{\dagger} \sigma_{n'_i}] \\ &= -2 \frac{1}{4} \text{Tr}[\hat{\mathcal{M}} \hat{P}_{+} \hat{\mathcal{M}}^{\dagger} \sigma_{n'_i}] = 2 \frac{1}{4} \text{Tr}[\hat{\mathcal{M}} \hat{P}_{-} \hat{\mathcal{M}}^{\dagger} \sigma_{n'_i}], \\ \frac{d\sigma}{d\Omega} O_{n'_i} &\equiv -\frac{1}{4} \text{Tr}[\hat{\mathcal{M}}(\hat{P}_{\perp'} - \hat{P}_{\parallel'}) \hat{\mathcal{M}}^{\dagger} \sigma_{n'_i}] \\ &= -2 \frac{1}{4} \text{Tr}[\hat{\mathcal{M}} \hat{P}_{\perp'} \hat{\mathcal{M}}^{\dagger} \sigma_{n'_i}] = 2 \frac{1}{4} \text{Tr}[\hat{\mathcal{M}} \hat{P}_{\parallel'} \hat{\mathcal{M}}^{\dagger} \sigma_{n'_i}], \end{aligned} \quad (\text{B.8})$$

associated with  $\{\hat{n}'_1, \hat{n}'_2, \hat{n}'_3\}$  which is obtained by rotating  $\{\hat{n}_1, \hat{n}_2, \hat{n}_3\}$  (counterclockwise) by an angle  $\theta$  about the  $\hat{n}_2$ -axis ( $\cos \theta \equiv \hat{q} \cdot \hat{n}_3$ ), such that,  $\hat{n}'_3$  is in the direction of the emitted meson momentum  $\vec{q}$ , *i.e.*,  $\hat{n}'_3 = \hat{q}$ . Explicitly, they are related by

$$\begin{aligned}\hat{n}'_1 &= \cos \theta \hat{n}_1 - \sin \theta \hat{n}_3, \\ \hat{n}'_3 &= \sin \theta \hat{n}_1 + \cos \theta \hat{n}_3, \\ \hat{n}'_2 &= \hat{n}_2.\end{aligned}\quad (\text{B.9})$$

The target-recoil asymmetries,  $L_{n'_i}$  and  $T_{n'_i}$  ( $i = 1, 3$ ), are defined as

$$\begin{aligned}\frac{d\sigma}{d\Omega} L_{n'_i} &\equiv \zeta_i \frac{1}{4} \text{Tr}[\hat{\mathcal{M}}\sigma_{n_3}\hat{\mathcal{M}}^\dagger\sigma_{n'_i}], \\ \frac{d\sigma}{d\Omega} T_{n'_i} &\equiv \frac{1}{4} \text{Tr}[\hat{\mathcal{M}}\sigma_{n_1}\hat{\mathcal{M}}^\dagger\sigma_{n'_i}],\end{aligned}\quad (\text{B.10})$$

where  $\zeta_1 = -1$  and  $\zeta_3 = +1$ . Again, these sign factors have been introduced to match the SAID convention in the c.m. frame. A list of conventions used by different groups may be found in ref. [253].

## Appendix B.2. Observables in terms of the coefficient amplitudes $F_i$

Any of the observables defined in the previous subsection may be expressed in terms of the coefficients  $F_i$  in eq. (A.3). The photoproduction amplitude given by eq. (A.3) can be put straightforwardly into the form

$$\hat{\mathcal{M}}^\lambda = \sum_{m=0}^3 \mathcal{M}_m^\lambda \sigma_m, \quad (\text{B.11})$$

for a given state of photon polarization  $\vec{\epsilon}_\lambda$ . Here,  $\sigma_0 \equiv 1$  ( $\sigma_i$  ( $i = 1, 2, 3$ ), the usual Pauli spin-matrices). Note that the form given by the above equation is particularly suited for calculating the observables defined in the previous subsection. Then, following ref. [251], the differential cross section becomes

$$\begin{aligned}\frac{d\sigma}{d\Omega} &= |F_1|^2 + \frac{1}{2} \left( |F_2|^2 + |F_3|^2 + |F_4|^2 \right) \\ &\quad + 2 \text{Re}[(F_1 + F_3 \cos \theta) F_4^*] \sin^2 \theta.\end{aligned}\quad (\text{B.12})$$

In the cross section above, the incident flux and the (final-state) phase-space density factors have been left out for further convenience. Therefore, to get the physical cross section,  $\frac{d\sigma_o}{d\Omega}$ , one needs to multiply the above defined cross section by these factors, *i.e.*,

$$\frac{d\sigma_o}{d\Omega} \equiv \left( \frac{m_N}{4\pi E} \right)^2 \frac{|\vec{q}|}{|\vec{k}|} \frac{d\sigma}{d\Omega}, \quad (\text{B.13})$$

in the c.m. frame.

The single polarization observables become

$$\begin{aligned}\frac{d\sigma}{d\Omega} \Sigma &= \frac{1}{2} \left( |F_2|^2 - |F_3|^2 - |F_4|^2 \right. \\ &\quad \left. - 2 \text{Re}[(F_1 + F_3 \cos \theta) F_4^*] \right) \sin^2 \theta, \\ \frac{d\sigma}{d\Omega} T &= \text{Im} \left[ (-F_2 + F_3 + F_4 \cos \theta) F_1^* \right. \\ &\quad \left. + (F_3 + F_4 \cos \theta) F_4^* \sin^2 \theta \right] \sin \theta, \\ \frac{d\sigma}{d\Omega} P &= -\text{Im} \left[ (F_2 + F_3 + F_4 \cos \theta) F_1^* \right. \\ &\quad \left. + (F_3 + F_4 \cos \theta) F_4^* \sin^2 \theta \right] \sin \theta,\end{aligned}\quad (\text{B.14})$$

and the double-polarization observables  $E$ ,  $F$ ,  $G$  and  $H$  read

$$\begin{aligned}\frac{d\sigma}{d\Omega} E &= |F_1|^2 + \text{Re} [F_2^*(F_3 + F_4 \cos \theta) + F_1^* F_4] \sin^2 \theta, \\ \frac{d\sigma}{d\Omega} F &= -\text{Re} [F_2^*(F_1 + F_4 \sin^2 \theta) - F_1^*(F_3 + F_4 \cos \theta)] \sin \theta \\ \frac{d\sigma}{d\Omega} G &= \text{Im} [F_2^*(F_3 + F_4 \cos \theta) + F_1^* F_4] \sin^2 \theta, \\ \frac{d\sigma}{d\Omega} H &= -\text{Im} [F_2^*(F_1 + F_4 \sin^2 \theta) \\ &\quad - F_1^*(F_3 + F_4 \cos \theta) \sin \theta] \sin \theta.\end{aligned}\quad (\text{B.15})$$

The beam-recoil polarizations  $C_{n'_1}$  and  $C_{n'_3}$  become

$$\begin{aligned}\frac{d\sigma}{d\Omega} C_{n'_1} &= \left\{ |F_1|^2 + \text{Re} \left[ F_1^*(F_2 + F_3) \cos \theta \right. \right. \\ &\quad \left. \left. + (F_1^* F_4 - F_2^* F_3 \sin^2 \theta) \right] \right\} \sin \theta, \\ \frac{d\sigma}{d\Omega} C_{n'_3} &= -|F_1|^2 \cos \theta + \text{Re} \left[ F_1^*(F_2 + F_3) \right. \\ &\quad \left. + F_2^*(F_3 \cos \theta + F_4) \right] \sin^2 \theta.\end{aligned}\quad (\text{B.16})$$

In the c.m. frame, where the Cartesian coordinate system  $\{\hat{x}', \hat{y}', \hat{z}'\}$  is identified with  $\{\hat{n}'_1, \hat{n}'_2, \hat{n}'_3\}_{(cm)}$ , we have

$$C_{x'} = C_{n'_1} \quad \text{and} \quad C_{z'} = C_{n'_3}. \quad (\text{B.17})$$

where  $C_{n'_1}$  and  $C_{n'_3}$  given by eq. (B.16) are evaluated in the c.m. frame.

Experimentalists report the beam-target asymmetries in the lab frame. Different groups use different lab coordinate frames. We define the lab frame quantities  $C_{x'_L}$  and  $C_{z'_L}$  with respect to the coordinate system  $\{\hat{x}'_L, \hat{y}'_L, \hat{z}'_L\}$  which is obtained by a (counterclockwise) rotation of  $\{\hat{x}_L, \hat{y}_L, \hat{z}_L\}$  (cf. eq. (B.2)) by an angle  $\pi - \theta_{p'_L}$  about the  $\hat{y}_L$ -axis. Here,  $\theta_{p'_L}$  stands for the recoil nucleon scattering angle in the  $\{\hat{x}_L, \hat{y}_L, \hat{z}_L\}$  frame, *i.e.*,  $\cos \theta_{p'_L} \equiv \hat{p}'_L \cdot \hat{z}_L$  with  $\hat{p}'_L$  being the recoil nucleon momentum in the latter frame. Explicitly,

$$\begin{aligned}\hat{x}'_L &= -\cos \theta_{p'_L} \hat{x}_L - \sin \theta_{p'_L} \hat{z}_L, \\ \hat{z}'_L &= \sin \theta_{p'_L} \hat{x}_L - \cos \theta_{p'_L} \hat{z}_L, \\ \hat{y}'_L &= \hat{y}_L.\end{aligned}\quad (\text{B.18})$$

Note that  $\hat{z}'_L$  points in the direction opposite to the recoil nucleon momentum, *i.e.*,  $\hat{z}'_L = -\hat{p}'_L$ .

The beam-recoil polarization observables in the lab frame,  $C_{x'_L}$  and  $C_{z'_L}$ , can be obtained from  $C_{x'}$  and  $C_{z'}$  in the c.m. frame by a combination of Lorentz boosts and rotations. We have [217, 254]

$$\begin{aligned} C_{x'_L} &= \cos \theta_r C_{x'} - \sin \theta_r C_{z'}, \\ C_{z'_L} &= \sin \theta_r C_{x'} + \cos \theta_r C_{z'}, \end{aligned} \quad (\text{B.19})$$

where the rotation angle  $\theta_r$  is given by

$$\begin{aligned} \cos \theta_r &= -\cos \theta \cos \theta_{p'_L} - \gamma_3 \sin \theta \sin \theta_{p'_L}, \\ \sin \theta_r &= \gamma_1 \left[ \cos \theta_{p'_L} \sin \theta + \gamma_3 \sin \theta_{p'_L} (\beta_1 \beta_3 - \cos \theta) \right], \end{aligned} \quad (\text{B.20})$$

with the Lorentz boost parameters

$$\beta_1 = \frac{|\vec{q}|}{\sqrt{\vec{q}^2 + m_N^2}}, \quad \beta_3 = \frac{|\vec{k}_L|}{\sqrt{\vec{k}_L^2 + m_N^2}}, \quad (\text{B.21})$$

and  $\gamma_i \equiv 1/\sqrt{1 - \beta_i^2}$ . Here,  $\vec{q}$  is the meson momentum in the c.m. frame  $\{\hat{x}, \hat{y}, \hat{z}\}$  and  $\vec{k}_L$  is the photon momentum in the lab frame  $\{\hat{x}_L, \hat{y}_L, \hat{z}_L\}$ .

We note that our choice of the lab frame,  $\{\hat{x}'_L, \hat{y}'_L, \hat{z}'_L\}$ , coincides with that of the SAID group [104] ( $\{\hat{x}^*, \hat{y}^*, \hat{z}^*\}$ ), and that,  $C_{x'_L} = C_{x^*}$  and  $C_{z'_L} = C_{z^*}$ .

In ref. [144], one introduces the cross-section difference of the parallel and anti-parallel helicity states of the photon and target nucleon. Explicitly,

$$\Delta\sigma_{31} = \frac{d\sigma_{3/2}}{d\Omega} - \frac{d\sigma_{1/2}}{d\Omega}, \quad (\text{B.22})$$

where  $\sigma_{3/2}$  and  $\sigma_{1/2}$  stand for the cross sections with the parallel ( $\lambda_N - \lambda_\gamma = \pm 3/2$ ) and the anti-parallel ( $\lambda_N - \lambda_\gamma = \pm 1/2$ ) initial state helicity, respectively.

$\Delta\sigma_{31}$  is related to the helicity asymmetry  $E$  via

$$\Delta\sigma_{31} = -2 \frac{d\sigma_o}{d\Omega} E, \quad (\text{B.23})$$

where the factor 1/2 is due to the fact that  $d\sigma_o/d\Omega$  (cf. eq. (B.13)) contains the initial spin averaging factor of 1/4, while  $d\sigma_{3/2}/d\Omega$  and  $d\sigma_{1/2}/d\Omega$  contain the spin averaging factor of 1/2.

## Appendix C. Definition of the photocouplings

Adopting the convention of ref. [246] the photocouplings are given as the residue of the helicity multipole  $A_{L\pm}^h$  multiplied by a complex factor  $\mathcal{N}$ :

$$\tilde{A}_{\text{pole}}^h = \mathcal{N} \text{Res} A_{L\pm}^h, \quad (\text{C.1})$$

where  $h = 1/2$  or  $3/2$  and

$$\mathcal{N} = I_F \sqrt{\frac{q_p}{k_p} \frac{2\pi(2J+1)E_p}{m_N r_{\pi N}}}. \quad (\text{C.2})$$

Here,  $I_F$  is an isospin factor with  $I_{1/2} = -\sqrt{3}$  and  $I_{3/2} = \sqrt{2/3}$ ,  $q_p$  ( $k_p$ ) is the meson (photon) momentum in the c.m. frame evaluated at the pole,  $J$  is the total angular momentum,  $L$  is the  $\pi N$  orbital angular momentum and  $m_N$  the nucleon mass, while  $E_p$  and  $r_{\pi N}$  represent the pole position and the elastic  $\pi N$  residue of the resonance. Note the convention that  $\text{Res} A_{L\pm}^h$  and  $r_{\pi N}$  are defined with a minus sign compared to the mathematical residues of the multipole and the elastic  $\pi N$  amplitude, respectively. The cuts of the square root in eq. (C.2) and also the square roots implicitly contained in  $q_p$ ,  $k_p$ , are from the origin to  $-\infty$ .

In terms of the electric and magnetic multipoles the helicity multipoles read

$$A_{L+}^{1/2} = -\frac{1}{2} [(L+2)E_{L+} + L M_{L+}], \quad (\text{C.3})$$

$$A_{L+}^{3/2} = \frac{1}{2} \sqrt{L(L+2)} [E_{L+} - M_{L+}], \quad (\text{C.4})$$

with total angular momentum  $J = L + 1/2$  and

$$A_{L-}^{1/2} = -\frac{1}{2} [(L-1)E_{L-} - (L+1)M_{L-}], \quad (\text{C.5})$$

$$A_{L-}^{3/2} = -\frac{1}{2} \sqrt{(L-1)(L+1)} [E_{L-} + M_{L-}], \quad (\text{C.6})$$

with  $J = L - 1/2$ .

The residues of the electric and magnetic multipoles  $E_{L\pm}$  and  $M_{L\pm}$  can be determined as explained in appendix C, eq. (C.2) of ref. [81].

## References

1. G. Höhler, *Pion Nucleon Scattering*, edited by H. Schopper, Landolt Börnstein, New Series, Group 9b, Vol. I (Springer, New York, 1983).
2. R.A. Arndt, W.J. Briscoe, I.I. Strakovsky, R.L. Workman, Phys. Rev. C **74**, 045205 (2006) arXiv: nucl-th/0605082.
3. R.L. Workman, M.W. Paris, W.J. Briscoe, I.I. Strakovsky, Phys. Rev. C **86**, 015202 (2012) arXiv:1202.0845 [hep-ph], webpage: <http://gwdac.phys.gwu.edu/>.
4. I.G. Aznauryan, V.D. Burkert, Phys. Rev. C **85**, 055202 (2012) arXiv:1201.5759 [hep-ph].
5. M. Ronniger, B.C. Metsch, Eur. Phys. J. A **47**, 162 (2011) arXiv:1111.3835 [hep-ph].
6. B. Golli, S. Širca, Eur. Phys. J. A **49**, 111 (2013) arXiv:1306.3330 [nucl-th].
7. G. Ramalho, M.T. Pena, Phys. Rev. D **84**, 033007 (2011) arXiv:1105.2223 [hep-ph].
8. S. Capstick, Phys. Rev. D **46**, 2864 (1992).
9. S. Capstick, W. Roberts, Phys. Rev. D **49**, 4570 (1994) arXiv:9310030[nucl-th].
10. C. Jayalath, J.L. Goity, E. González de Urreta, N.N. Scoccola, Phys. Rev. D **84**, 074012 (2011) arXiv:1108.2042 [nucl-th].
11. D.J. Wilson, I.C. Cloët, L. Chang, C.D. Roberts, Phys. Rev. C **85**, 025205 (2012) arXiv:1112.2212 [nucl-th].
12. C. Chen, L. Chang, C.D. Roberts, S. Wan, D.J. Wilson, Few-Body Syst. **53**, 293 (2012) arXiv:1204.2553 [nucl-th].

13. R.G. Edwards, N. Mathur, D.G. Richards, S.J. Wallace, Phys. Rev. D **87**, 054506 (2013) arXiv:1212.5236 [hep-ph].
14. I.S. Barker, A. Donnachie, J.K. Storrow, Nucl. Phys. B **95**, 347 (1975).
15. A.M. Sandorfi, S. Hoblit, H. Kamano, T.-S.H. Lee, J. Phys. G **38**, 053001 (2011) arXiv:1010.4555 [nucl-th].
16. R.L. Workman, M.W. Paris, W.J. Briscoe, L. Tiator, S. Schumann, M. Ostrick, S.S. Kamalov, Eur. Phys. J. A **47**, 143 (2011) arXiv:1102.4897 [nucl-th].
17. T. Vrancx, J. Ryckebusch, T. Van Cuyck, P. Vancraeyveld, Phys. Rev. C **87**, 055205 (2013) arXiv:1303.2936 [nucl-th].
18. W.-T. Chiang, F. Tabakin, Phys. Rev. C **55**, 2054 (1996).
19. A.S. Omelaenko, Sov. J. Nucl. Phys. **34**, 406 (1981).
20. Y. Wunderlich, R. Beck, L. Tiator, arXiv:1312.0245 [nucl-th].
21. V. Bernard, N. Kaiser, J. Gasser, U.-G. Meißner, Phys. Lett. B **268**, 291 (1991).
22. V. Bernard, N. Kaiser, U.-G. Meißner, Nucl. Phys. B **383**, 442 (1992).
23. V. Bernard, N. Kaiser, T.-S.H. Lee, U.-G. Meißner, Phys. Rep. **246**, 315 (1994) hep-ph/9310329.
24. V. Bernard, N. Kaiser, U.-G. Meißner, A. Schmidt, Nucl. Phys. A **580**, 475 (1994) nucl-th/9403013.
25. V. Bernard, N. Kaiser, U.-G. Meißner, Z. Phys. C **70**, 483 (1996) hep-ph/9411287.
26. V. Bernard, N. Kaiser, U.-G. Meißner, Phys. Lett. B **382**, 19 (1996) nucl-th/9604010.
27. V. Bernard, B. Kubis, U.-G. Meißner, Eur. Phys. J. A **25**, 419 (2005) nucl-th/0506023.
28. M. Hoferichter, B. Kubis, U.-G. Meißner, Phys. Lett. B **678**, 65 (2009) arXiv:0903.3890 [hep-ph].
29. V. Baru, C. Hanhart, M. Hoferichter, B. Kubis, A. Nogga, D.R. Phillips, Phys. Lett. B **694**, 473 (2011) arXiv:1003.4444 [nucl-th].
30. V. Baru, C. Hanhart, M. Hoferichter, B. Kubis, A. Nogga, D.R. Phillips, Nucl. Phys. A **872**, 69 (2011) arXiv:1107.5509 [nucl-th].
31. C. Ditsche, M. Hoferichter, B. Kubis, U.-G. Meißner, JHEP **06**, 043 (2012) arXiv:1203.4758 [hep-ph].
32. M. Hilt, S. Scherer, L. Tiator, Phys. Rev. C **87**, 045204 (2013) arXiv:1301.5576 [nucl-th].
33. M. Hilt, B.C. Lehnhart, S. Scherer, L. Tiator, Phys. Rev. C **88**, 055207 (2013) arXiv:1309.3385 [nucl-th].
34. C. Fernández Ramírez, A.M. Bernstein, Phys. Lett. B **724**, 253 (2013) arXiv:1212.3237 [nucl-th].
35. C. Fernández Ramírez, A.M. Bernstein, T.W. Donnelly, Phys. Rev. C **80**, 065201 (2009) arXiv:0907.3463 [nucl-th].
36. U.-G. Meißner, J.A. Oller, Nucl. Phys. A **673**, 311 (2000) arXiv:nucl-th/9912026.
37. M. Mai, P.C. Bruns, U.-G. Meißner, Phys. Rev. D **86**, 094033 (2012) arXiv:1207.4923 [nucl-th].
38. D. Ruic, M. Mai, U.-G. Meißner, Phys. Lett. B **704**, 659 (2011) arXiv:1108.4825 [nucl-th].
39. P.C. Bruns, M. Mai, U.-G. Meißner, Phys. Lett. B **697**, 254 (2011) arXiv:1012.2233 [nucl-th].
40. A. Gasparyan, M.F.M. Lutz, Nucl. Phys. A **848**, 126 (2010) arXiv:1003.3426 [hep-ph].
41. M. Döring, E. Oset, U.-G. Meißner, Eur. Phys. J. A **46**, 315 (2010) arXiv:1003.0097 [nucl-th].
42. M. Döring, K. Nakayama, Phys. Lett. B **683**, 145 (2010) arXiv:0909.3538 [nucl-th].
43. M. Döring, Nucl. Phys. A **786**, 164 (2007) nucl-th/0701070.
44. B. Borasoy, P.C. Bruns, U.-G. Meißner, R. Nißler, Eur. Phys. J. A **34**, 161 (2007) arXiv:0709.3181 [nucl-th].
45. B. Borasoy, U.-G. Meißner, R. Nißler, Phys. Rev. C **74**, 055201 (2006) hep-ph/0606108.
46. M. Döring, E. Oset, D. Strottman, Phys. Lett. B **639**, 59 (2006) nucl-th/0602055.
47. M. Döring, E. Oset, D. Strottman, Phys. Rev. C **73**, 045209 (2006) nucl-th/0510015.
48. K.P. Khemchandani, A. Martinez Torres, H. Nagahiro, A. Hosaka, Phys. Rev. D **88**, 114016 (2013) arXiv:1307.8420 [nucl-th].
49. K.P. Khemchandani, A. Martinez Torres, H. Nagahiro, A. Hosaka, Int. J. Mod. Phys. Conf. Ser. **26**, 1460060 (2014) arXiv:1310.0067 [nucl-th].
50. E.J. Garzón, E. Oset, Eur. Phys. J. A **48**, 5 (2012) arXiv:1201.3756 [hep-ph].
51. J.-J. Wu, R. Molina, E. Oset, B.S. Zou, Phys. Rev. C **84**, 015202 (2011) arXiv:1011.2399 [nucl-th].
52. E.E. Kolomeitsev, M.F.M. Lutz, Phys. Lett. B **585**, 243 (2004) nucl-th/0305101.
53. C. García Recio, M.F.M. Lutz, J. Nieves, Phys. Lett. B **582**, 49 (2004) nucl-th/0305100.
54. A.V. Anisovich, R. Beck, E. Klempt, V.A. Nikonov, A.V. Sarantsev, U. Thoma, Eur. Phys. J. A **48**, 88 (2012) arXiv:1205.2255 [nucl-th].
55. A.V. Anisovich, R. Beck, E. Klempt, V.A. Nikonov, A.V. Sarantsev, U. Thoma, Eur. Phys. J. A **48**, 15 (2012) arXiv:1112.4937 [hep-ph].
56. A.V. Anisovich, R. Beck, E. Klempt, V.A. Nikonov, A.V. Sarantsev, U. Thoma, Y. Wunderlich, Eur. Phys. J. A **49**, 121 (2013) arXiv:1306.5126 [hep-ph].
57. X. Cao, V. Shklyar, H. Lenske, Phys. Rev. C **88**, 055204 (2013) arXiv:1303.2604 [nucl-th].
58. V. Shklyar, H. Lenske, U. Mosel, Phys. Rev. C **87**, 015201 (2013) arXiv:1206.5414 [nucl-th].
59. M. Shrestha, D.M. Manley, Phys. Rev. C **86**, 055203 (2012) arXiv:1208.2710 [hep-ph].
60. M. Shrestha, D.M.M. Manley, Phys. Rev. C **86**, 045204 (2012) arXiv:1205.5294 [hep-ph].
61. M. Batinic, S. Ceci, A. Švarc, B. Zauner, Phys. Rev. C **82**, 038203 (2010).
62. S. Ceci, A. Švarc, B. Zauner, Phys. Rev. Lett. **97**, 062002 (2006) hep-ph/0603144.
63. P.F.A. Goudsmit, H.J. Leisi, E. Matsinos, B.L. Birbrair, A.B. Gridnev, Nucl. Phys. A **575**, 673 (1994).
64. A.B. Gridnev, N.G. Kozlenko, Eur. Phys. J. A **4**, 187 (1999).
65. A.B. Gridnev, I. Horn, W.J. Briscoe, I.I. Strakovsky, Phys. At. Nucl. **69**, 1542 (2006) hep-ph/0408192.
66. D. Drechsel, S.S. Kamalov, L. Tiator, Eur. Phys. J. A **34**, 69 (2007) arXiv:0710.0306 [nucl-th].
67. L. Tiator, D. Drechsel, S.S. Kamalov, M. Vanderhaeghen, Eur. Phys. J. ST **198**, 141 (2011) arXiv:1109.6745 [nucl-th].
68. H. Kamano, S.X. Nakamura, T.-S.H. Lee, T. Sato, Phys. Rev. C **88**, 035209 (2013) arXiv:1305.4351 [nucl-th].
69. N. Suzuki, T. Sato, T.-S.H. Lee, Phys. Rev. C **82**, 045206 (2010) arXiv:1006.2196 [nucl-th].

70. M.W. Paris, Phys. Rev. C **79**, 025208 (2009) arXiv:0802.3383 [nucl-th].
71. B. Juliá Díaz, T.-S.H. Lee, A. Matsuyama, T. Sato, L.C. Smith, Phys. Rev. C **77**, 045205 (2008) arXiv:0712.2283 [nucl-th].
72. B. Juliá Díaz, T.-S.H. Lee, A. Matsuyama, T. Sato, Phys. Rev. C **76**, 065201 (2007) arXiv:0704.1615 [nucl-th].
73. A. Matsuyama, T. Sato, T.-S.H. Lee, Phys. Rep. **439**, 193 (2007) arXiv:nucl-th/0608051.
74. L. Tiator, S.S. Kamalov, S. Ceci, G.Y. Chen, D. Drechsel, A. Svarc, S.N. Yang, Phys. Rev. C **82**, 055203 (2010) arXiv:1007.2126 [nucl-th].
75. G.Y. Chen, S.S. Kamalov, S.N. Yang, D. Drechsel, L. Tiator, Phys. Rev. C **76**, 035206 (2007) arXiv:nucl-th/0703096.
76. C. Fernández-Ramírez, E. Moya de Guerra, J.M. Udías, Ann. Phys. **321**, 1408 (2006) nucl-th/0509020.
77. V. Pascalutsa, J.A. Tjon, Phys. Rev. C **70**, 035209 (2004) nucl-th/0407068.
78. M.G. Fuda, H. Alharbi, Phys. Rev. C **68**, 064002 (2003).
79. D. Rönchen, M. Döring, F. Huang, H. Haberzettl, J. Haidenbauer, C. Hanhart, S. Krewald, U.-G. Meißner, K. Nakayama, Eur. Phys. J. A **49**, 44 (2013) arXiv:1211.6998 [nucl-th].
80. Figures representing the full solution of this study and tables of hadronic transitions among the channels  $\pi N$ ,  $\eta N$ ,  $K\Lambda$ , and  $K\Sigma$  can be downloaded at <http://collaborations.fz-juelich.de/ikp/meson-baryon/main>.
81. M. Döring, C. Hanhart, F. Huang, S. Krewald, U.-G. Meißner, D. Rönchen, Nucl. Phys. A **851**, 58 (2011) arXiv:1009.3781 [nucl-th].
82. M. Döring, C. Hanhart, F. Huang, S. Krewald, U.-G. Meißner, Phys. Lett. B **681**, 26 (2009) arXiv:0903.1781 [nucl-th].
83. M. Döring, C. Hanhart, F. Huang, S. Krewald, U.-G. Meißner, Nucl. Phys. A **829**, 170 (2009) arXiv:0903.4337 [nucl-th].
84. A.M. Gasparyan, J. Haidenbauer, C. Hanhart, J. Speth, Phys. Rev. C **68**, 045207 (2003) arXiv:nucl-th/0307072.
85. O. Krehl, C. Hanhart, S. Krewald, J. Speth, Phys. Rev. C **62**, 025207 (2000) arXiv:nucl-th/9911080.
86. S. Ceci, M. Döring, C. Hanhart, S. Krewald, U.-G. Meißner, A. Švarc, Phys. Rev. C **84**, 015205 (2011) arXiv:1104.3490 [nucl-th].
87. A.V. Anisovich, E. Klempt, V.A. Nikonov, A.V. Sarantsev, U. Thoma, Eur. Phys. J. A **49**, 158 (2013) arXiv:1310.3610 [nucl-ex].
88. M. Döring, J. Haidenbauer, U.-G. Meißner, A. Rusetsky, Eur. Phys. J. A **47**, 163 (2011) arXiv:1108.0676 [hep-lat].
89. C.B. Lang, V. Verduci, Phys. Rev. D **87**, no. 5, 054502 (2013) arXiv:1212.5055.
90. G.P. Engel, C.B. Lang, D. Mohler, A. Schäfer, Phys. Rev. D **87**, 074504 (2013) arXiv:1301.4318 [hep-lat].
91. C. Alexandrou, J.W. Negele, M. Petschlies, A. Strelchenko, A. Tsapalis, Phys. Rev. D **88**, 031501 (2013) arXiv:1305.6081 [hep-lat].
92. M. Lage, U.-G. Meißner, A. Rusetsky, Phys. Lett. B **681**, 439 (2009) arXiv:0905.0069 [hep-lat].
93. M. Döring, U.-G. Meißner, E. Oset, A. Rusetsky, Eur. Phys. J. A **48**, 114 (2012) arXiv:1205.4838 [hep-lat].
94. M. Döring, U.-G. Meißner, JHEP **01**, 009 (2012) arXiv:1111.0616 [hep-lat].
95. M. Döring, U.-G. Meißner, E. Oset, A. Rusetsky, Eur. Phys. J. A **47**, 139 (2011) arXiv:1107.3988 [hep-lat].
96. M. Döring, M. Mai, U.-G. Meißner, Phys. Lett. B **722**, 185 (2013) arXiv:1302.4065 [hep-lat].
97. F. Huang, M. Döring, H. Haberzettl, J. Haidenbauer, C. Hanhart, S. Krewald, U.-G. Meißner, K. Nakayama, Phys. Rev. C **85**, 054003 (2012) arXiv:1110.3833 [nucl-th].
98. H. Haberzettl, F. Huang, K. Nakayama, Phys. Rev. C **83**, 065502 (2011) arXiv:1103.2065 [nucl-th].
99. H. Haberzettl, K. Nakayama, S. Krewald, Phys. Rev. C **74**, 045202 (2006) nucl-th/0605059.
100. H. Haberzettl, Phys. Rev. C **56**, 2041 (1997) nucl-th/9704057.
101. W. Chen, H. Gao, W.J. Briscoe, D. Dutta, A.E. Kudryavtsev, M. Mirazita, M.W. Paris, P. Rossi *et al.*, Phys. Rev. C **86**, 015206 (2012) arXiv:1203.4412 [hep-ph].
102. R.L. Workman, Phys. Rev. C **83**, 035201 (2011) arXiv:1007.3041 [nucl-th].
103. M.W. Paris, R.L. Workman, Phys. Rev. C **82**, 035202 (2010) arXiv:1004.0455 [nucl-th].
104. R.A. Arndt, W.J. Briscoe, I.I. Strakovsky, R.L. Workman, Phys. Rev. C **66**, 055213 (2002) nucl-th/0205067.
105. M. Döring, K. Nakayama, Eur. Phys. J. A **43**, 83 (2010) arXiv:0906.2949 [nucl-th].
106. C. Hanhart, Phys. Lett. B **715**, 170 (2012) arXiv:1203.6839 [hep-ph].
107. D. Morgan, M.R. Pennington, Z. Phys. C **37**, 431 (1988) **39**, 590(E) (1988).
108. W. Chen, T. Mibe, D. Dutta, H. Gao, J.M. Laget, M. Mirazita, P. Rossi, S. Stepanyan *et al.*, Phys. Rev. Lett. **103**, 012301 (2009) arXiv:0903.1260 [nucl-ex].
109. Graal Collaboration (G. Mandaglio *et al.*), Phys. Rev. C **82**, 045209 (2010) arXiv:1010.1715 [nucl-ex].
110. W.J. Briscoe, A.E. Kudryavtsev, P. Pedroni, I.I. Strakovsky, V.E. Tarasov, R.L. Workman, Phys. Rev. C **86**, 065207 (2012) arXiv:1209.0024 [nucl-th].
111. V.E. Tarasov, W.J. Briscoe, H. Gao, A.E. Kudryavtsev, I.I. Strakovsky, Phys. Rev. C **84**, 035203 (2011) arXiv:1105.0225 [hep-ph].
112. S. Weinberg, Phys. Rev. Lett. **17**, 616 (1966).
113. V. Bernard, N. Kaiser, U.-G. Meißner, Phys. Lett. B **309**, 421 (1993) hep-ph/9304275.
114. U.-G. Meißner, S. Steininger, Phys. Lett. B **419**, 403 (1998) hep-ph/9709453.
115. A.M. Bernstein, Phys. Lett. B **442**, 20 (1998) hep-ph/9810376.
116. F. Huang, H. Haberzettl, K. Nakayama, Phys. Rev. C **87**, 054004 (2013) arXiv:1208.2279 [nucl-th].
117. K. Nakayama, Y. Oh, H. Haberzettl, J. Korean Phys. Soc. **59**, 224 (2011) arXiv:0803.3169 [hep-ph].
118. M. Dugger, B.G. Ritchie, P. Collins, E. Pasyuk, W.J. Briscoe, I.I. Strakovsky, R.L. Workman, Y. Azimov *et al.*, Phys. Rev. C **88**, 065203 (2013) arXiv:1308.4028 [nucl-ex].
119. A.V. Anisovich, E. Klempt, V.A. Nikonov, A.V. Sarantsev, U. Thoma, Eur. Phys. J. A **47**, 153 (2011) arXiv:1109.0970 [hep-ph].
120. CBELSA/TAPS Collaboration (V. Crede *et al.*), Phys. Rev. C **84**, 055203 (2011) arXiv:1107.2151 [nucl-ex].
121. J.P. Ader, M. Capdeville, Ph. Salin, Nucl. Phys. B **3**, 407 (1967).

122. J.P. Ader, M. Capdeville, P. Salin, Nucl. Phys. B **17**, 221 (1970).
123. M. Guidal, J.M. Laget, M. Vanderhaeghen, Nucl. Phys. A **627**, 645 (1997).
124. A. Sibirtsev, J. Haidenbauer, F. Huang, S. Krewald, U.-G. Meißner, Eur. Phys. J. A **40**, 65 (2009) arXiv:0903.0535 [hep-ph].
125. A. Sibirtsev, J. Haidenbauer, S. Krewald, U.-G. Meißner, A.W. Thomas, Eur. Phys. J. A **41**, 71 (2009) arXiv:0902.1819 [hep-ph].
126. CB-ELSA Collaboration (O. Bartholomy *et al.*), Phys. Rev. Lett. **94**, 012003 (2005) hep-ex/0407022.
127. M. Dugger, B.G. Ritchie, J.P. Ball, P. Collins, E. Pasyuk, R.A. Arndt, W.J. Briscoe, I.I. Strakovsky *et al.*, Phys. Rev. C **76**, 025211 (2007) arXiv:0705.0816 [hep-ex].
128. G. Buschhorn, P. Heide, U. Kotz, R.A. Lewis, P. Schmuser, H.J. Skronn, Phys. Rev. Lett. **20**, 230 (1968).
129. B. Bouquet, B. D'Almagne, P.T. Eschstruth, M. Croissiaux, E.F. Erickson, R. Morand, J.P. Pahin, P. Kitching *et al.*, Phys. Rev. Lett. **27**, 1244 (1971).
130. K. Ekstrand, A. Browman, L. Hand, M.E. Nordberg, Phys. Rev. D **6**, 1 (1972).
131. R.A. Alvarez, G. Cooperstein, K. Kalata, R.C. Lanza, D. Luckey, Phys. Rev. D **1**, 1946 (1970).
132. G. Buschhorn, J. Carroll, R.D. Eandi, P. Heide, R. Hubner, W. Kern, U. Kotz, P. Schmuser *et al.*, Phys. Rev. Lett. **17**, 1027 (1966).
133. G. Buschhorn, J. Carroll, R.D. Eandi, P. Heide, R. Hubner, W. Kern, U. Kotz, P. Schmuser *et al.*, Phys. Rev. Lett. **18**, 571 (1967).
134. CLAS Collaboration (M. Dugger *et al.*), Phys. Rev. C **79**, 065206 (2009) arXiv:0903.1110 [hep-ex].
135. A. Schmidt, P. Achenbach, J. Ahrens, H.J. Arends, R. Beck, A.M. Bernstein, V. Hejny, M. Kotulla *et al.*, Phys. Rev. Lett. **87**, 232501 (2001) **110**, 039903(E) (2013) nucl-ex/0105010.
136. M. Fuchs, J. Ahrens, G. Anton, R. Auerbeck, R. Beck, A.M. Bernstein, A.R. Gabler, F. Härter *et al.*, Phys. Lett. B **368**, 20 (1996).
137. R. Beck, F. Kalleicher, B. Schoch, J. Vogt, G. Koch, H. Ströher, V. Metag, J.C. McGeorge *et al.*, Phys. Rev. Lett. **65**, 1841 (1990).
138. A2 and CB-TAPS Collaboration (D. Hornidge *et al.*), Phys. Rev. Lett. **111**, 062004 (2013) arXiv:1211.5495 [nucl-ex].
139. J.C. Bergstrom, R. Igarashi, J.M. Vogt, Phys. Rev. C **55**, 2016 (1997).
140. W. Hitzeroth, Nuovo Cimento A **60**, 467 (1969).
141. R. Beck, Eur. Phys. J. A **28S1**, 173 (2006).
142. GDH and A2 Collaboration (J. Ahrens *et al.*), Eur. Phys. J. A **21**, 323 (2004).
143. GRAAL Collaboration (O. Bartalini *et al.*), Eur. Phys. J. A **26**, 399 (2005).
144. GDH and A2 Collaborations (J. Ahrens *et al.*), Phys. Rev. Lett. **88**, 232002 (2002) hep-ex/0203006.
145. M. Sumihama, J.K. Ahn, H. Akimune, Y. Asano, W.C. Chang, S. Date, H. Ejiri, H. Fujimura *et al.*, Phys. Lett. B **657**, 32 (2007) arXiv:0708.1600 [nucl-ex].
146. E. Korkmaz, N.R. Kolb, D.A. Hutcheon, G.V. O'Rielly, J.C. Bergstrom, G. Feldman, D. Jordan, A.K. Opper *et al.*, Phys. Rev. Lett. **83**, 3609 (1999).
147. K.G. Fissum, H.S. Caplan, E.L. Hallin, D.M. Skopik, J.M. Vogt, M. Frodyma, D.P. Rosenzweig, D.W. Storm *et al.*, Phys. Rev. C **53**, 1278 (1996).
148. J.K. Walker, J.P. Burq, Phys. Rev. Lett. **8**, 37 (1962).
149. D.W.G.S. Leith, R. Little, E.M. Lawson, Phys. Lett. **8**, 355 (1964).
150. H.B. van den Brink, H.P. Blok, H.T. Chung, H. Choi, T. Gresko, E.L. Hallin, W.H.A. Hesselink, T. Kobayashi *et al.*, Nucl. Phys. A **587**, 657 (1995).
151. K. Büchler, K.H. Althoff, G. Anton, J. Arends, W. Beulertz, M. Breuer, P. Detemple, H. Dutz *et al.*, Nucl. Phys. A **570**, 580 (1994).
152. G. Fischer, H. Fischer, M. Heuel, G. Von Holtey, G. Knop, J. Stumpfig, Nucl. Phys. B **16**, 119 (1970).
153. G. Fischer, G. Von Holtey, G. Knop, J. Stumpfig, Z. Phys. **253**, 38 (1972).
154. D. Branford, J.A. MacKenzie, F.X. Lee, J. Ahrens, J.R.M. Annand, R. Beck, G.E. Cross, T. Davinson *et al.*, Phys. Rev. C **61**, 014603 (2000).
155. T. Fujii, T. Kondo, F. Takasaki, S. Yamada, S. Homma, K. Huke, S. Kato, H. Okuno *et al.*, Nucl. Phys. B **120**, 395 (1977).
156. E.A. Knapp, R.W. Kenney, V. Perez-Mendez, Phys. Rev. **114**, 605 (1959).
157. R. Beck, H.P. Krahn, J. Ahrens, J.R.M. Annand, H.J. Arends, G. Audit, A. Braghieri, N. d'Hose *et al.*, Phys. Rev. C **61**, 035204 (2000) nucl-ex/9908017.
158. T. Fujii, H. Okuno, S. Orito, H. Sasaki, T. Nozaki, F. Takasaki, Takikawa, K. Amako *et al.*, Phys. Rev. Lett. **26**, 1672 (1971).
159. H.W. Dannhausen, E.J. Durwen, H.M. Fischer, M. Leneke, W. Niehaus, F. Takasaki, Eur. Phys. J. A **11**, 441 (2001).
160. J. Ahrens, S. Altieri, J.R.M. Annand, H.-J. Arends, R. Beck, C. Bradtke, A. Braghieri, N. d'Hose *et al.*, Phys. Rev. C **74**, 045204 (2006).
161. S.D. Ecklund, R.L. Walker, Phys. Rev. **159**, 1195 (1967).
162. J.R. Kilner, PhD thesis (1962).
163. R.A. Alvarez, G. Cooperstein, K. Kalata, R.C. Lanza, D. Luckey, Phys. Rev. D **1**, 1946 (1970).
164. Jefferson Lab Hall A and Jefferson Lab E94-104 Collaborations (L.Y. Zhu *et al.*), Phys. Rev. C **71**, 044603 (2005) nucl-ex/0409018.
165. G. Blanpied, M. Blecher, A. Caracappa, R. Deininger, C. Djalali, G. Giordano, K. Hicks, S. Hoblit *et al.*, Phys. Rev. C **64**, 025203 (2001).
166. F.V. Adamian, A.Y. Bunyatyan, G.S. Frangulian, P.I. Galumian, V.H. Grabsky, A.V. Airapetian, H.H. Hakopian, V.K. Hokinian *et al.*, Phys. Rev. C **63**, 054606 (2001) nucl-ex/0011006.
167. CBELSA and TAPS Collaborations (D. Elsner *et al.*), Eur. Phys. J. A **39**, 373 (2009) arXiv:0810.1849 [nucl-ex].
168. CBELSA/TAPS Collaboration (N. Sparks *et al.*), Phys. Rev. C **81**, 065210 (2010) arXiv:1003.1346 [nucl-ex].
169. GRAAL Collaboration (J. Ajaka *et al.*), Phys. Lett. B **475**, 372 (2000).
170. GRAAL and GW-SAID Group Collaborations (O. Bartalini *et al.*), Phys. Lett. B **544**, 113 (2002) nucl-ex/0207010.
171. A. Bock, G. Anton, W. Beulertz, C. Bradtke, H. Dutz, R. Gehring, S. Goertz, K. Helbing *et al.*, Phys. Rev. Lett. **81**, 534 (1998).
172. A.A. Belyaev, V.A. Get'man, V.G. Gorbenko, V.A. Gushchin, A.Ya. Derkach, Y.V. Zhebrovsky, I.M. Karnaukhov, L.Ya. Kolesnikov *et al.*, Nucl. Phys. B **213**, 201 (1983).

173. M. Fukushima, N. Horikawa, R. Kajikawa, H. Kobayakawa, K. Mori, T. Nakanishi, C.O. Pak, S. Suzuki *et al.*, Nucl. Phys. B **136**, 189 (1978).
174. P.S.L. Booth, L.J. Carroll, G.R. Court, P.R. Daniel, R. Gamet, C.J. Hardwick, P.J. Hayman, J.R. Holt *et al.*, Nucl. Phys. B **121**, 45 (1977).
175. H. Herr, D. Husmann, W. Jansen, V. Kadansky, B. Lohr, W. Meyer, H. Schilling, T. Yamaki, Nucl. Phys. B **125**, 157 (1977).
176. P.J. Bussey, C. Raine, J.G. Rutherglen, P.S.L. Booth, L.J. Carroll, G.R. Court, P.R. Daniel, A.W. Edwards *et al.*, Nucl. Phys. B **154**, 492 (1979).
177. H. Dutz, D. Krämer, B. Zucht, K.H. Althoff, G. Anton, J. Arends, W. Beulertz, A. Bock *et al.*, Nucl. Phys. A **601**, 319 (1996).
178. V.A. Getman, V.G. Gorbenko, A.Y. Derkach, Y.V. Zhebrovsky, I.M. Karnaukhov, L.Y. Kolesnikov, A.A. Lukhanin, A.L. Rubashkin *et al.*, Nucl. Phys. B **188**, 397 (1981).
179. M. Fukushima, N. Horikawa, R. Kajikawa, H. Kobayakawa, K. Mori, T. Nakanishi, C.O. Pak, S. Suzuki *et al.*, Nucl. Phys. B **130**, 486 (1977).
180. P.J. Bussey, C. Raine, J.G. Rutherglen, P.S.L. Booth, L.J. Carroll, G.R. Court, P.R. Daniel, A.W. Edwards *et al.*, Nucl. Phys. B **154**, 205 (1979).
181. K.H. Althoff, R. Conrad, M. Gies, H. Herr, V. Kadansky, O. Kaul, K. Königsmann, G. Lenzen *et al.*, Phys. Lett. B **63**, 107 (1976).
182. K.H. Althoff, M. Gies, H. Herr, V. Kadansky, O. Kaul, K. Königsmann, D. Menze, W. Meyer *et al.*, Nucl. Phys. B **131**, 1 (1977).
183. K. Fujii, H. Hayashii, S. Iwata, R. Kajikawa, A. Miyamoto, T. Nakanishi, Y. Ohashi, S. Okumi *et al.*, Nucl. Phys. B **197**, 365 (1982).
184. K.H. Althoff, D. Finken, N. Minatti, H. Piel, D. Trines, M. Unger, Phys. Lett. B **26**, 677 (1968).
185. K.H. Althoff, K. Kramp, H. Matthay, H. Piel, Z. Phys. **194**, 135 (1966).
186. K.H. Althoff, K. Kramp, H. Matthay, H. Piel, Z. Phys. **194**, 144 (1966).
187. P. Blum, P. Brinckmann, R. Brockmann, P. Lutter, W. Mohr, R. Sauerwein, Z. Phys. A **277**, 311 (1976).
188. P. Blum, R. Brockmann, W. Mohr, Z. Phys. A **278**, 275 (1976).
189. V.G. Gorbenko, A.I. Derebchinskii, Y.V. Zhebrovskii, A.A. Zybalov, O.G. Konovaloo, V.I. Nikiforov, A.L. Rubashkin, P.V. Sorokin, A.E. Tenishev, Sov. J. Nucl. Phys. **27**, 638 (1978).
190. A.S. Bratashevsky, V.G. Gorbenko, A.I. Derebchinsky, A.Y. Derkach, Y.V. Zhebrovsky, A.A. Zybalov, I.M. Karnaukhov, L.Y. Kolesnikov *et al.*, Nucl. Phys. B **166**, 525 (1980).
191. V.G. Gorbenko *et al.*, JETP Lett. **19**, 340 (1974).
192. V.G. Gorbenko *et al.*, JETP Lett. **22**, 186 (1975).
193. V.G. Gorbenko *et al.*, Sov. J. Nucl. Phys. **26**, 167 (1977).
194. A.I. Derebchinsky *et al.*, JETP **43**, 218 (1976).
195. A.S. Bratashevsky *et al.*, Sov. J. Nucl. Phys. **42**, 417 (1985).
196. A.S. Bratashevsky *et al.*, Sov. J. Nucl. Phys. **35**, 33 (1982).
197. A.A. Zybalov *et al.*, Sov. J. Nucl. Phys. **28**, 52 (1978).
198. N.V. Goncharov *et al.*, JETP **37**, 205 (1973).
199. A.S. Bratashevsky *et al.*, Sov. J. Nucl. Phys. **38**, 233 (1983).
200. A.S. Bratashevsky *et al.*, Sov. J. Nucl. Phys. **46**, 635 (1987).
201. A.S. Bratashevsky *et al.*, Sov. J. Nucl. Phys. **33**, 538 (1981).
202. A.S. Bratashevsky *et al.*, Sov. J. Nucl. Phys. **41**, 960 (1985).
203. A.I. Derebchinsky *et al.*, JETP **39**, 30 (1974).
204. S. Kato, T. Miyachi, K. Sugano, K. Toshioka, K. Ukai, M. Chiba, K. Egawa, T. Ishii *et al.*, Nucl. Phys. B **168**, 1 (1980).
205. S. Kayakawa *et al.*, J. Phys. Soc. Jap. **25**, 307 (1968).
206. S. Kabe, T. Fujii, T. Kamei, R. Yamada, T. Yamagata, S. Kato, I. Kita, T. Kiyoshima, Nucl. Phys. B **50**, 17 (1972).
207. J.O. Maloy, V.Z. Peterson, G.A. Salandin, F. Waldner, A. Manfredini, J.I. Friedman, H. Kendall, Phys. Rev. B **139**, 733 (1965).
208. E.D. Bloom, C.A. Heusch, C.Y. Prescott, L.S. Rochester, Phys. Rev. Lett. **19**, 671 (1967).
209. R. Querzoli, G. Salvini, A. Silverman, Nuovo Cimento **19**, 53 (1961).
210. L. Bertanza, I. Mannelli, S. Santucci, G.V. Silvestrini, V.Z. Peterson, Nuovo Cimento **24**, 734 (1962).
211. R.O. Avakyan *et al.*, Sov. J. Nucl. Phys. **37**, 199 (1983).
212. R.O. Avakyan *et al.*, Sov. J. Nucl. Phys. **46**, 853 (1987).
213. R.O. Avakyan *et al.*, Sov. J. Nucl. Phys. **48**, 1030 (1988).
214. N.M. Agababyan *et al.*, Sov. J. Nucl. Phys. **50**, 834 (1989).
215. M.M. Asaturyan *et al.*, JETP Lett. **44**, 341 (1986).
216. R.O. Avakyan *et al.*, Sov. J. Nucl. Phys. **53**, 448 (1991).
217. K. Wijesooriya, A. Afanasev, M. Amarian, K. Aniol, S. Becher, K. Benslama, L. Bimbot, P. Bosted *et al.*, Phys. Rev. C **66**, 034614 (2002).
218. GEP-III and GEP2 $\gamma$  Collaborations (W. Luo *et al.*), Phys. Rev. Lett. **108**, 222004 (2012) arXiv:1109.4650 [nucl-ex].
219. M.N. Prentice, R. Railton, J.G. Rutherglen, K.M. Smith, G.R. Brookes, P.J. Bussey, F.H. Combley, G.H. Eaton *et al.*, Nucl. Phys. B **41**, 353 (1972).
220. N. Tanaka, M.M. Castro, R.H. Milburn, W.B. Richards, J.P. Rutherford, B.F. Stearns, M. Deutsch, P.M. Patel *et al.*, Phys. Rev. D **8**, 1 (1973).
221. V.A. Getman *et al.*, Journal of Kharkov Physical Technical Institute, Vopr. At. Nauki Tekh **8**, 3 (1989).
222. A. Thiel, A.V. Anisovich, D. Bayadilov, B. Bantes, R. Beck, Y. Beloglazov, M. Bichow, S. Bose *et al.*, Phys. Rev. Lett. **109**, 102001 (2012) arXiv:1207.2686 [nucl-ex].
223. J. Ahrens, S. Altieri, J.R. Annand, H.J. Arends, R. Beck, A. Braghieri, N. d'Hose, H. Dutz *et al.*, Eur. Phys. J. A **26**, 135 (2005).
224. P.J. Bussey, J.G. Rutherglen, P.S.L. Booth, L.J. Carroll, G.R. Court, A.W. Edwards, R. Gamet, P.J. Hayman *et al.*, Nucl. Phys. B **159**, 383 (1979).
225. P.S.L. Booth, Bonn University Annual Report, 1977.
226. A.A. Belyaev *et al.*, Sov. J. Nucl. Phys. **40**, 83 (1984).
227. P.J. Bussey, J.G. Rutherglen, P.S.L. Booth, L.J. Carroll, G.R. Court, P.R. Daniel, A.W. Edwards, R. Gamet *et al.*, Nucl. Phys. B **169**, 403 (1980).
228. A.A. Belyaev *et al.*, Sov. J. Nucl. Phys. **43**, 947 (1983).
229. P.J. Bussey, *Physik Daten* (1977) unpublished.
230. CBELSA/TAPS Collaboration (M. Gottschall *et al.*), Phys. Rev. Lett. **112**, 012003 (2014) arXiv:1312.2187 [nucl-ex].

231. CB-ELSA Collaboration (H. van Pee *et al.*), Eur. Phys. J. A **31**, 61 (2007) arXiv:0704.1776 [nucl-ex].
232. M.H. Sikora, D.P. Watts, D.I. Glazier, P. Aguar-Bartolome, L.K. Akasoy, J.R.M. Annand, H.J. Arends, K. Bantawa *et al.*, Phys. Rev. Lett. **112**, 022501 (2014) arXiv:1309.7897 [nucl-ex].
233. A. Afanasev, C.E. Carlson, C. Wahlquist, Phys. Lett. B **398**, 393 (1997) hep-ph/9701215.
234. G.R. Farrar, K. Huleihel, H.-y. Zhang, Nucl. Phys. B **349**, 655 (1991).
235. L. Tiator, PWA7 workshop, 09/24/2013, Camogli, Italy.
236. V. Bernard, N. Kaiser, U.-G. Meißner, Phys. Lett. B **378**, 337 (1996) hep-ph/9512234.
237. M. Lenkewitz, E. Epelbaum, H.W. Hammer, U.-G. Meißner, Eur. Phys. J. A **49**, 20 (2013) arXiv:1209.2661 [nucl-th].
238. O. Hanstein, D. Drechsel, L. Tiator, Phys. Lett. B **399**, 13 (1997) nucl-th/9612057.
239. S.S. Kamalov, G.-Y. Chen, S.-N. Yang, D. Drechsel, L. Tiator, Phys. Lett. B **522**, 27 (2001) nucl-th/0107017.
240. V. Bernard, N. Kaiser, U.-G. Meißner, Eur. Phys. J. A **11**, 209 (2001) hep-ph/0102066.
241. M. Döring, D. Jido, E. Oset, Eur. Phys. J. A **45**, 319 (2010) arXiv:1002.3688 [nucl-th].
242. D. Jido, M. Döring, E. Oset, Phys. Rev. C **77**, 065207 (2008) arXiv:0712.0038 [nucl-th].
243. L.S. Geng, E. Oset, M. Döring, Eur. Phys. J. A **32**, 201 (2007) hep-ph/0702093.
244. M. Döring, E. Oset, S. Sarkar, Phys. Rev. C **74**, 065204 (2006) nucl-th/0601027.
245. Particle Data Group Collaboration (J. Beringer *et al.*), Phys. Rev. D **86**, 010001 (2012).
246. R.L. Workman, L. Tiator, A. Sarantsev, Phys. Rev. C **87**, 068201 (2013) arXiv:1304.4029 [nucl-th].
247. R.A. Arndt, R.L. Workman, Z. Li, L.D. Roper, Phys. Rev. C **42**, 1853 (1990).
248. R.A. Arndt, R.L. Workman, Z. Li, L.D. Roper, Phys. Rev. C **42**, 1864 (1990).
249. G.F. Chew, M.L. Goldberger, F.E. Low, Y. Nambu, Phys. Rev. **106**, 1345 (1957).
250. F.A. Berends, A. Donnachie, D.L. Weaver, Nucl. Phys. B **4**, 1 (1967).
251. K. Nakayama, W.G. Love, Phys. Rev. C **72**, 034603 (2005).
252. C.G. Fasano, F. Tabakin, B. Saghai, Phys. Rev. C **46**, 2430 (1992).
253. A.M. Sandorfi, B. Dey, A. Sarantsev, L. Tiator, R. Workman, AIP Conf. Proc. **1432**, 219 (2012) (see, arXiv:1108.5411v2 for a revised version).
254. L. Tiator, private communication.